

UFL/COEL-93/009

PIER SEDIMENT SCOUR TESTS FOR MERRILL-BARBER BRIDGE

FINAL REPORT

D. Max Sheppard

and

Maximo Ramos III

October 1993

FINAL REPORT
PIER SEDIMENT SCOUR TESTS FOR
MERRILL-BARBER BRIDGE

D. MAX SHEPPARD
AND
MAXIMO RAMOS III

OCTOBER 1993

1. Report No.		2. Government Accession No.		3. Recipient's Catalog No.	
4. Title and Subtitle Pier Sediment Scour Tests for Merrill-Barber Bridge				5. Report Date October 1993	
				6. Performing Organization Code	
				8. Performing Organization Report No. 49104511246	
7. Author(s) D. Max Sheppard, Maximo Ramos				10. Work Unit No. (TRAIS)	
9. Performing Organization Name and Address Coastal and Oceanographic Engineering Department University of Florida Gainesville, FL 32611-2083				11. Contract or Grant No.	
				13. Type of Report and Period Covered Final Report	
12. Sponsoring Agency Name and Address Florida Department of Transportation, District IV 780 SW 24th Street Ft. Lauderdale, Florida 33315-2696				14. Sponsoring Agency Code 88030-3514	
				15. Supplementary Notes	
16. Abstract <p>The objectives of this study were 1) to determine the maximum structure-induced local sediment scour depths for the proposed bridge piers for the Merrill Barber Bridge over Indian River on State Road 60 in Indian River County, Florida and 2) to determine the feasibility of predicting equilibrium local scour depths near complex multiple pile bridge piers from bottom shear stresses on the prescoured bed. A series of hydrodynamic tests were conducted in a laboratory flume (100 ft long x 8 ft wide x 2 ft deep) where flow velocities near model piers were measured with a two component constant temperature anemometer at a height of 3 mm above the bed. Bottom shear stresses were then estimated from the flow measurements. The piers (which are 1/15 scale models of proposed Merrill Barber Bridge piers) consisted of thirtysix square piles (3 columns of 12) and a pile cap that was positioned at different elevations above the bottom. Two different pile cap shapes were also considered. A simple relationship between the prescoured bottom shear stress and the equilibrium local scour depth was postulated.</p> <p>Sediment scour tests were then conducted in the same flume with the same models. The average duration of these tests was 28 hours. Scour depths were measured periodically throughout these tests using an acoustic transponder. The scour measurements were used 1) to establish the maximum scour depths for the Merrill Barber Bridge piers and 2) to calibrate and test the scour-shear stress relationship. Even though the range of conditions tested was somewhat limited, the approach appears promising and should be pursued further. A number of interesting findings were made regarding the rate at which scour occurs in these complex structures.</p>					
17. Key Words Bridge Pier Scour, Local Scour, Multiple Pile, Pile Caps, Footings			18. Distribution Statement No restrictions. This document is available to the public		
19. Security Classif. (of this report) Unclassified		20. Security Classif. (of this page) Unclassified		21. No. of Pages 134	22. Price

DISCLAIMER

“The opinions, findings and conclusions expressed in this publication are those of the authors and not necessarily those of the Florida Department of Transportation or the U.S. Department of Transportation. ”

“Prepared in cooperation with the State of Florida Department of Transportation and the U.S. Department of Transportation.”

TABLE OF CONTENTS

INTRODUCTION	1
BODY	1
PART A:	2
Hydrodynamic Study	2
Objectives of the Hydrodynamic Study	3
Experimental Plan and Procedures	3
Results of Hydrodynamic Experiments	4
PART B:	5
Scour Study	5
Objectives of the Scour Study	5
Experimental Plan and Procedures	5
Results of Scour Experiments	7
PART C:	7
Overall Results and Conclusions	7
Merrill-Barber Bridge Piers	7
Use of Prescoured Bottom Shear Stress to Estimate Local Scour	8
General Comments	8
REFERENCES	32
APPENDIX A	A34
HYDRODYNAMIC STUDY	A1
A.1 Background	A1
A.2 Experimental Procedures	A2
A.3 Data Acquisition	A4
A.3.1 X Sensor Probe	A4
A.3.2 Temperature Probe	A4
A.3.3 Temperature Correction	A5
A.3.4 Vortex Shedding from Probe Holder	A5
A.4 Flow Visualization Measurements	A6

APPENDIX B	B15
SCOUR STUDY	B1
B.1 Background	B1
B.2 Instrumentation and Calibration	B1
B.2.1 Depth Readings	B1
B.2.2 Position Readings	B2
B.3 Data Acquisition	B3
B.4 Data Reduction	B4
B.5 Test Procedures	B5
B.6 Time Rate of Scour	B5
APPENDIX C	C23
ANALYSIS OF HYDRODYNAMIC AND SCOUR RESULTS	C1
C.1 Mathematical Model	C1
APPENDIX D	D1
DATA	D1

LIST OF TABLES

Table 1.	Sequence of Hydrodynamic Tests	10
Table 2.	Sequence of Scour Tests	11
Table 3.	Calibration Tests	11
Table 4.	Maximum Scour Depths	12
Table A.1	Constant temperature anemometer technical data.	A7
Table A.2	X sensor probe technical data.	A8
Table A.3	Temperature probe technical data.	A8
Table A.4	Variation of mean velocity with time at the same location (x = -4.92 ft; y = 0.269 ft and z = 0.12 in).	A9
Table A.5	Variation of mean velocity across the tank in front of and away from the influence of the structure (x = -4.92 ft and z = 0.41 ft).	A9
Table A.6	X sensor probe cosine response - <u>probe vertical</u> (x = -4.92 ft; y = 1.46 ft and z = 0.12 in).	A10
Table A.7	X sensor probe cosine response - <u>probe horizontal</u> (x = -4.92 ft; y = 0.692 ft and z = 0.12 in).	A10
Table B.1	Echo sounder technical data.	B6
Table C.1	Some formulas for bed load and total load (Sleath, 1984).	C4
Table D.1	Values of x and y at grid points of hydrodynamic study.	D1
Table D.2	Results of hydrodynamic test H-1.	D3
Table D.3	Results of hydrodynamic test H-2.	D5
Table D.4	Results of hydrodynamic test H-3.	D7
Table D.5	Predicted and measured bottom elevations for scour test S-1 (no pile cap structure).	D9
Table D.6	Predicted and measured bottom elevations for scour test S-2 (70° pile cap structure - top position).	D15
Table D.7	Predicted and measured bottom elevations for scour test S-3 (70° pile cap structure - bottom position).	D21

LIST OF FIGURES

Figure 1	Definition sketch of pile cap.	13
Figure 2	Predicted bottom elevation (row 3, $x = 1.31$ ft) (see Figure A.3 for definition of axes).	14
Figure 3	Predicted bottom elevation (row 5, $x = 3.28$ ft) (see Figure A.3 for definition of axes).	15
Figure 4	Predicted bottom elevation (row 7, $x = 5.25$ ft) (see Figure A.3 for definition of axes).	16
Figure 5	Predicted bottom elevation (row 3, $x = 1.31$ ft) (see Figure A.3 for definition of axes).	17
Figure 6	Predicted bottom elevation (row 5, $x = 3.28$ ft) (see Figure A.3 for definition of axes).	18
Figure 7	Predicted bottom elevation (row 7, $x = 5.25$ ft) (see Figure A.3 for definition of axes).	19
Figure 8	Predicted bottom elevation (row 3, $x = 1.31$ ft) (see Figure A.3 for definition of axes).	20
Figure 9	Predicted bottom elevation (row 5, $x = 3.28$ ft) (see Figure A.3 for definition of axes).	21
Figure 10	Predicted bottom elevation (row 7, $x = 5.25$ ft) (see Figure A.3 for definition of axes).	22
Figure 11	Predicted bottom elevation (row 3, $x = 1.31$ ft) (see Figure A.3 for definition of axes).	23
Figure 12	Predicted bottom elevation (row 5, $x = 3.28$ ft) (see Figure A.3 for definition of axes).	24
Figure 13	Predicted bottom elevation (row 7, $x = 5.25$ ft) (see Figure A.3 for definition of axes).	25
Figure 14	Predicted bottom elevation (row 3, $x = 1.31$ ft) (see Figure A.3 for definition of axes).	26
Figure 15	Predicted bottom elevation (row 5, $x = 3.28$ ft) (see Figure A.3 for definition of axes).	27
Figure 16	Predicted bottom elevation (row 7, $x = 5.25$ ft) (see Figure A.3 for definition of axes).	28
Figure 17	Predicted bottom elevation (row 3, $x = 1.31$ ft) (see Figure A.3 for definition of axes).	29
Figure 18	Predicted bottom elevation (row 5, $x = 3.28$ ft) (see Figure A.3 for definition of axes).	30
Figure 19	Predicted bottom elevation (row 7, $x = 5.25$ ft) (see Figure A.3 for definition of axes).	31

Figure A.1	Shear stress profiles in front of and away from the influence of the structure at $x = -4.92$ ft and $y = 0.364$ ft.	A11
Figure A.2	Velocity profile corresponding to shear stress profiles in Figure A.1.	A11
Figure A.3	Grid points for hydrodynamic study (1:1 scale).	A12
Figure A.4	Grid points for hydrodynamic study (distorted 1:4.5 scale).	A12
Figure A.5	Overall set-up of experimental apparatus and instrumentation for hydrodynamic study.	A13
Figure A.6	Calibration curve for the temperature probe.	A14
Figure A.7	Calibration curve for the x sensor probe.	A14
Figure A.8	Mean velocity in front of structure vs. time at $x = -4.92$ ft and $z = 0.12$ in (test H-1).	A15
Figure A.9	Turbulent energy/unit mass in front of structure vs. time at $x = -4.92$ ft and $z = 0.12$ in (test H-1).	A15
Figure A.10	Unfiltered U and V velocity components for test H-1 at grid point B2.	A16
Figure A.11	Filtered U and V velocity components for test H-1 at grid point B2.	A17
Figure A.12	Power density spectra of U velocity components in Figures A.10 and A.11.	A18
Figure A.13	Power density spectra of V velocity components in Figures A.10 and A.11.	A19
Figure A.14	Mean velocity vs number of data points sampled ($x = 0.335$ ft; $y = 0.364$ ft and $z = 0.12$ in).	A20
Figure A.15	Variation of mean velocity parallel to the 70° pile cap (top position) structure at $y = 0.364$ ft and $z = 0.12$ in.	A20
Figure A.16	Variation of mean velocity normal to the 70° pile cap (top position) structure at $x = 0.335$ ft and $z = 0.12$ in.	A21
Figure B.1	Test area of flume showing no pile cap structure and central region near structure.	B7
Figure B.2	Sediment size distribution for Category 1 sand (away from structure).	B7
Figure B.3	Sediment size distribution for Category 2 sand (anchoring layer).	B8
Figure B.4	Sediment size distribution for Category 3 sand (around structure).	B8
Figure B.5	Overall set-up of experimental apparatus and instrumentation for scour study.	B9
Figure B.6	Experimental set-up for scour study.	B10
Figure B.7	Calibration curve for the echo sounder output signal.	B10
Figure B.8	Unfiltered output signals after completion of test S-1.	B11
Figure B.9	Filtered output signals after completion of test S-1.	B12

Figure B.10	Power density spectra of echo sounder output (Channel CH00) in Figures B.8 and B.9.	B13
Figure B.11	Modified calibration curve for echo sounder angle.	B14
Figure B.12	Power density spectra of y position potentiometer (Channel CH03) in Figures B.8 and B.9.	B15
Figure B.13	Definition sketch showing measurements needed for conversion of raw data to x-y coordinates.	B16
Figure B.14	Data points before start of scour test S-1 (No pile cap structure).	B17
Figure B.15	Data points after completion of scour test S-1 (No pile cap structure).	B17
Figure B.16	Time rate of scour of piles 1, 2 and 6 of no pile cap structure.	B18
Figure B.17	Time rate of scour of piles 1, 2 and 6 of 70 ⁰ pile cap (top position) structure.	B19
Figure B.18	Time rate of scour of pile 1.	B20
Figure B.19	Time rate of scour of pile 2.	B21
Figure B.20	Time rate of scour of pile 6.	B22
Figure C.1	Comparison of measured bottom elevation, predicted equilibrium bottom elevation and dimensionless shear stress for the no pile cap structure (row 2 : x = 0.33 ft).	C5
Figure C.2	Comparison of measured bottom elevation, predicted equilibrium bottom elevation and dimensionless shear stress for the no pile cap structure (row 3 : x = 1.31 ft).	C6
Figure C.3	Comparison of measured bottom elevation, predicted equilibrium bottom elevation and dimensionless shear stress for the no pile cap structure (row 4 : x = 2.30 ft).	C7
Figure C.4	Comparison of measured bottom elevation, predicted equilibrium bottom elevation and dimensionless shear stress for the no pile cap structure (row 5 : x = 3.28 ft).	C8
Figure C.5	Comparison of measured bottom elevation, predicted equilibrium bottom elevation and dimensionless shear stress for the no pile cap structure (row 6 : x = 4.27 ft).	C9
Figure C.6	Comparison of measured bottom elevation, predicted equilibrium bottom elevation and dimensionless shear stress for the no pile cap structure (row 7 : x = 5.25 ft).	C10
Figure C.7	Comparison of measured bottom elevation, predicted equilibrium bottom elevation and dimensionless shear stress for 70 ⁰ pile cap (top) structure (row 2 : x = 0.33 ft).	C11
Figure C.8	Comparison of measured bottom elevation, estimated and predicted equilibrium bottom elevations and dimensionless shear stress for the 70 ⁰ pile cap (top) structure (row 3 : x = 1.31 ft).	C12

Figure C.9	Comparison of measured bottom elevation, predicted equilibrium bottom elevation and dimensionless shear stress for the 70° pile cap (top) structure (row 4 : x = 2.30 ft).	C13
Figure C.10	Comparison of measured bottom elevation, predicted equilibrium bottom elevation and dimensionless shear stress for the 70° pile cap (top) structure (row 5 : x = 3.28 ft).	C14
Figure C.11	Comparison of measured bottom elevation, predicted equilibrium bottom elevation and dimensionless shear stress for the 70° pile cap (top) structure (row 6 : x = 4.27 ft).	C15
Figure C.12	Comparison of measured bottom elevation, predicted equilibrium bottom elevation and dimensionless shear stress for the 70° pile cap (top) structure (row 7 : x = 5.25 ft).	C16
Figure C.13	Contours of dimensionless shear stress, τ_d , around no pile cap structure.	C17
Figure C.14	Contours of dimensionless shear stress, τ_d , around 70° pile cap (top position) structure.	C17
Figure C.15	Contours of measured bottom elevation x 10 ² (ft) around no pile cap structure after completion of scour test.	C18
Figure C.16	Contours of predicted equilibrium bottom elevation x 10 ² (ft) around no pile cap structure.	C18
Figure C.17	Contours of measured bottom elevation x 10 ² (ft) around 70° pile cap (top position) structure after completion of scour test.	C19
Figure C.18	Contours of predicted equilibrium bottom elevation x 10 ² (ft) around 70° pile cap (top position) structure.	C19
Figure C.19	70° pile cap (top position) structure before the scour test.	C20
Figure C.20	70° pile cap (top position) structure after completion of the scour test.	C20
Figure C.21	Comparison of measured bottom elevation, predicted equilibrium bottom elevation and dimensionless shear stress for 70° pile cap (bottom) structure (row 3 : x = 1.31 ft).	C21
Figure C.22	70° pile cap (bottom position) structure before the scour test.	C22
Figure C.23	70° pile cap (bottom position) structure after completion of the scour test.	C22

PIER SEDIMENT SCOUR TESTS FOR MERRILL-BARBER BRIDGE

INTRODUCTION

Local sediment scour near complex, multiple pile structures is difficult to predict due to the complexity of the flow in the vicinity of these structures. At present one must rely on empirical equations based primarily on laboratory data for most structure-induced scour predictions. The number of studies and the quantity of data available for multiple pile structures is very limited. There were four objectives of the study reported on here. The primary objective was to obtain local pier scour data to aid in the establishment of design scour depths for Merrill-Barber Bridge piers. The second objective was to investigate the possibility of inferring local scour depths and volumes from near bottom flow measurements over the fixed, prescoured bed in the vicinity of the structure. A third objective was to determine if modifications to the pile cap design (side wall slope) would have an impact on the local scour depths. The fourth objective was to add to the database of scour data for multiple pile structures with pile caps.

The experimental portion of this study was divided into two major categories, namely that related to the "hydrodynamic tests" and that associated with the moveable bed or "scour tests". Even though the same physical models and flume were used in both series of tests, the objectives, procedures, instrumentation, etc. were different. Therefore, they will be discussed separately. The specific objectives of each category of tests are outlined followed by the overall philosophy and procedure used to achieve the results. This is followed by an analysis of data from both test series and conclusions on the subjects stated in the objectives. Throughout the report an attempt is made to present the main aspects of the analysis and results in the body and leave the details of the experimental procedure, instrumentation used, instrument calibration and the data for the Appendices.

BODY

The overall objectives of the research reported here were 1) to establish the maximum pier sediment scour depths and patterns for proposed Merrill-Barber Bridge pier designs, 2) to determine the effect of pile cap location and shape on the maximum pier sediment scour, 3) to examine the feasibility of predicting equilibrium sediment scour from estimates of prescoured bottom shear stress made from near bottom flow measurements over the area where scour is anticipated and 4) to obtain additional scour data for multiple pile structures.

All proposed pier designs for the Merrill-Barber Bridge consisted of three rows of twelve square piles (for a total of thirty-six piles per pier) with a centerline to diameter ratio, a/D , of three (see Figure 1). Also the overall dimensions of the pile caps tested were

constant for all tests. The quantities varied were, 1) the location of the caps relative to the bottom (and water surface), 2) the pier side wall slope and in the hydrodynamic tests 3) the pier orientation to the flow (i.e. the skew angle).

PART A: Hydrodynamic Study

Fixed bed models have been effectively used in the study and analysis of sediment transport for a number of years. The application has, for the most part however, been restricted to general sediment transport and not structure-induced scour. Local, structure-induced scour usually results in more significant changes in the bed over shorter distances than general scour, thus it was not clear at the start of this project if such an approach would work. It is not unreasonable, however, to assume that, unless the structure-flow changes drastically during the scour process, that the bottom will simply adjust (scour) until the bottom shear stress is reduced to that of the area away from the structure. Although more tests on different structures with different sediments and flow conditions are needed before definite conclusions can be reached the procedure seems to work for the range of conditions tested. A simple relationship between the near bottom flow parameters and the ultimate scour in the vicinity of the structure has been hypothesized.

Another application for this approach that appears promising is in the selection and placement of scour protection near complex pier structures. If scour protection in the form of riprap, mats, etc. are to be used near a bridge pier, a hydrodynamic study such as the one conducted here should be helpful in deciding the type and location of this protection.

Perhaps the best way to test the approach described above would be to directly measure the bottom shear stress in the vicinity of a structure (for a given set of flow conditions) and compare the results with those for a scour experiment for the structure subjected to the same environmental conditions. There are flush mounted probes on the market that measure bottom shear stress directly. These probes can be difficult to calibrate, however, and present installation problems for flumes with limited access to the bottom. Near bottom flow measurements (mean and fluctuating components of velocity) with a cross-wire constant temperature probe are perhaps easier to make and calibration is relatively straight forward if a variable speed instrument carriage is available. The drawback to this approach is, of course, that the stress measured in the flow has to be extrapolated to the bottom. For a variety of reasons (including insufficient time to construct and perfect a flush mounted shear stress probe calibration facility) the approach involving flow measurements just above the bottom was used in this study.

The configurations examined in the hydrodynamic tests are listed in Table 1.

Objectives of the Hydrodynamic Study

1. To obtain estimates of the bottom shear stress at points in the vicinity of the pier where scour is anticipated.
2. To obtain a relationship between the bottom shear stress and the local scour at that location.

Experimental Plan and Procedures

Two series of laboratory experiments were conducted on 1/15 scale models of proposed Merrill-Barber bridge piers. The first series were hydrodynamic tests and included four different vertical positions of the pile cap, two different pile cap designs (see Figure 1) and three different flow alignments. Near bottom flow measurements were made with a two-component constant temperature anemometer over a grid that covered a portion of the anticipated sediment scour area. The second series were sediment scour tests and included three different pile cap locations and two different pile cap designs. The scour experiments are described later in this report.

The flume in which these tests were conducted is 100 ft long x 8 ft wide x 2.5 ft deep and has a flat, zero sloped bottom. The bottom in the central part of the flume is recessed 1.08 ft over an area 8 ft wide and 20 ft long as shown in the photograph in Figure B.1. This recession was covered by five 4' x 8' steel plates for the hydrodynamic tests. A 100 hp pump recirculates the water and the depth and flow rate were controlled by a V-notch shaped weir at the entrance and a tail gate at the downstream end of the flume.

A comprehensive set of flow visualization tests were conducted first. These were used to obtain a qualitative understanding of the flow field in the vicinity of the structure and to determine the mean flow direction (and temporal variation in direction) at each grid point. A relatively large variation in flow direction with time $\pm 30^\circ$ was observed near the pier. This is due to alternate vortex shedding from the piles and pile cap. The variation in flow direction necessitated a rotation of the cross probe to a horizontal position from the normal vertical position. The consequences of this rotation with regard to shear stress measurement are discussed in detail in Appendix A. A grid was laid out along the side of the pier as shown in Figures A.3 and A.4. Near bottom flow measurements were made at each grid point with the probe directed in the mean flow direction. A small cutoff switch attached to the probe support insured that the center of the cross wire probe was located 0.12 in (3 mm) from the bottom at every grid point. The duration of each measurement was 2.7 minutes and was based on the largest period of variation of the flow. The flow field for the grided area was determined for each of the structure configurations given in Table 1.

Results of Hydrodynamic Experiments

The near bottom shear stress in a turbulent flow such as that considered here is composed of two components, i.e.

$$\tau = \tau_v + \tau_t \quad (1)$$

where

τ = total shear stress

$\tau_v = \mu \frac{\partial U}{\partial z} \equiv$ viscous component of shear stress

$\tau_t = a \rho (u'^2 + v'^2) \equiv$ turbulent component of shear stress

Note that the turbulent component of the bottom shear stress is expressed in terms of the horizontal components of the turbulent energy, where "a" is an experimentally determined constant. For a detailed discussion of the reasons and rationale for such a formulation see Appendix A. Estimated shear stress data for three of the structure configurations are given in Tables D.2 - D.4.

Most sediment transport theories assume that there is a relationship between the transport and the bottom shear stress (or the excess shear stress above that required to put the sediment in motion). As a first attempt to obtain a relationship between the prescoured bottom shear stress and the equilibrium scour depth the following simple relationship was used:

$$\begin{aligned} d_e &= f(\tau) \\ &= b \left(\frac{\tau - \tau_0}{\tau_0} \right)^c \\ &= b (\tau_d - 1)^c \end{aligned} \quad (2)$$

where

$d_e \equiv$ equilibrium scour depth

$b, c \equiv$ empirically determined coefficients

$\tau \equiv$ total prescoured bottom shear stress

$\tau_0 \equiv$ total shear stress away from structure

$\tau_d \equiv \frac{\tau}{\tau_0}$

The coefficients b and c were determined by using the shear stress measurements and equilibrium scour depths estimated from the measurements made at the end of the 28 hour tests. A least squares curve fit was used to determine coefficients. Scour depths versus time plots at various locations from the leading edge indicate that the scour depths for the first two rows of piles are near equilibrium. The maturity of the scour hole decreases significantly, however, with the distance from leading edge of the structure. That is, the scour hole at some distance from the upstream end of the pier cannot reach equilibrium until the sediment being scoured around the piles upstream from that position has subsided. Thus, the time required to reach an equilibrium scour depth will be shortest for the leading (upstream) edge of the pier and longest for the trailing (downstream) edge. For the conditions considered in this study (i.e. flow just below transition from clearwater to livebed conditions) the scour depth at the upstream end of the pier was estimated to be 90% of equilibrium after 28 hours of steady flow. Percentages of equilibrium for the remainder of the structure are difficult to estimate. The rate of scour plots shown in Figures B.16 - B.20 are very informative. Without this information it is difficult to judge the degree to which the scour hole has progressed. As the rate of scour decreases the scour hole may appear to have reached an equilibrium condition when in reality it is only a fraction of that value. More work on the rates at which local scour occurs is needed.

PART B: Scour Study

Scour experiments were also conducted as part of this study. Local scour experiments on model structures are an accepted method for estimating scour near prototype structures. Froude scaling laws have been used in the model specification and in estimating the prototype scour depths from the laboratory measurements.

Objectives of the Scour Study

1. To obtain sediment scour measurements for the pier configurations proposed for the Merrill-Barber Bridge.
2. To obtain local pier scour data that can be used to calibrate and test the scour prediction equation developed as part of the hydrodynamic study.

Experimental Plan and Procedures

As stated above the same flume and the same 1/15 scale physical models used for the hydrodynamic tests were used in the scour study. A sonar bottom scanning transponder was used to monitor the scour in the vicinity of the pier periodically over the duration of the 28 hour tests. At the end of each test, mechanical (point gage) measurements of the scour hole were made. Since the pump for the flume is not designed to transport sediment, a "sediment trap" was built and installed at the downstream end of the tank to prevent sediment transported out of the test area from reaching the pump.

The sediment used in the flume was divided into three categories according to grain size distribution. The largest quantity (category 1) was as purchased and contained sizes ranging from 0.2 mm to 0.8 mm (see Figure B.2). This sand was placed in regions of the test area where scour was not anticipated. The second category contained grain diameters ranging from 0.84 mm to 2.0 mm (see Figure B.3). This sand was used to cap the sand in category one. The cap was approximately 2 inches (5 cm) in depth. The third category had the size distribution shown in Figure B.4 and had diameters ranging from 0.42 mm to 0.84 mm. This sand occupied the central region of the test area. Figure B.1 shows the partition used in separating the central region during the sand placement process. The intent was to maintain a given sediment size distribution in the region of scour and to retard sediment motion in the areas away from the structure.

Since one of the objectives of the study was to measure the maximum scour, the flow rate and sediment size were selected so as to produce conditions as close to transition from clear water to live bed as possible while at the same time maintaining the depth mean velocity in the neighborhood of the 100 year design velocity (using Froude scaling). Froude scaling was used to determine the water depth, which was maintained approximately constant throughout both test series at approximately 1.25 ft (38 cm). The structure configurations used in the scour tests were 1) no pile cap (i.e. pile cap above the water line), 2) rectangular pile cap at the water surface, 3) rectangular pile cap resting on the bottom, 4) sloping (70° sides) pile cap at the water surface and 5) sloping (70° sides) pile cap resting on the bottom. The initial flow rate was set just below the computed value for transition. The five tests described above were then conducted at this flow rate.

After the scour tests on the pier structures described above were completed and the scour depths found to be significantly less than predicted by the methods presented in HEC-18 (1991), a decision was made to test a single cylinder under the same sediment, water depth and flow conditions and at an increased flow rate. The purpose of these tests was to determine if the conditions of the pier tests were close enough to transition (clear water to live bed) that maximum scour was occurring. The first cylinder test (conducted at the depth mean velocity used for the pier tests, 1.03 ft/sec) produced an ultimate scour depth ratio (scour depth/cylinder diameter) of 1.68. The second cylinder test (conducted at a velocity of 1.22 ft/sec) produced an ultimate scour depth ratio of 1.91, some 14% larger than that of the first test. The scour ratio of 1.91 matches the value obtained by Hannah (1978) for a single (circular) cylindrical pile with a similar aspect ratio. This indicates that the flow rates used for the pier tests were a bit low. Sand ripples formed away from the structure and sand was transported down the flume for every test conducted indicating a live bed condition, at least for a portion of the sand grains. However, more ripples formed and more sand was transported during the second test with the cylinder indicating the conditions were closer to transition for the D_{50} sediment. See Table 3 for the results of these tests as well as the computed scour depths for these conditions using the HEC-18 equation. To see if the 14% increase in scour depths found for the single cylinder could be applied to the multiple pile structure, an additional test was made on the pier with no pile cap at the higher flow rate. As with the cylinder the scour depth increased by approximately 14%. There was some

contraction scour during this test making these measurements not quite as precise as for the other tests. It therefore seems appropriate to apply a 14% scour depth correction to the mature scour depths near the leading edge of all five pier configurations.

Researchers have found that the rate of scour in model studies of approximately the scale of these tests is such that 90% of the ultimate scour takes place in approximately 24 hours model time (see e.g. Hannah (1978)). The duration of the scour tests reported on here are shown in Table 2 and ranged from 27.4 hours to 28.9 hours. For the purposes of estimating ultimate scour depth, the conservative (in the sense of giving a larger scour depth) assumption was made that the scour at the ends of these tests were produced in 24 hours. The scour process was recorded by sonar measurements, video and point gage measurements for all of the pier tests and by video and point gage measurements for the cylinder tests.

Results of Scour Experiments

The results of the scour experiments are presented in several ways. The scour depths for each structure from point gage measurements at the end of each test are given in Table 4. The scour depths for the model are given in feet and centimeters and for the prototype in feet and meters.

As stated earlier, with the exception of the first two or three rows of piles, it is difficult to know the maturity of the scour hole (i.e. how close the scour hole is to equilibrium). For this reason, no attempt was made to estimate equilibrium scour depths from the measured scour beyond the first few rows of piles. This estimated equilibrium data was used to evaluate the coefficients in Equation 2. Contours of the measured scour are shown in Figures C.15 and C.17. The fact that the scour hole is in various stages of development from the front to the back of the pier should be kept in mind when viewing these Figures. Measured profiles normal to the pier at selected values of x are shown in Figures C.1 - C.12.

PART C: Overall Results and Conclusions

Merrill-Barber Bridge Piers

The equilibrium maximum sediment scour depths that occur at transition from clearwater to live bed for the pier configurations considered in this study are given in Table 4. The values presented in this Table are based primarily on results of the scour experiments and represent the authors best estimates of scour depths for the pier designs proposed for the Merrill-Barber Bridge. They take into consideration the fact that the scour experiments were conducted at velocities slightly below transition (i.e. the measured depths were increased by 14%) and the fact that at the upstream end of the pier the measured scour depths are only 90% developed. A more detailed discussion of this subject is presented in

Appendix B. The results of the hydrodynamic study can provide predictions of equilibrium scour depths for the area where bottom shear stresses are known. Selected bottom profiles are presented in Figures 2 - 19. Note that the scour depths for skew angles greater than zero were computed from the pre-scoured bottom shear stress measurements and scour measurements do not exist for these cases. The values appear to be reasonable but they should be used with caution.

Use of Prescoured Bottom Shear Stress to Estimate Local Scour

One of the objectives of this study was to determine if equilibrium local scour depths could be predicted from prescoured bottom shear stress measurements. Even though additional work is needed before definite conclusions regarding the feasibility can be made, the results look very promising. The predictions made with the simplistic model developed as part of this study are reasonable and appear to fit the scour at those locations believed to be close to equilibrium. The scheme also gives estimates of scour depths at locations that are far from equilibrium that are consistent with the rate of scour plots for those areas. That is, the predicted equilibrium scour depths are reasonable extrapolations of the measured values at locations where the rate of scour plots indicate that the scour is far from equilibrium.

Due to time and cost constraints flow measurements adjacent to the piles were not made in this study. A special constant temperature probe support is needed for these measurements and it was not available. As a result the shear stress for these areas had to be extrapolated from the values along the side of the pier. The values of shear stress needed to predict the equilibrium scour depths obtained from the scour measurements fall within the range of values measured by other investigators (Carstens and Sharma (1975)). A series of tests are needed where shear stress is measured much closer to the piles. In addition, structure shapes other than the ones considered here need to be tested to determine the universality of the coefficients obtained in this study.

General Comments

The results of a number of researchers including the authors of this report (see Sheppard et al. (1992)) indicate that the maximum local structure-induced scour occurs just prior to transition from clear water to live bed scour. As velocities increase in the live bed regime sand waves can form and propagate through the test area. The combination of local scour and sand wave trough depth will produce a second local maximum scour depth which may or may not exceed the transition maximum, depending on, among other things, the sediment size (see Melville (1984)). The scour measured in these tests is limited to "structure-induced local scour" and does not contain sand waves of any significant size. The presence of sand waves (coupled with local scour) could thus produce a scour hole deeper than the values obtained in these tests. Sand wave heights can be estimated using expressions given in the literature (see e.g. Raudkivi and Witte (1990), van Rijn (1984)).

The results of the hydrodynamic tests and the rate of scour plots indicate that the time required to reach equilibrium scour depths increases with distance from the leading edge of the pier. This is an important finding that helps interpret the results of this and other studies. The rate of scour for the front rows of piles seems to be similar to that of a single pile structure. The time required to reach equilibrium scour depths at piles downstream from the leading edge can be significant.

Flow misalignments (i.e. skew angles) of 7.5° and 15° were examined in the hydrodynamic tests. Scour predictions based on bottom shear stress for these cases do not have scour data to back them up but they seem reasonable.

Reversing flows such as might occur during a hurricane could scour the other end of the structure and perhaps fill or partially fill in the original scour hole. Even if the scour hole is filled by the reverse flow the load bearing properties of this newly deposited sediment are questionable and should be disregarded until tests can be conducted to prove otherwise.

The sloping (70°) pile cap does not significantly alter the maximum scour depth in any of the positions tested. The reduction in scour is only 4.6% for the pile cap at the bottom and 3.4% for the pile cap at the surface. This result is somewhat surprising since the dominant scour mechanism for these bluff bodies appears to be the "horseshoe vortex" generated on the leading face of the structure.

The scour tests were performed for two positions of the pile cap; resting on the bottom and located at the water surface (i.e. the top of the pile cap just above the water surface). Three pile cap positions (bottom, mid depth and surface) were investigated in the hydrodynamic tests. At the end of the 28 hour scour tests the scour depths were greater for the pile cap at the surface than at the bottom. This, most likely, will be true for equilibrium scour depths as well but it could be that the scour hole is much less developed for the case when the pile cap is at the bottom. Unfortunately the hydrodynamic (shear stress) test results are not helpful for this situation due to their inability to predict scour when the structure-flow configuration changes dramatically as a result of the scour. Longer duration scour tests are needed to resolve this question.

The presence of a number of piles and a massive pile cap such as that investigated here has two somewhat opposing effects on the sediment scour potential. The turbulence intensity (and presumably the bottom shear stress) increases with the number of bluff structural elements (piles) but as the number of piles increase the flow velocity within the structure is retarded thereby reducing the flow through the structure and the bottom shear stress. It appears that the extent and volume of scour must be a function of the number of in-line piles as well as the size, shape, spacing, etc. Thus, for a given pile shape, size and spacing there could be a maximum extent to the scour with regard to the number of piles in the in-line direction. The pier designs considered in these tests seems to have exceeded the point of maximum extent of scour in that the predicted scour depths for the downstream piles is significantly less than for those at the upstream end.

Rate of scour is obviously an important aspect of local structure-induced sediment scour in the coastal environment. Using Froude scaling laws, 28 hours in the flume corresponds to approximately 108 hours or 4.5 days for the prototype. Froude scaling for rate of scour is probably not appropriate since prototype sediment and water are being used in the flume studies. Nevertheless it is obvious that a significant amount of time is required for the entire scour hole to reach equilibrium. The rate of structure-induced scour problem is presently under investigation by the author. Data from this and other similar studies will hopefully lead to a better understanding of the mechanisms involved and ultimately to predictive models.

Table 1. Sequence of Hydrodynamic Tests

Test Number	Pile Cap Type	Pile Cap Position	Flow Skew Angle
1	No Pile Cap	NA	0°
2	70° Pile Cap	Top	0°
3	70° Pile Cap	Mid	0°
4	70° Pile Cap	Bottom	0°
5	90° Pile Cap	Top	0°
6	90° Pile Cap	Mid	0°
7	No Pile Cap	NA	7.5°
8	70° Pile Cap	Top	7.5°
9	70° Pile Cap	Mid	7.5°
10	No Pile Cap	NA	15°
11	90° Pile Cap	Top	15°
12	90° Pile Cap	Mid	15°

Table 2. Sequence of Scour Tests

Test Number	Structure	Velocity (ft/sec)	Flow Depth (ft)	Duration of Test (hours)
1	No Pile Cap	1.03	1.28	28.3
2	90° Pile Cap (Top Position)	1.03	1.28	27.4
3	90° Pile Cap (Bottom Position)	1.03	1.28	28.9
4	70° Pile Cap (Top Position)	1.03	1.28	28.6
5	70° Pile Cap (Bottom Position)	1.03	1.28	28.1
6	4 inch Cylinder	1.03	1.28	7.1
7	4 inch Cylinder	1.22	1.31	7.0
8	No Pile Cap	1.22	1.31	24.7

Table 3. Calibration Tests

Test No.	Structure	Water Depth (ft)	Velocity (ft/sec)	Duration (hr)	Equilibrium Scour Depth (ft)	HEC-18 Scour Depth (ft)
				Scour Depth (ft)		
6	4in Dia. Cylinder	1.28	1.03	7.1	0.56	0.49
				0.446		
7	4in Dia. Cylinder	1.31	1.22	7.0	0.64	0.525
				0.509		

Table 4. Maximum Scour Depths

Structure	Model						Prototype	
	Scour Depth ¹		Equilibrium Maximum Scour Depth		Corrected Equilibrium Maximum Scour Depth		Corrected Maximum Scour Depth	
	ft	cm	ft	cm	ft	cm	ft	m
No Pile Cap	0.54	16.6	0.60	18.4	0.71	21.7	10.59	3.3
90° Pile Cap (Top Position)	0.76	23.2	0.84	25.8	0.95	29.0	14.25	4.4
90° Pile Cap (Bottom Position)	0.67	20.5	0.74	22.8	0.85	26.0	12.75	3.9
70° Pile Cap (Top Position)	0.73	22.4	0.81	24.9	0.92	28.1	13.75	4.2
70° Pile Cap (Bottom Position)	0.64	19.6	0.71	21.8	0.82	25.0	12.25	3.8

¹Scour depths are measured from the initial bottom and are positive down.

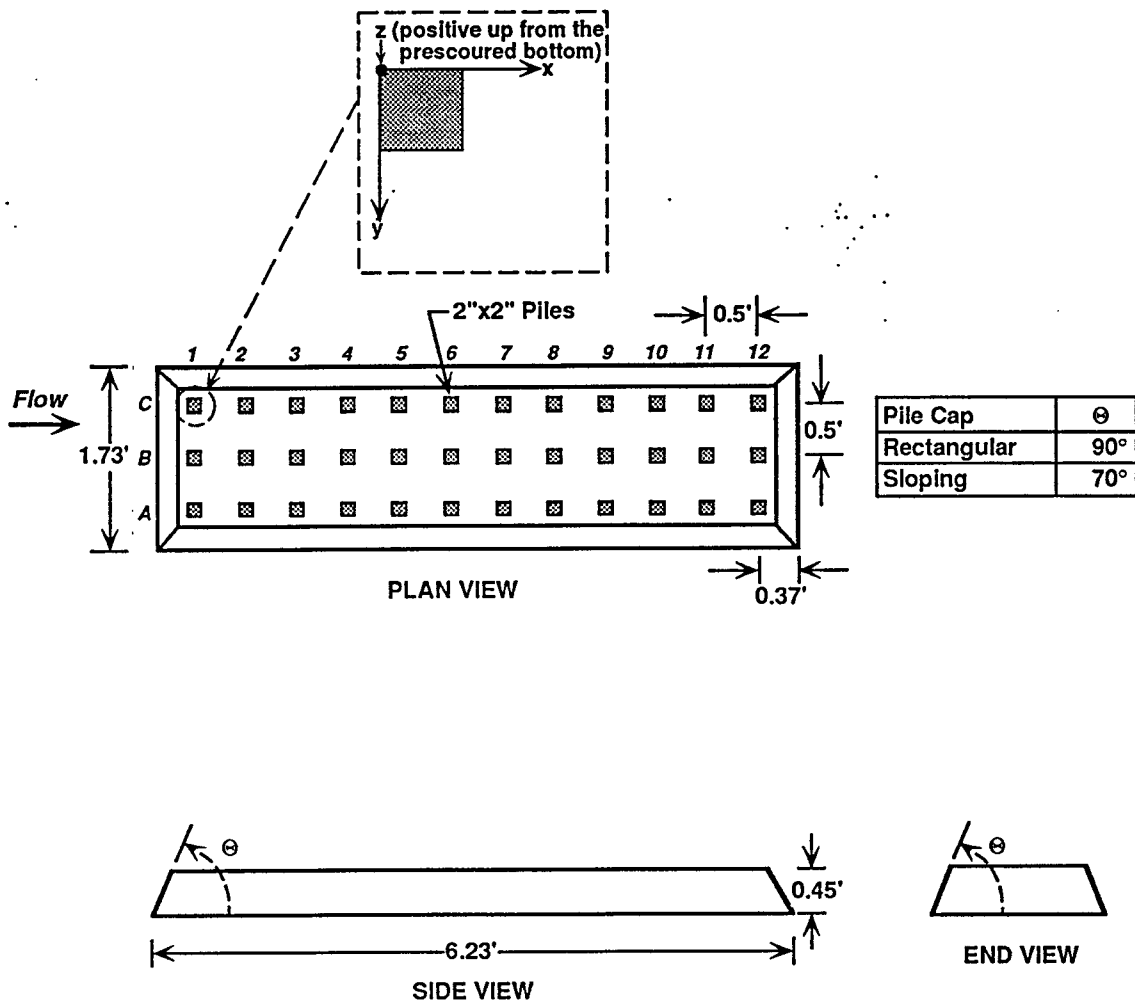


Figure 1 Definition sketch of pile cap.

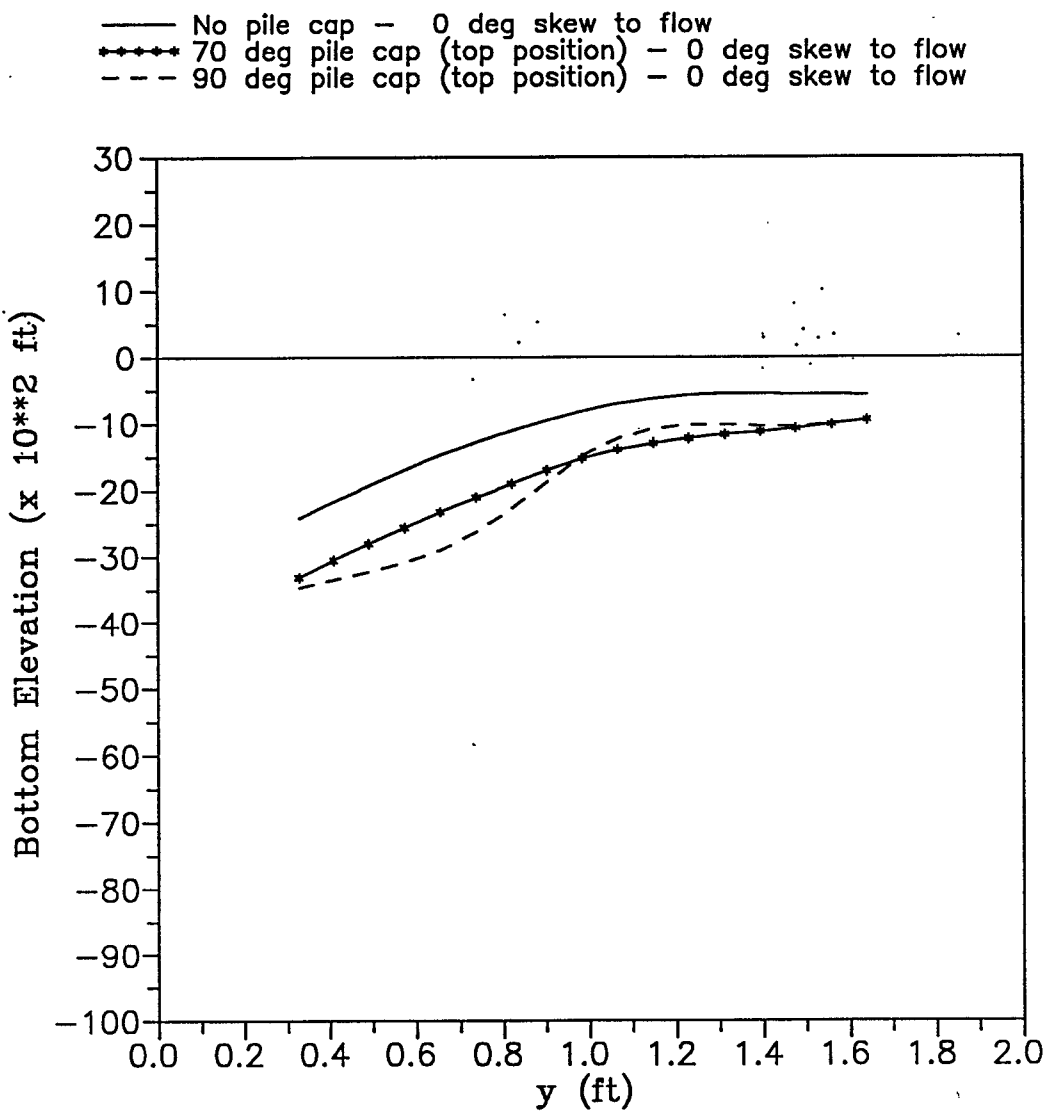


Figure 2 Predicted bottom elevation (row 3, x = 1.31 ft)
 (see Figure A.3 for definition of axes).

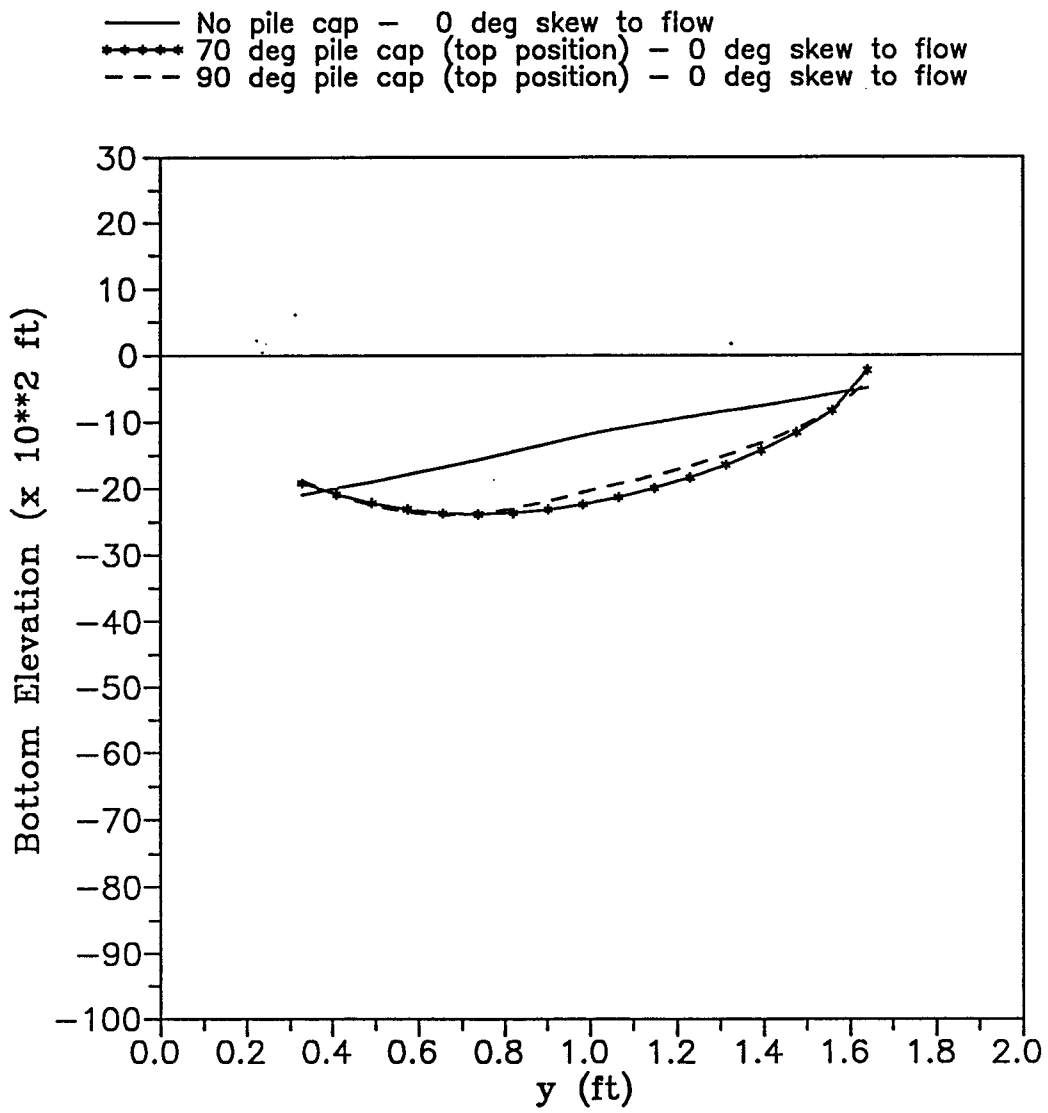


Figure 3 Predicted bottom elevation (row 5, x = 3.28 ft)
 (see Figure A.3 for definition of axes).

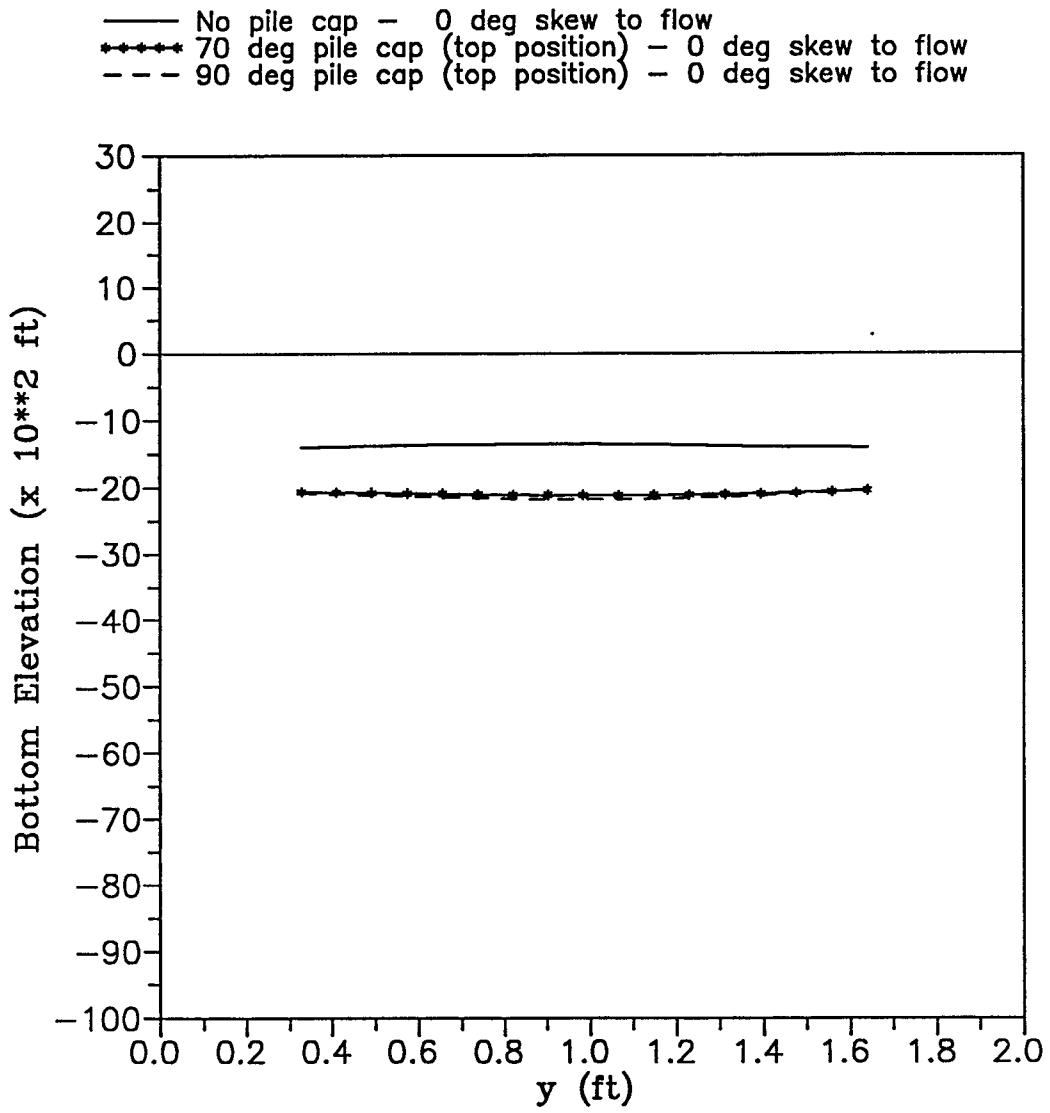


Figure 4 Predicted bottom elevation (row 7, x = 5.25 ft)
 (see Figure A.3 for definition of axes).

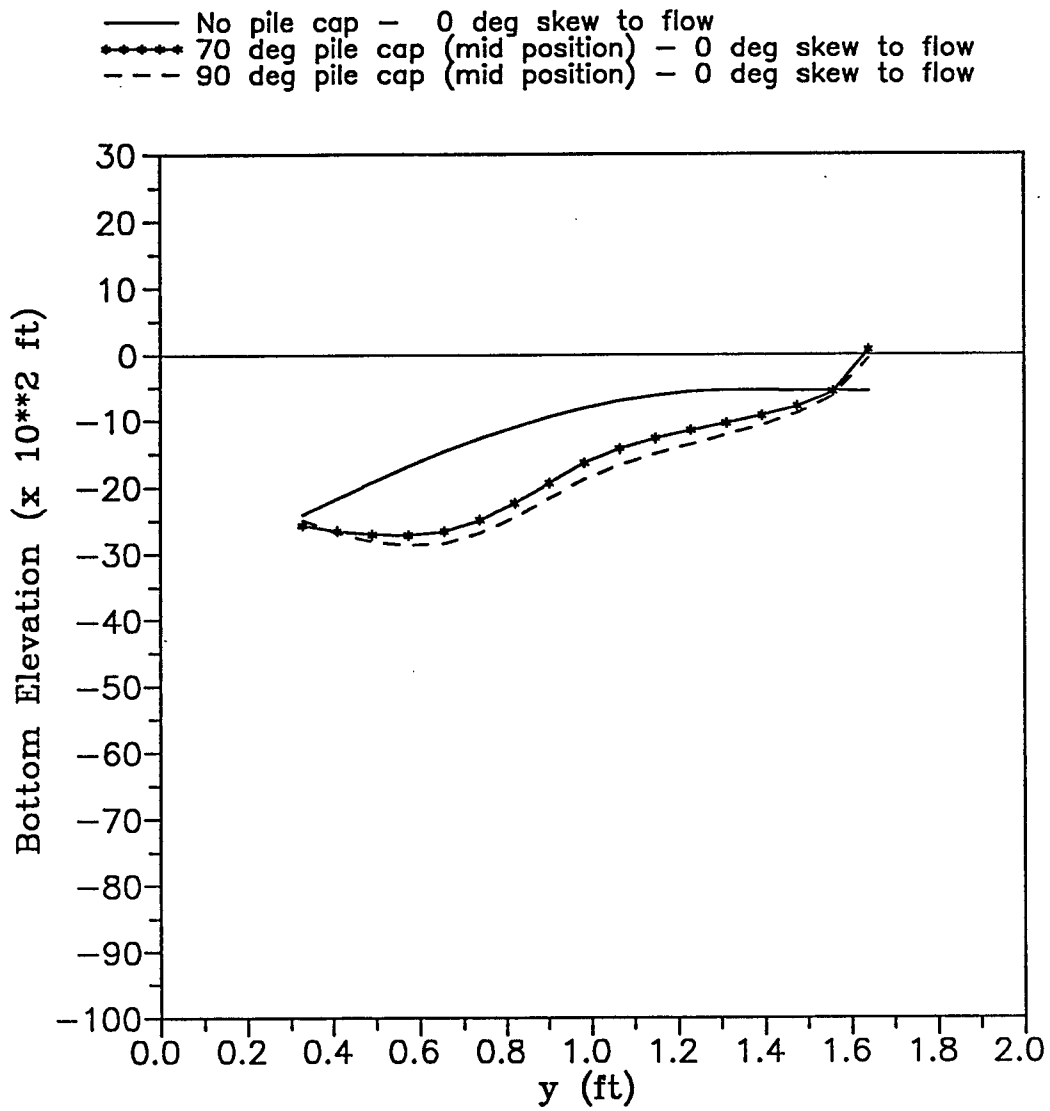


Figure 5 Predicted bottom elevation (row 3, $x = 1.31$ ft) (see Figure A.3 for definition of axes).

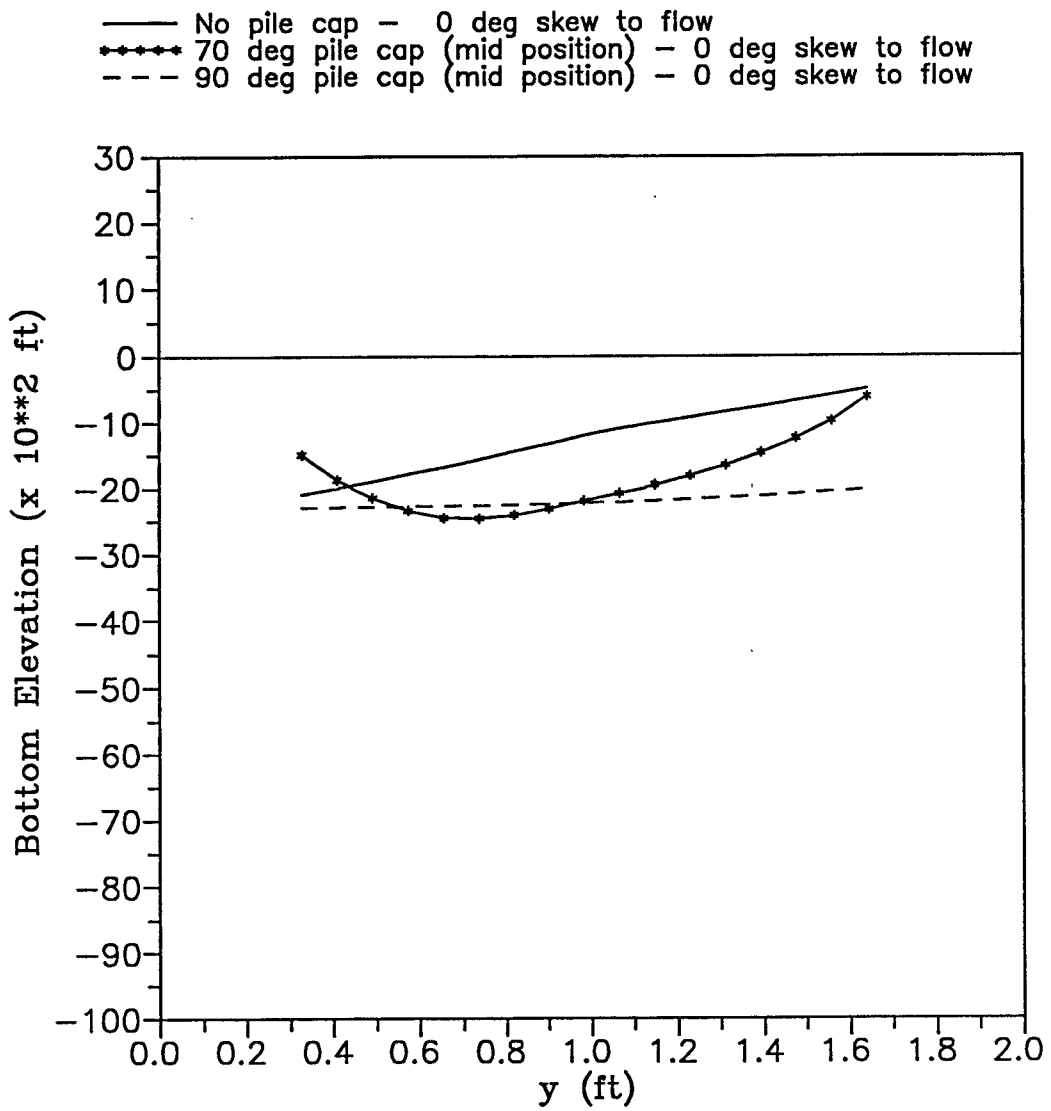


Figure 6 Predicted bottom elevation (row 5, $x = 3.28$ ft)
 (see Figure A.3 for definition of axes).

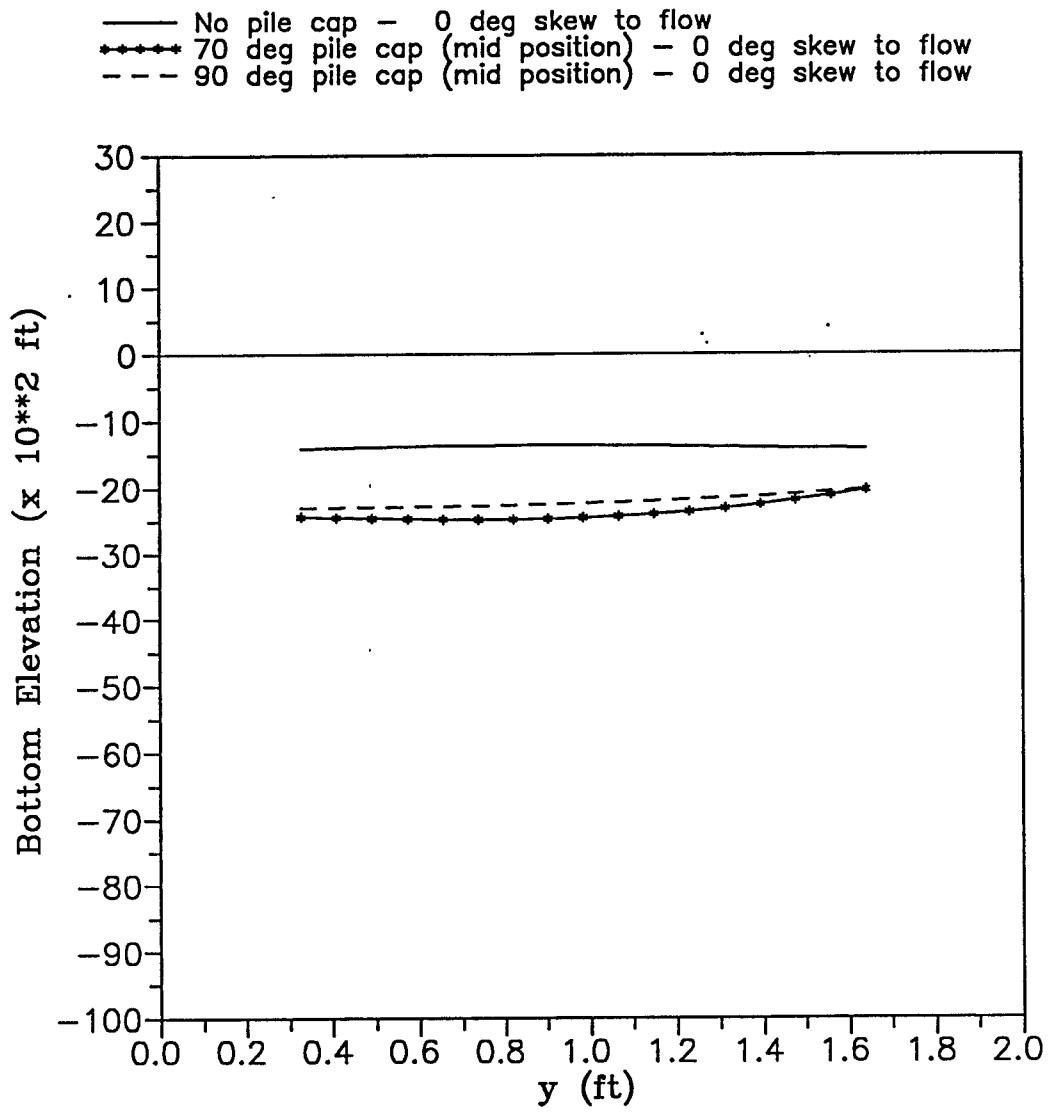


Figure 7 Predicted bottom elevation (row 7, x = 5.25 ft)
 (see Figure A.3 for definition of axes).

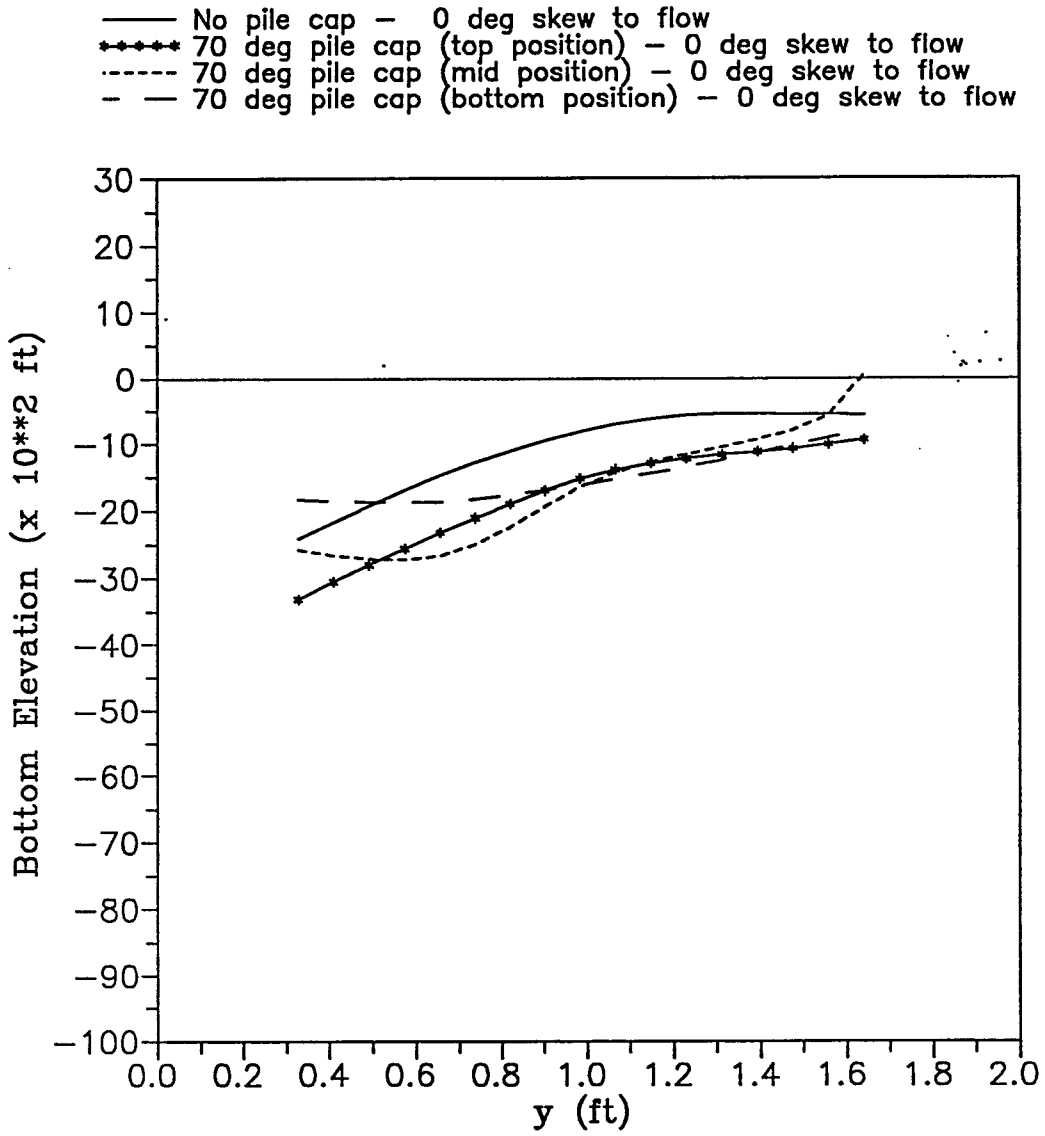


Figure 8 Predicted bottom elevation (row 3, $x = 1.31$ ft) (see Figure A.3 for definition of axes).

- No pile cap — 0 deg skew to flow
- ◆◆◆◆ 70 deg pile cap (top position) — 0 deg skew to flow
- 70 deg pile cap (mid position) — 0 deg skew to flow
- - - 70 deg pile cap (bottom position) — 0 deg skew to flow

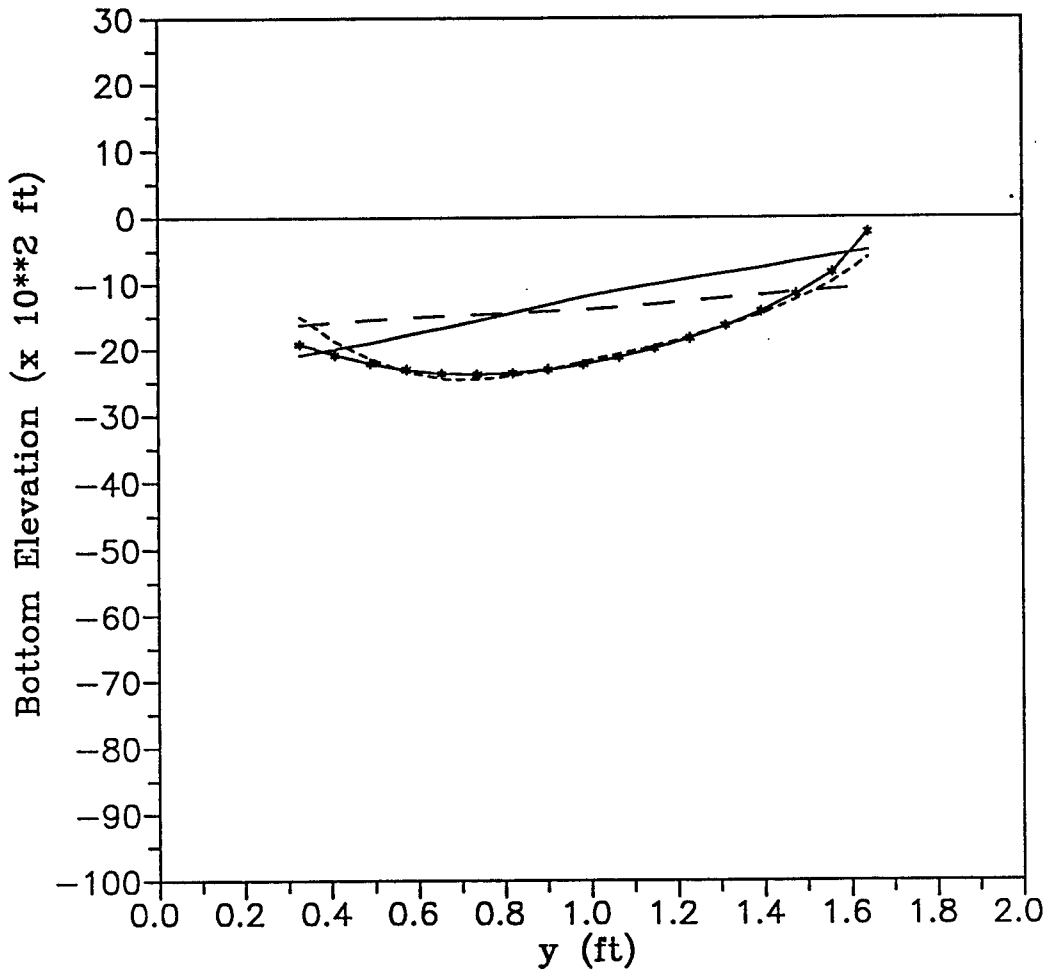


Figure 9 Predicted bottom elevation (row 5, x = 3.28 ft)
 (see Figure A.3 for definition of axes).

- No pile cap — 0 deg skew to flow
- 70 deg pile cap (top position) — 0 deg skew to flow
- - - 70 deg pile cap (mid position) — 0 deg skew to flow
- - - 70 deg pile cap (bottom position) — 0 deg skew to flow

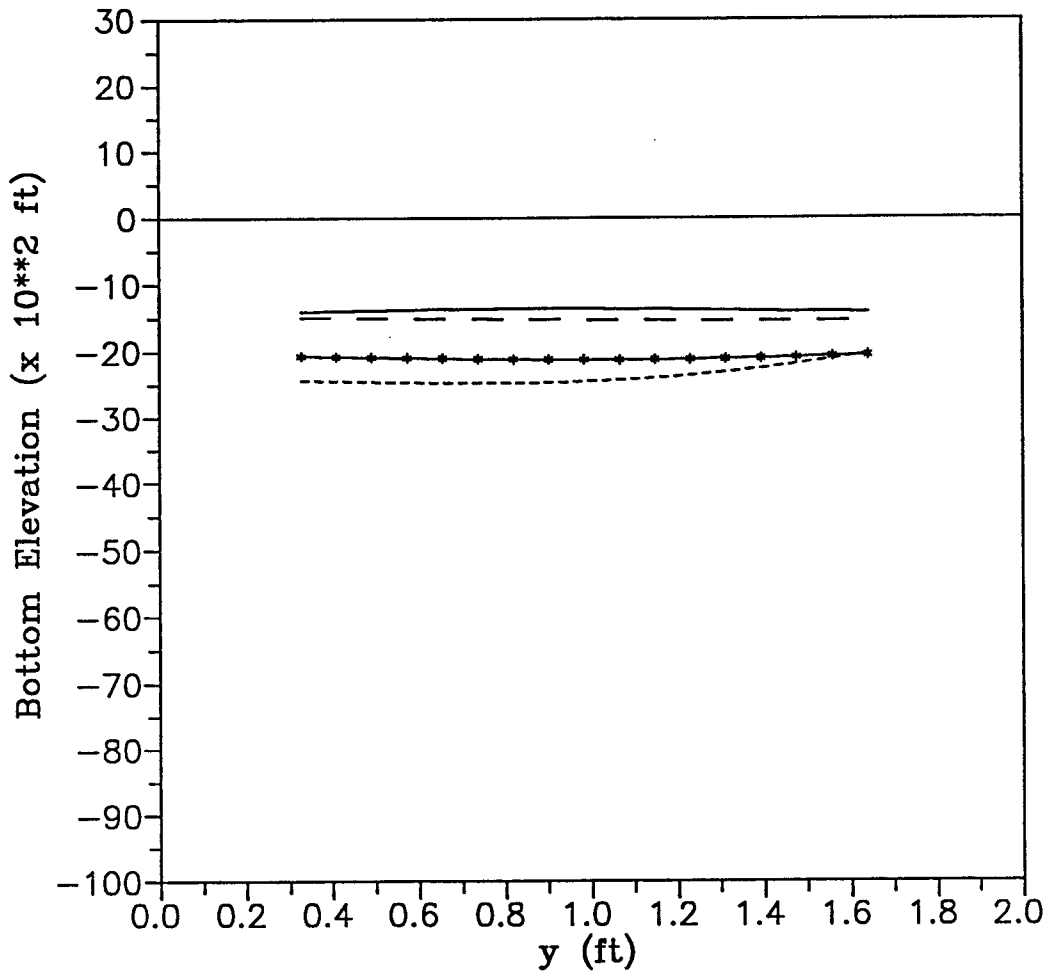


Figure 10 Predicted bottom elevation (row 7, x = 5.25 ft)
 (see Figure A.3 for definition of axes).

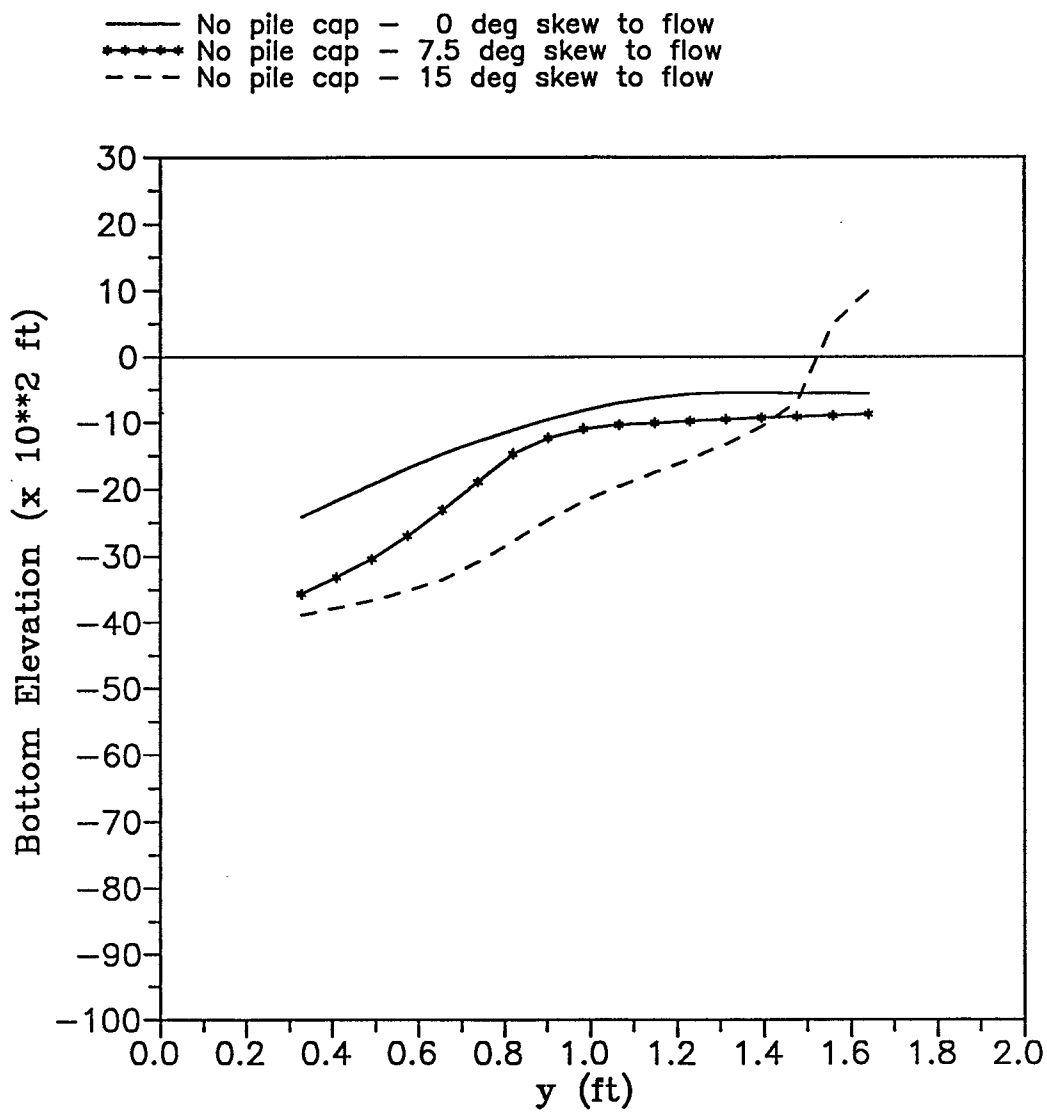


Figure 11 Predicted bottom elevation (row 3, $x = 1.31$ ft) (see Figure A.3 for definition of axes).

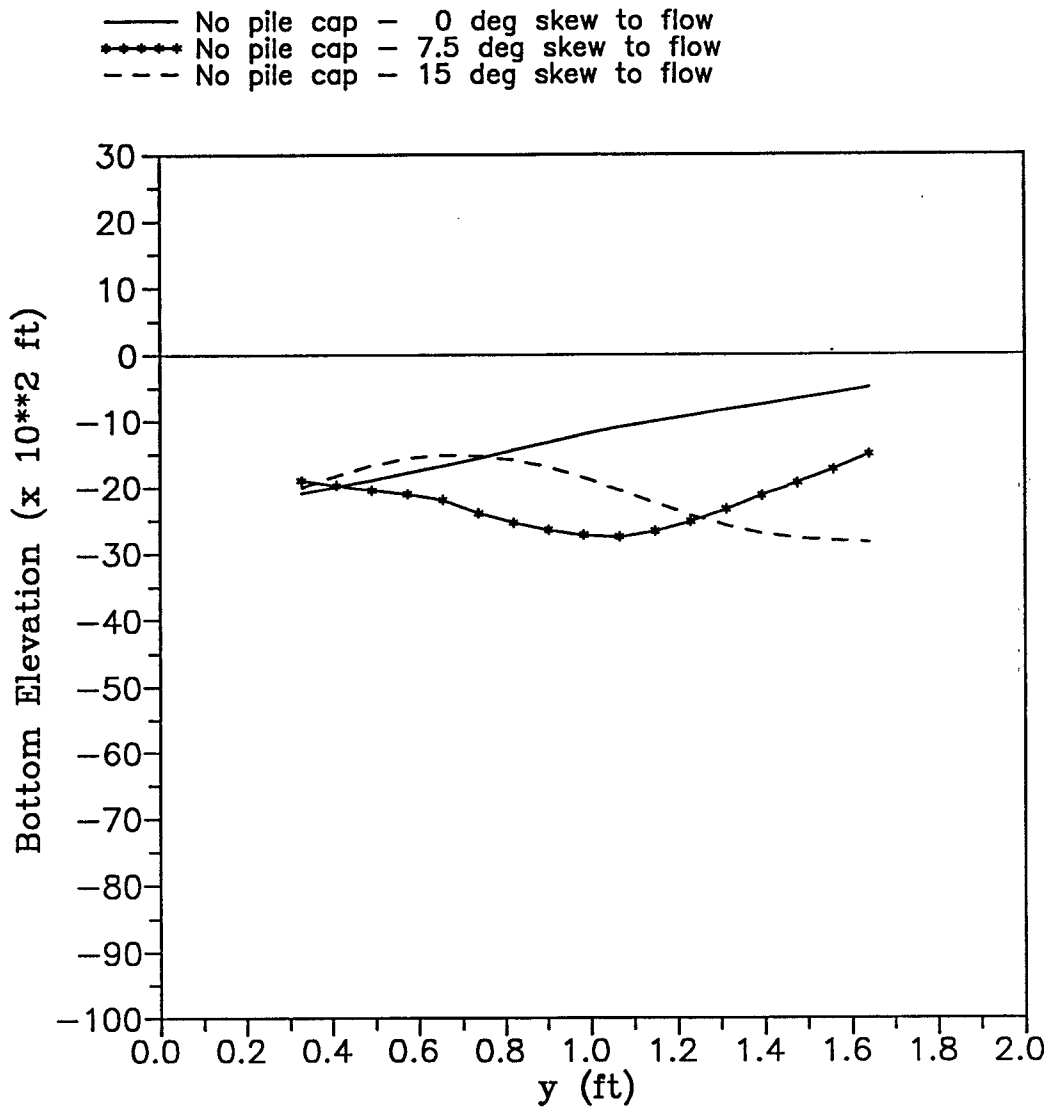


Figure 12 Predicted bottom elevation (row 5, $x = 3.28$ ft) (see Figure A.3 for definition of axes).

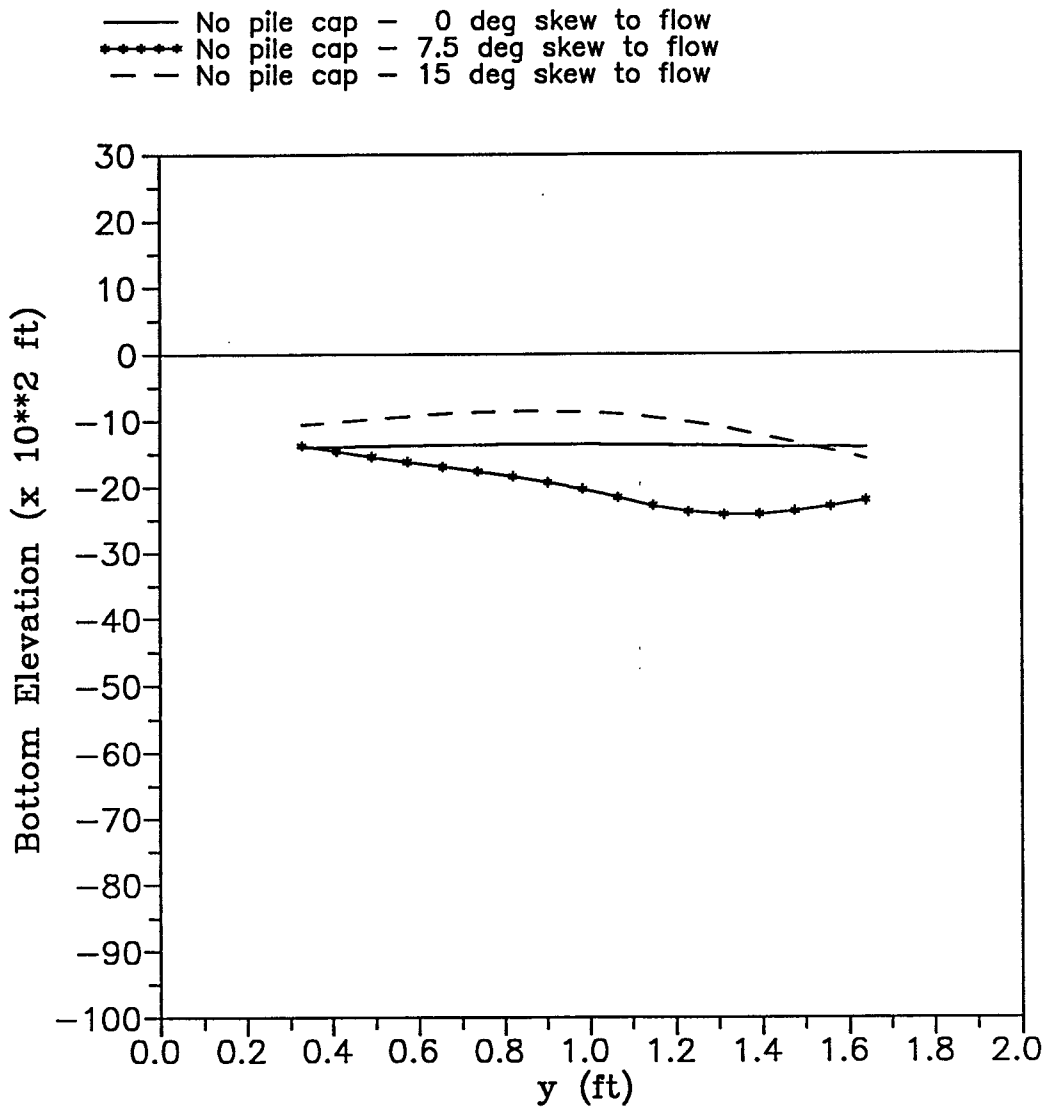


Figure 13 Predicted bottom elevation (row 7, x = 5.25 ft)
 (see Figure A.3 for definition of axes).

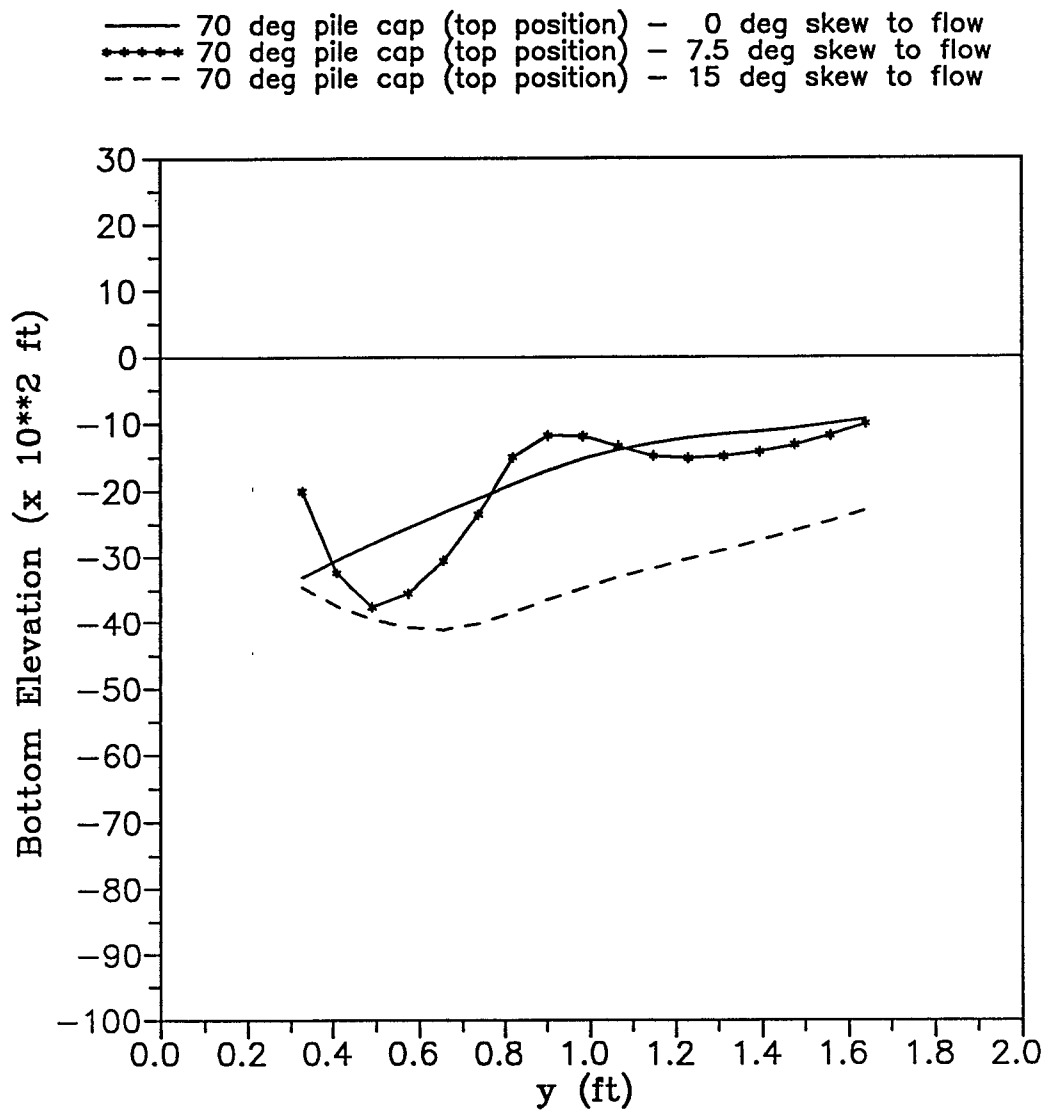


Figure 14 Predicted bottom elevation (row 3, $x = 1.31$ ft)
 (see Figure A.3 for definition of axes).

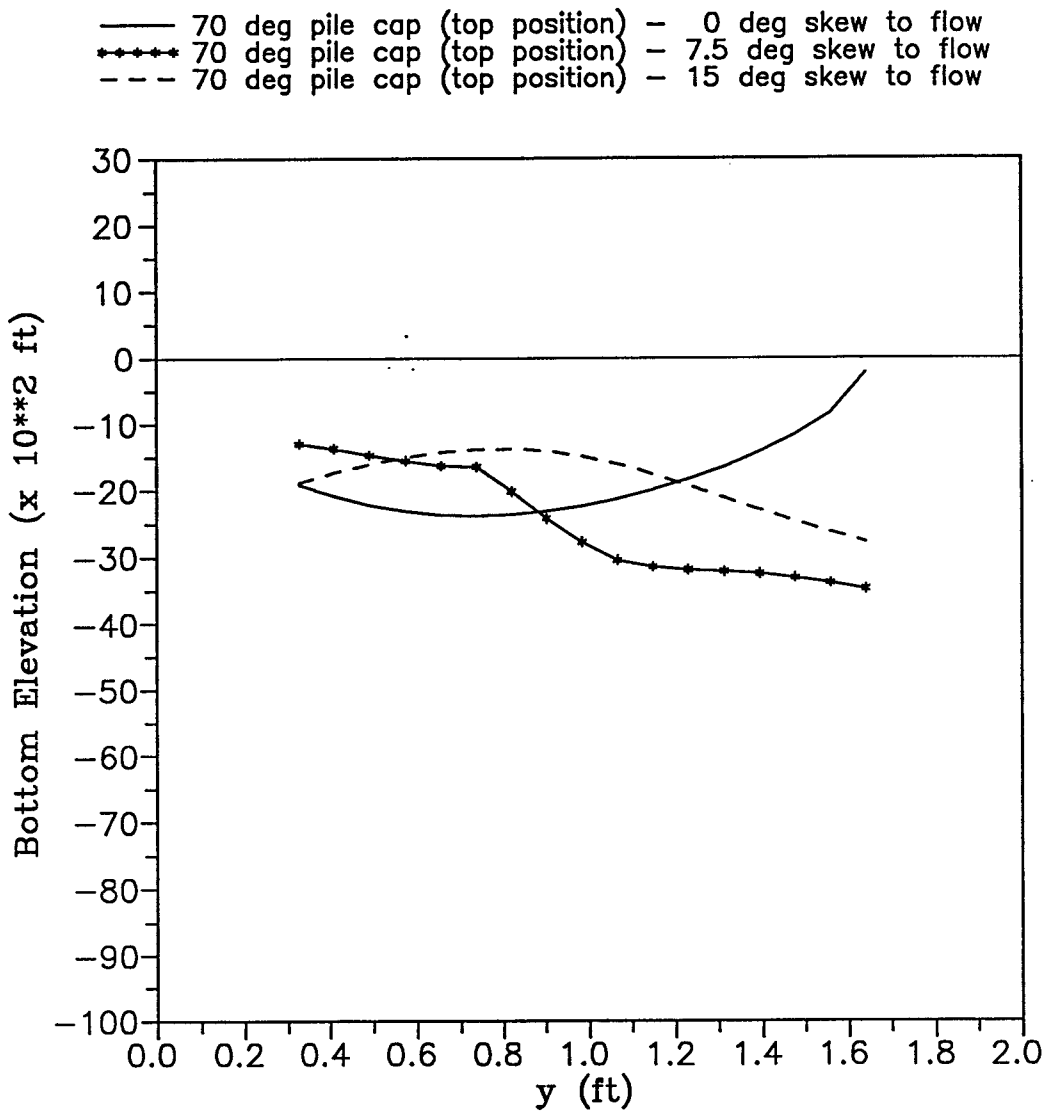


Figure 15 Predicted bottom elevation (row 5, $x = 3.28$ ft)
 (see Figure A.3 for definition of axes).

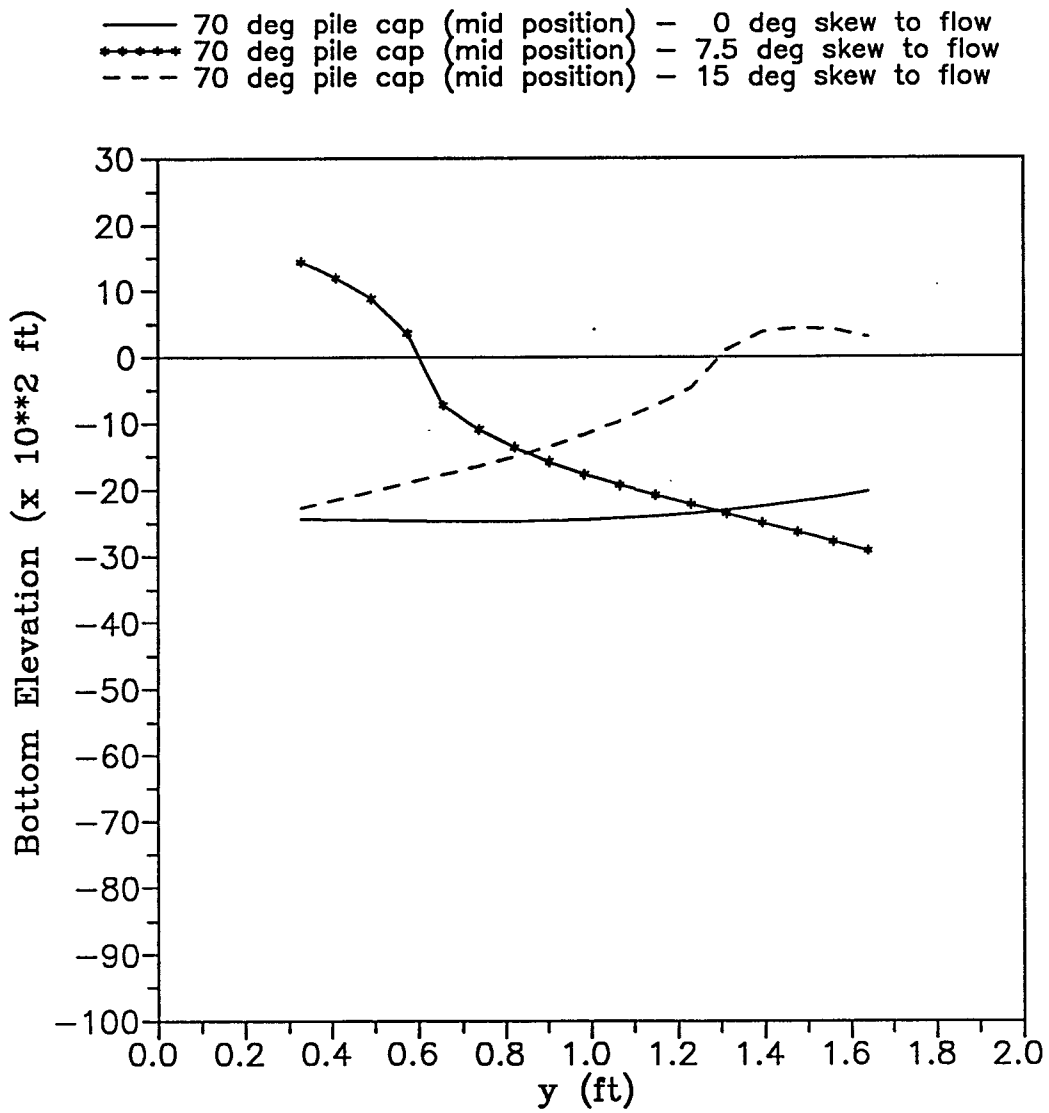


Figure 16 Predicted bottom elevation (row 7, $x = 5.25$ ft)
 (see Figure A.3 for definition of axes).

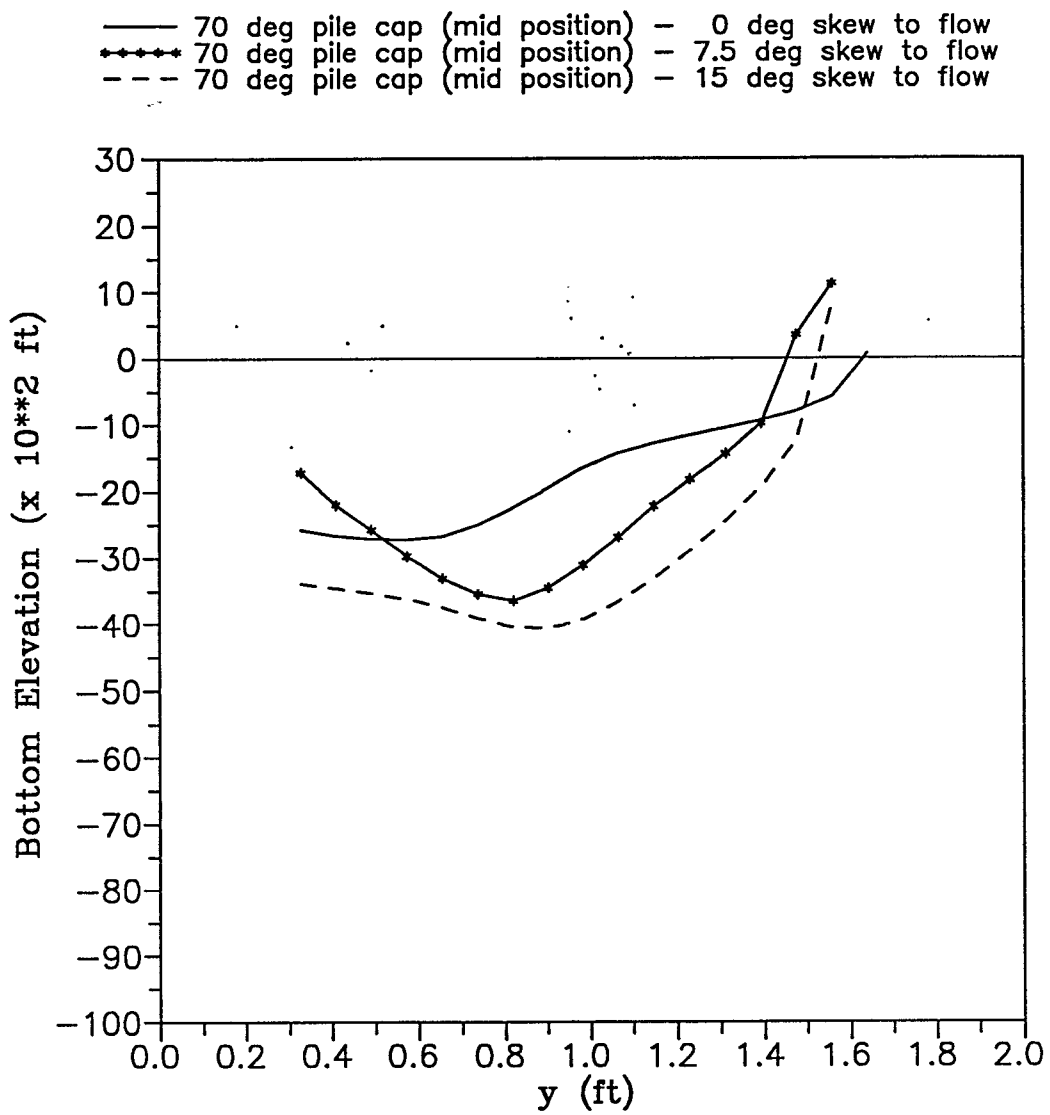


Figure 17 Predicted bottom elevation (row 3, $x = 1.31$ ft)
 (see Figure A.3 for definition of axes).

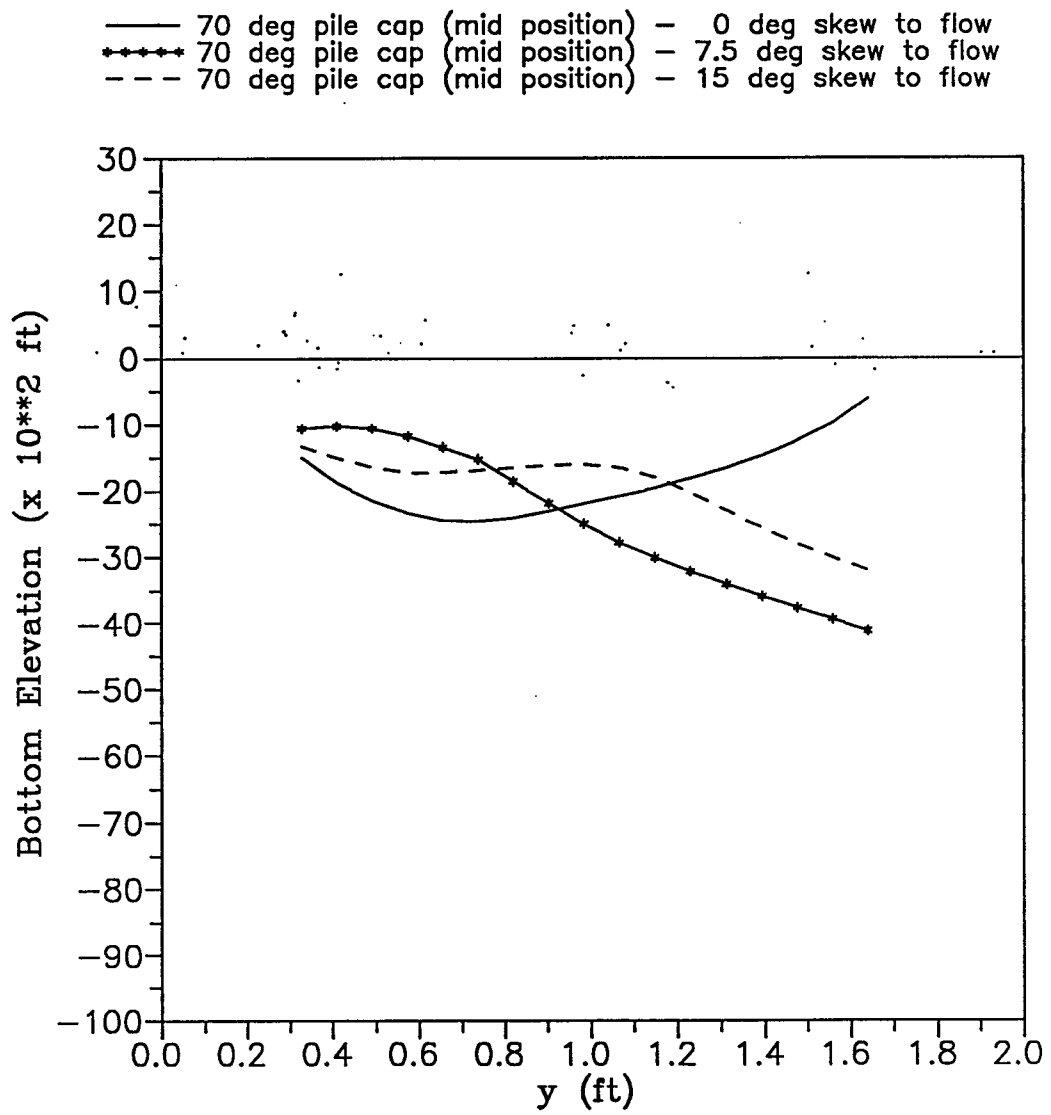


Figure 18 Predicted bottom elevation (row 5, $x = 3.28$ ft)
 (see Figure A.3 for definition of axes).

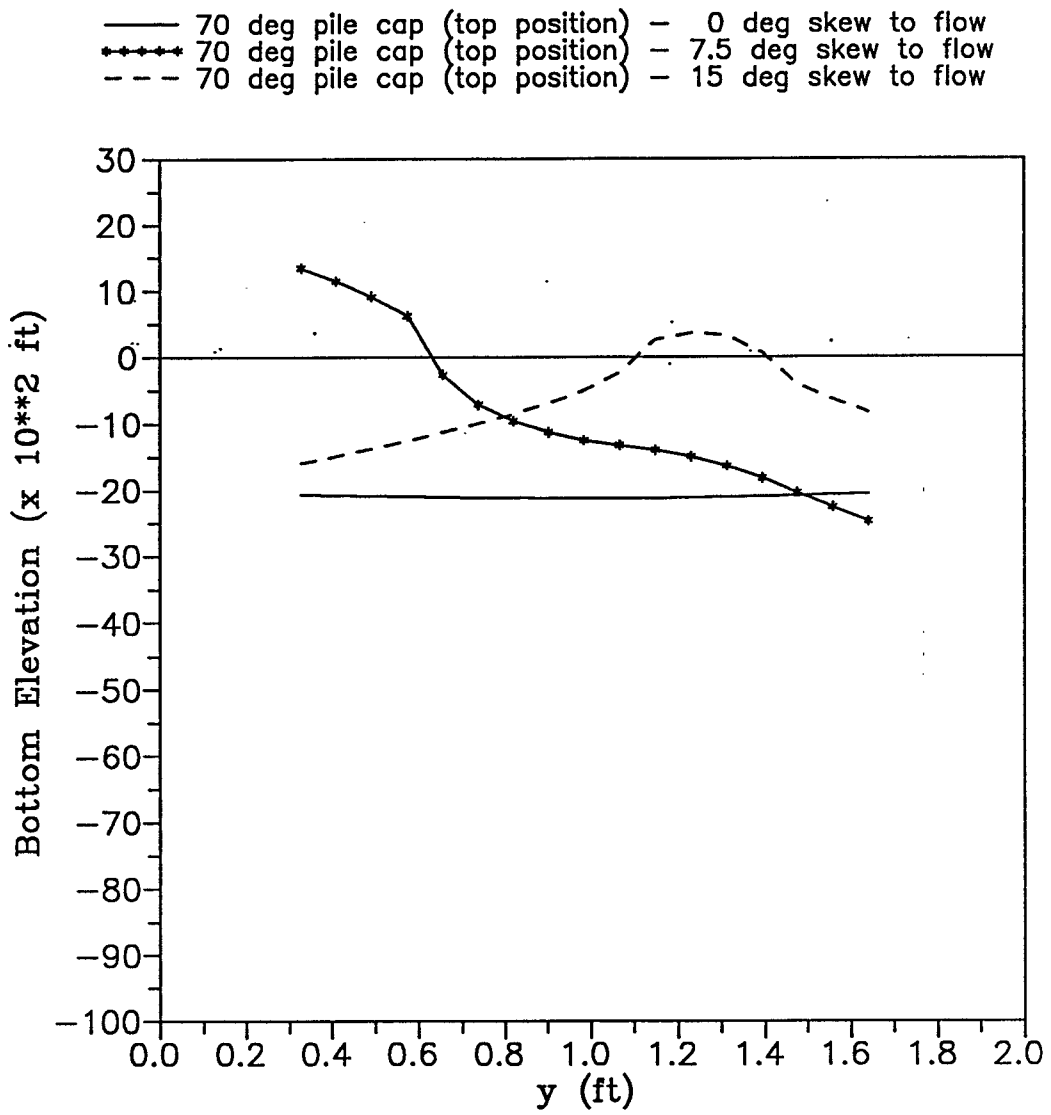


Figure 19 Predicted bottom elevation (row 7, x = 5.25 ft)
 (see Figure A.3 for definition of axes).

REFERENCES

- Brown, C.B. (1950), "Sediment Transportation." In Engineering Hydraulics, H. Rouse, Ed. Wiley, New York.
- Carstens, T. and H.R. Sharma (1975), "Local Scour Around Large Obstructions." Int. Assoc. for Hydraul. Res., 16th Congr., Proc., V.2, Subj. B, 251-262.
- Chang, F.M., D.B. Simons and E.V. Richardson (1967), "Total Bed-Material Discharge in Alluvial Channels." Proc. 12th Cong. IAHR, Fort Collins, Colorado.
- Du Boys, M.P. (1879), "le Rhône et les rivières à lit affouillable." Mem. Doc. Ann. Ponts Chaussées. Ser.5, No.18, 141-195.
- Garde, R.J. and M.L. Albertson (1958), Discussion of "The Total Sediment Load of Streams." by E.M. Laursen, Proc. A.S.C.E., J. Hydraulics Div., Vol.84, No.HY6, 1856-59-64.
- Hannah, C.R. (1978) "Scour at Pile Groups." Master of Engineering Thesis at the University of Canterbury, New Zealand, 92 p.
- HEC-18, (1991) Hydraulic Engineering Circular No. 18, "Evaluating Scour at Bridges." Pub. No. FHWA-IP-90-017.
- Melville, B.W. (1984) "Live-Bed Scour at Bridge Piers." J. of Hydraulic Engineering, V.110, No.9, 1234-1247.
- O'Brien, M.P. and B.D. Rindlaub (1934), "The Transportation of Bed-Load by Streams." Trans. A.G.U., Vol.15, 593-603.
- Raudkivi, A.J. and H.H. Witte (1990), "Development of Bed Features." J. of Hydraulic Engineering, V.116, No.9, 1063-1079.
- Sheppard, D.M. and A. W. Niedoroda (1992) "Structure-Induced Sediment Scour - Local Scour Bounds & Assessment of Global Scour." Final report to Florida Department of Natural Resources, PR 4910451123412 UPN No. 90100412, 84 pages.
- Shields, A. (1936), "Anwendung der aehnlichkeitsmechanik und der turbulenz forschung auf die geschiebebewegung." Mitt. Preuss. Versuchsanstalt Wasserbau Schiffbau, Berlin, No.26.
- van Rijn, L.C. (1984), "Sediment Transport, Part III: Bed Forms and Alluvial Roughness." J. of Hydraulic Engineering, V.110, No.12, 1733-1754.

ACKNOWLEDGEMENTS

The authors would like to thank the Florida Department of Transportation District IV Office for supporting this research. The technical insight and input throughout this study by Mr. Roberto Perez, P.E. and Mr. Rick Renna, P.E. with FDOT has been most helpful and appreciated. Mr. Sterling Jones with the Federal Highway Administration (FHWA) also provided helpful suggestions at various points in the project. A number of graduate students headed by Maximo Ramos worked on different aspects of this study. They include Mike Dombrowski, Kailash Krishnamurthy, Suresh Maddula and Andrade Prashant. Thanks to Mr. Rick Renna, P.E. (FDOT) and Mr. Frank Balsamo, P.E. (Parsons Brinckerhoff Quade and Douglas, Inc.) for their work on the contract administration. Also, thanks to Ms. Laura Dickinson for her assistance with data reduction and word processing.

APPENDIX A
HYDRODYNAMIC STUDY

HYDRODYNAMIC STUDY

A.1 Background

As stated in the introduction, the primary objective of this study was to determine if local scour depths can be predicted from near-bottom flow measurements over the pre-scoured bed near the structure. The hydrodynamic study with the fixed bed is discussed in this appendix and details of the scour study are discussed in Appendix B.

Sediment transport is a complex process but it is generally believed that the movement of sediment is related to the shear stress at the bed. For this reason, an attempt was made to estimate the bottom shear stress from flow measurements at a fixed distance above the bed 0.12 in (3 mm). In a fully developed open channel flow, estimation of the bottom shear stress is relatively straight forward. This is not the case for the complex "wake region" near a multiple pile structure and certain assumptions regarding the stress distributions had to be made. To further complicate the situation, the mean flow direction near the structure was found to vary with time as a result of the vortices being alternately shed by the piles and pile cap.

A two component Dantec 56C01 constant temperature anemometer was used for the flow measurements (see Table A.1). The response of the Dantec R61 X sensor probe used was such that the high frequency fluctuating components of the velocity could be measured (see Table A.2). It was determined that when the X sensor probe was mounted such that the filaments lie in parallel vertical planes, variations in the mean velocity direction in a horizontal plane could not be resolved. That is, when the probe is oriented to measure velocities in the x (horizontal) and z (vertical) directions, changes in the direction of the horizontal velocity were not detected. This is to be expected since the probe is not designed for this flow situation. This means that the turbulent component of the shear stress, $-\rho \overline{u'v'}$, could not be accurately measured near the structure where the horizontal component of velocity undergoes fluctuations in direction as large as $\pm 30^\circ$. Ordinarily, the in line horizontal and the vertical velocities would be measured and the mean horizontal velocity, \bar{U} , and time average of the product $u'w'$ computed in order to determine the total horizontal shear stress

$$\tau = \mu \frac{\partial \bar{U}}{\partial z} - \rho \overline{u'w'} . \quad (\text{A.1})$$

To avoid the problem of the probe not being able to resolve variations in flow direction, it was decided to rotate the probe 90° so that the filaments were in parallel, horizontal planes. In this position, the probe measures the two horizontal components of velocity, U and V. It was assumed that the turbulent shear stress is proportional to $\rho(u'^2 + v'^2)$. The total shear stress would then be

$$\tau = \mu \frac{\partial \bar{U}}{\partial z} + a\rho(u'^2 + v'^2) \quad (\text{A.2})$$

where "a" is a constant to be determined from measurements in front of the structure at $x = -4.92$ ft and $z = 0.12$ in (3 mm). The analysis resulted in a value of 0.10 for "a".

The value of "a" was computed using the expression:

$$a = \frac{-\overline{u'v'}}{(u'^2 + v'^2)}$$

It was evaluated at a point in front of the structure at different heights above the bottom ($z = 0.93, 4.15$ and 7.38 in) and found to vary between 0.08 and 0.12. The value of "a" ranged from 0.04 to 0.09 next to the structure. The lower values of "a" next to the structure were probably due to the inability of the X sensor probe to resolve horizontal variations in the mean flow direction larger than $\pm 30^\circ$. Based on the above, a value of 0.10 for "a" was used throughout the flow field.

Figure A.1 compares the shear stress profiles in front of and away from the influence of the structure computed using Equations A.1 and A.2. The shear stress profiles are similar and at $z = 0.12$ in (3 mm) both give the same value for τ (4.59×10^{-3} lb_f/ft²). The velocity profile corresponding to the shear stress profiles in Figure A.1 is shown in Figure A.2. A dimensionless constant k, was also computed ($k = 1.08$) to relate the turbulent energy obtained with the probe in the horizontal position to the turbulent energy with the probe in the vertical position i.e.

$$k = \frac{u'^2 + v'^2}{u'^2 + w'^2} \quad (\text{A.3})$$

A grid was laid out over a portion of the area expected to scour. The region directly in front of the structure was excluded due to the complexity of the flow direction resulting from the horseshoe vortices. The grid is shown in Figures A.3 and A.4. In Figure A.3, the x and y scales are equal. The y scale has been expanded 4.5 times in Figure A.4. This distorted scale is used to present both hydrodynamic and scour results.

A.2 Experimental Procedures

Prior to conducting the actual tests, the instrumentation had to be set up and calibrated. Preliminary tests were also conducted in the flume to determine the optimum location to place the model. It was determined that the flow over the V-notch weir had a jetting effect such that the velocity across the tank was not uniform as the flow approached the test area, so a fine mesh screen was constructed and placed directly downstream of the

weir. This significantly decreased the jetting effect. A floating wooden lattice was also placed at the entrance of the flume to dampen the waves generated by the weir and a plastic wire mesh wave absorber was placed at the downstream tailgate to minimize wave reflection. The anemometer measurements were sensitive to water temperature variations so a temperature probe was placed near the anemometer probe as shown in Figure A.5. The calibration curve for the temperature probe is shown in Figure A.6. The hydrodynamic tests were conducted at water temperatures ranging from 25 to 29 °C.

The mean flow direction at each grid point had to be determined for each structure configuration. The anemometer was then directed in the mean direction to minimize the probe skew angle. Prior to conducting the hydrodynamic tests, the flow was started and a vane was used to establish the mean flow direction at each grid point.

The hydrodynamic tests were conducted at night (starting around midnight) when the air temperature was on the decline, to minimize the change in water temperature during the test. Even with the decline in air temperature, the water temperature increased at a rate of approximately 0.3 °C/hour due to the pump and recirculation. Prior to starting the experiment, the anemometer probe was towed at several velocities through the still water in the flume to obtain a calibration curve for the velocity. A typical velocity versus probe output voltage curve for the X sensor probe is shown in Figure A.7. After calibration, the pump was started and the flow allowed to stabilize for approximately 45 minutes prior to starting the flow measurements.

The probe was first moved in front and away from the influence of the structure and the velocity measured at depths ranging from 0.12 to 7.38 inches above the bottom. This was used to obtain the undisturbed velocity profile (Figure A.2). The carriage was then moved along the structure and measurements were taken at the specified grid points. The measurements were made at all grid points in one column prior to moving to the next column, starting with points in front of the structure. The grid points are in rows and columns with the rows having constant x values and the columns having constant y values. Because the temperature in the flume increased at a rate of approximately 0.3 °C/hour, the velocity measurements in front of the structure were used to determine the variations in the flow measurements due to changes in the velocity calibration. After completing the measurements at the grid points, the velocities directly behind the structure were measured.

In order to compensate for the change in water temperature during the course of the test, curves of the mean velocity and turbulent energy/unit mass in front of the structure versus time were constructed as shown in Figures A.8 and A.9. Since the flow velocity did not vary significantly across the tank, the mean velocity and turbulent energy/unit mass curves could be applied to the entire test area. This allowed the mean velocity and turbulent energy at each grid point to be non-dimensionalized by the mean velocity and turbulent energy in front of the structure.

A.3 Data Acquisition

A Metrabyte 16F computer board and ACQWIRE data acquisition software were used to digitize and record the analog signals from the X sensor and temperature probes. Scales were placed along and across the flume and the readings were recorded manually. The vertical position traversing mechanism was controlled by a lap top computer. In addition, a cut off switch attached to the probe support was used for the lowest (0.12 in) position (see Figure A.5). This switch was used to insure that the bottom velocity measurements were made at the same fixed distance above the bed at all locations.

A.3.1 X Sensor Probe

The probe has 2 perpendicular wires in parallel planes that sense the normal components of the flow in the plane of the wires. The output voltages that are proportional to the velocity components are processed by the ACQWIRE data acquisition software to obtain U (velocity along the tank) and V (velocity across the tank) based on a velocity calibration curve such as that shown in Figure A.7. Flow and temperature measurements were sampled at a rate of 50 hertz. Due to the change in the average temperature of the water in the flume, the X sensor probe had to be calibrated prior to each set of tests. The two velocity components, U and V can be calculated from the sum and difference of the hot film anemometer output voltages, Volt₁ and Volt₂, as follows:

$$U = \frac{1}{\sqrt{2}} (Volt_1 + Volt_2) \quad (A.4)$$

and

$$V = \frac{1}{\sqrt{2}} (Volt_1 - Volt_2) . \quad (A.5)$$

A typical unfiltered signal is shown in Figure A.10 and the same signal after filtering is shown in Figure A.11. Plotted in Figures A.12 and A.13 are the power density spectra of U and V for the time series shown in Figures A.10 and A.11. The power density spectra of the unfiltered U signal shows a large spike of energy at 10 hertz. This was caused by vortex shedding from the probe holder. Although the noise at 10 hertz for the V signal was not as large as for the U signal, a bandstop, fourth-order Butterworth filter at 10 hertz was applied to both signals.

A.3.2 Temperature Probe

The temperature probe (see Table A.3) was attached downstream of the X sensor probe to measure the instantaneous temperature fluctuations. Ideally, the temperature probe would be located at the X sensor probe but since the temperature probe was rather large (approximately 0.156 inches in diameter and 3.33 inches long), it was placed far enough

downstream so as not to disturb the flow at the X sensor probe. It was located approximately one foot downstream of the X sensor probe. These water temperature measurements were used in the ACQWIRE data acquisition software to apply a correction to the velocity data after measurement.

A.3.3 Temperature Correction

The ACQWIRE data acquisition software applies a correction to the measured raw voltages and is valid for small temperature changes such that the physical parameters of the fluid can still be assumed to be constant. This temperature adjustment is shown below:

$$V_{bo} = V_b \left(1 - \frac{\alpha \delta T}{a} \right)^{-0.5} \quad (\text{A.6})$$

where

V_{bo}	=	bridge voltage at ambient fluid temperature T_o ,
V_b	=	bridge voltage at temperature T ,
α	=	temperature coefficient of resistance (property of probe provided by manufacturer),
a	=	overheat ratio $(R_h - R_{co})/R_{co}$,
R_{co}	=	cold sensor resistance at T_o ,
R_h	=	hot sensor resistance,
T_o	=	calibration fluid temperature (i.e. ambient temperature) and
T	=	fluid temperature during measurement.

A.3.4 Vortex Shedding from Probe Holder

Alternate vortex shedding in the wake region of the flow around the X sensor probe support induced a response that influenced the flow measurements. The traversing mechanism and probe support were more rigid in the x direction than the y direction thus the response was greater in the y direction. The response is evident in the power density spectrum of U shown in Figure A.12. Note the spike in the spectrum at 10 hertz. If the Strouhal Number, S_t , is assumed to be 0.2 for smooth cylinders, the vortex shedding frequency, f_v , can be computed as follows:

$$f_v = \frac{S_t U}{d} \quad (\text{A.7})$$

If $U = 0.98$ ft/sec and
 $d = 0.02$ ft,
 then $f_v = 10$ hertz.

This made it necessary to filter the velocity measurements with a bandstop, fourth-order Butterworth filter at 10 hertz. A pre and post filtered time series and energy density spectrum are shown in Figures A.10 to A.13.

A.4 Flow Visualization Measurements

Several flow measurements were taken prior to the hydrodynamic study to determine the different parameters that may affect the results. It was necessary to determine the limitations of the X sensor probe and the characteristics of the flume. The results of these tests are presented and discussed in this section.

1. Variation of mean velocity versus number of data points sampled

The sampling duration had to be longer than the lowest frequency component of the flow. The sampling rate used was 50 hertz and a plot of mean velocity versus number of data points sampled (i.e. the duration of the record) is shown in Figure A.14. Variations in the mean velocity appear to cease at about 8192 samples so this duration record was selected for all tests.

2. Variation of mean velocity parallel and normal to the 70° pile cap (top position) structure

The grid points chosen for the flow measurements were based on the results of mean velocity measurements parallel and normal to the structure. The X sensor probe was placed as close as possible to the 70° pile cap (top position) structure and measurements taken at $z = 0.12$ in (3 mm) between pile 1 and 2, pile 2 and 3, pile 3 and 4 and so forth. Figure A.15 shows the variation of the ratio of the mean velocity next to the structure and the mean velocity in front of and away from the influence of the structure, as the probe was moved along the structure. The results show that by taking measurements between every other pile (e.g. pile 1 and 2, pile 3 and 4 etc.), the velocity field along the structure can be mapped. Figure A.16 shows the variation of the mean velocity across the tank as the probe was moved away from the structure. The probe was positioned at $x = 0.335$ ft and $z = 0.12$ in (3 mm) and the y position of the probe was varied. The coordinates of the grid points used during the hydrodynamic experiments are listed in Table D.1.

3. Variation of mean velocity at the same location

The probe was positioned in front of and away from the influence of the structure and three consecutive mean velocity measurements were taken at the same location ($x = -4.92$ ft; $y = 0.269$ ft and $z = 0.12$ in). Table A.4 shows that the mean velocity can fluctuate up to 2.5% even without the influence of the structure.

4. Variation of mean velocity across the tank

The probe was once again moved in front of the structure ($x = -4.92$ ft and $z = 0.420$ ft) and flow measurements were taken as the probe was moved away from the center of the tank. Table A.5 shows that the flow was fully developed across the tank in the test area.

5. X sensor probe cosine response

Preliminary tests using a flow vane and streamers were conducted to determine the changes in horizontal flow direction as a function of time near the structure. This showed that the flow direction varied up to $\pm 30^\circ$ from the mean. To determine if the X sensor probe (filaments in the vertical direction) could resolve the horizontal flow direction changes, the probe was placed in front of and away from the influence of the structure and the mean velocity measured with the probe at various angles to the flow. Column 2 in Table A.6 shows that the velocity component in the x direction, U, measured by the probe increased as the probe was rotated away from the mean flow direction. The correct cosine response of the X sensor probe is listed in column 3. Turning the probe on its side (filaments in the horizontal direction) improved the ability of the probe to resolve changes in the horizontal flow direction. With the probe in the horizontal position, the U and V velocity components can be measured.

Table A.7 lists the measured resultant velocity $\sqrt{U^2 + V^2}$. This value should, of course, remain constant as the probe is rotated. The results show that the measured velocity when the probe is at 15° to the flow is 1.3% less than the measured velocity when the probe is at 0° . This is within the range of fluctuations of the mean velocity at the same location as shown in Table A.4

Table A.1 Constant temperature anemometer technical data.

Dantec 56C01 CTA Unit - Serial No. 905B0121 688 Dantec 56C17 CTA Bridge - Serial No. 905C0171 1447 and 1435	
Top Resistance	20 Ω
Bridge Ratio	1 : 20
Sensor Resistance Range	3 - 30 Ω
Resistance Measuring Sensitivity	0.1 Ω/V
Probe Cable Length	16.4 ft
Amplifier Shape	Film
Temperature Range	+5 to +40 $^\circ C$

Table A.2 X sensor probe technical data.

Dantec R61 Probe - Serial No. 9055R0611		
	Wire 1	Wire 2
Sensor Resistance at 20 °C	6.96 Ω	6.10 Ω
Probe Lead Resistance	0.60 Ω	0.60 Ω
Coefficient of Resistance	0.39 %/°C	0.40 %/°C
Overheat Ratio	0.045	0.045
Cable Resistance	0.14 Ω	0.04 Ω

Table A.3 Temperature probe technical data.

Analog Devices AC2626-J4 Temperature Probe Serial No. 2461 9161	
Accuracy	0.125 °C max @ 25 °C
Temperature Range	-55 °C to +140 °C
Voltage Supply	+4 V to +30 V
Output	1 μA/K
Length	4.0 in
Diameter	0.187 in

Table A.4 Variation of mean velocity with time at the same location
($x = -4.92$ ft; $y = 0.269$ ft and $z = 0.12$ in).

Test Number	Mean Velocity (ft/sec)
1	0.781
2	0.764
3	0.761

Table A.5 Variation of mean velocity across the tank in front of and away
from the influence of the structure ($x = -4.92$ ft and
 $z = 0.41$ ft).

Test Number	Mean Velocity (ft/sec)	y (ft)
1	1.191	-0.344
2	1.220	0.312
3	1.217	1.04
4	1.198	1.95

Table A.6 X sensor probe cosine response - probe vertical
(x = -4.92 ft; y = 1.46 ft and z = 0.12 in).

Flow Skew Angle	U _{measured} (ft/sec)	U _{correct} (ft/sec)
0	0.754	0.754
7.5	0.760	0.748
15	0.766	0.728

Table A.7 X sensor probe cosine response - probe horizontal
(x = -4.92 ft; y = 0.692 ft and z = 0.12 in).

Angle	Vel _{measured} (ft/sec)	Vel _{correct} (ft/sec)
0	0.690	0.690
15	0.680	0.690
30	0.640	0.690

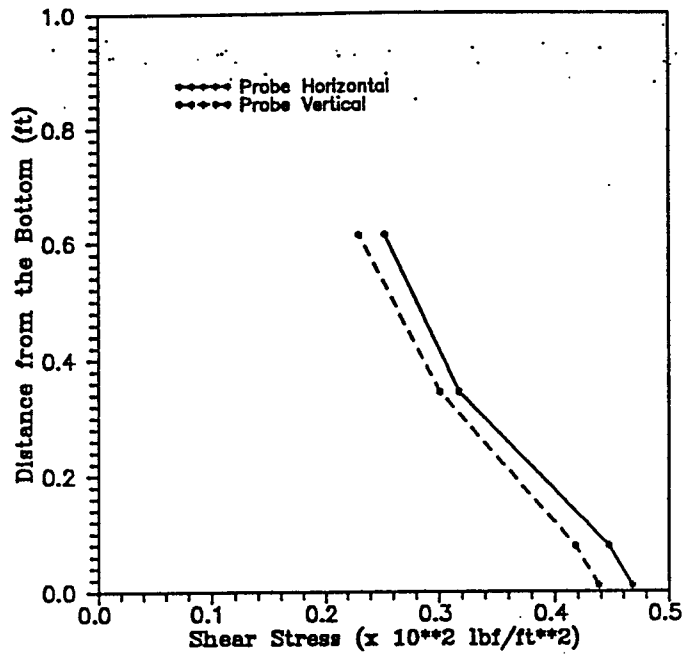


Figure A.1 Shear stress profiles in front of and away from the influence of the structure at $x = -4.92$ ft and $y = 0.364$ ft.

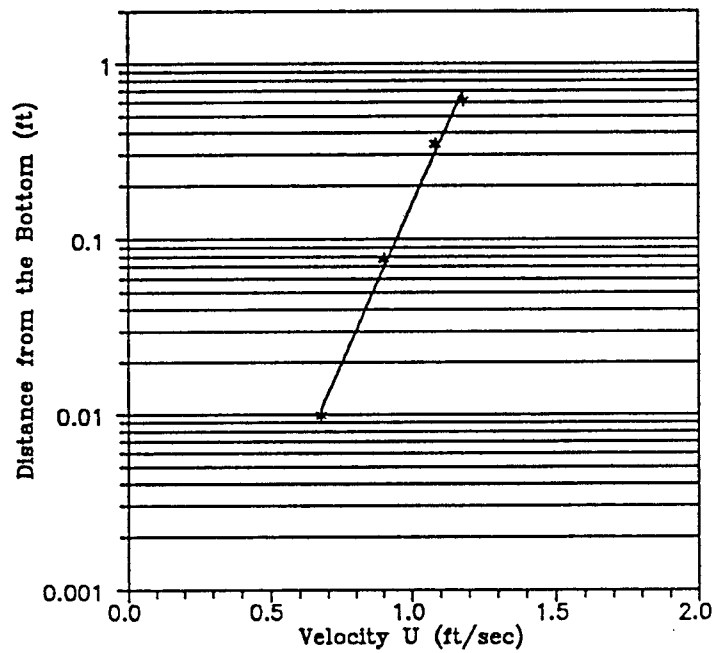


Figure A.2 Velocity profile corresponding to shear stress profiles in Figure A.1.

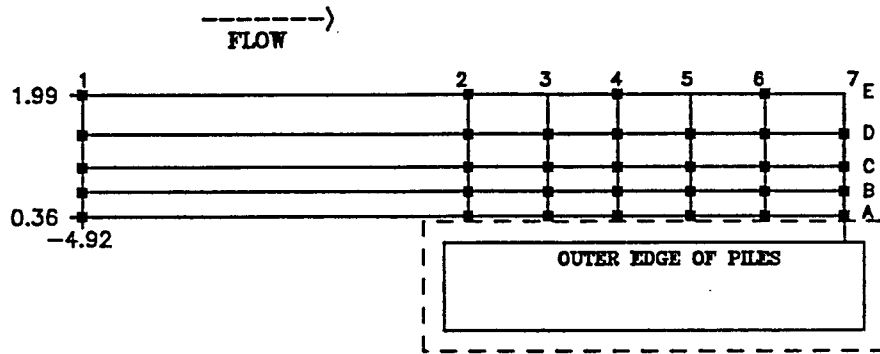


Figure A.3 Grid points for hydrodynamic study (1:1 scale).

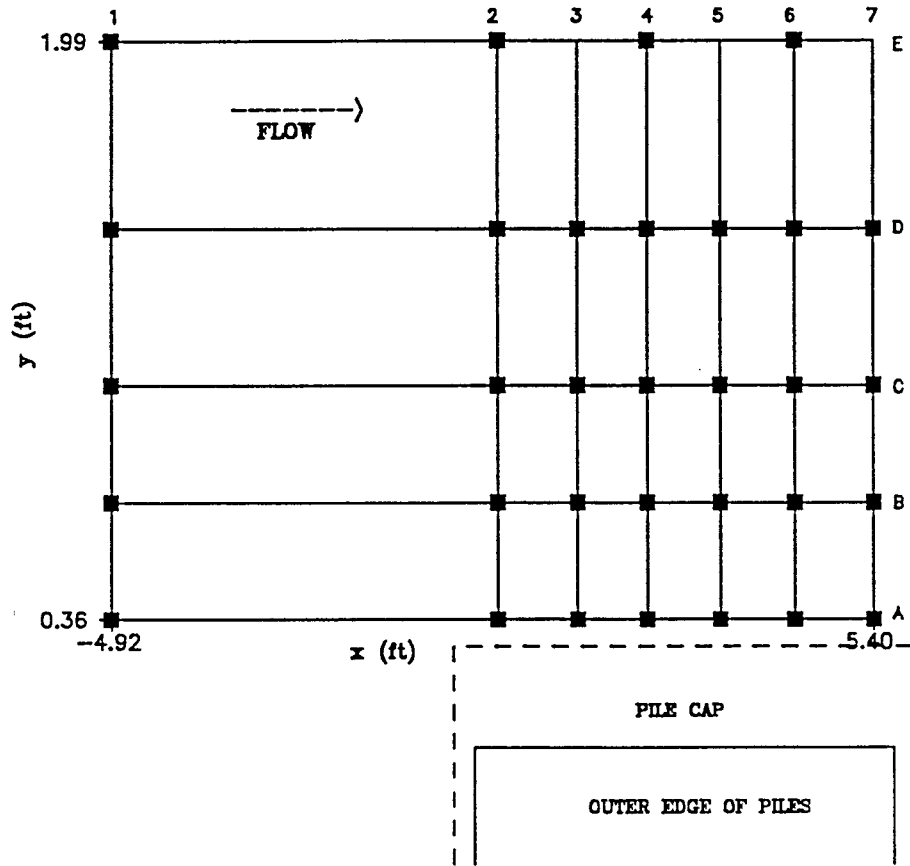


Figure A.4 Grid points for hydrodynamic study (distorted 1:4.5 scale).

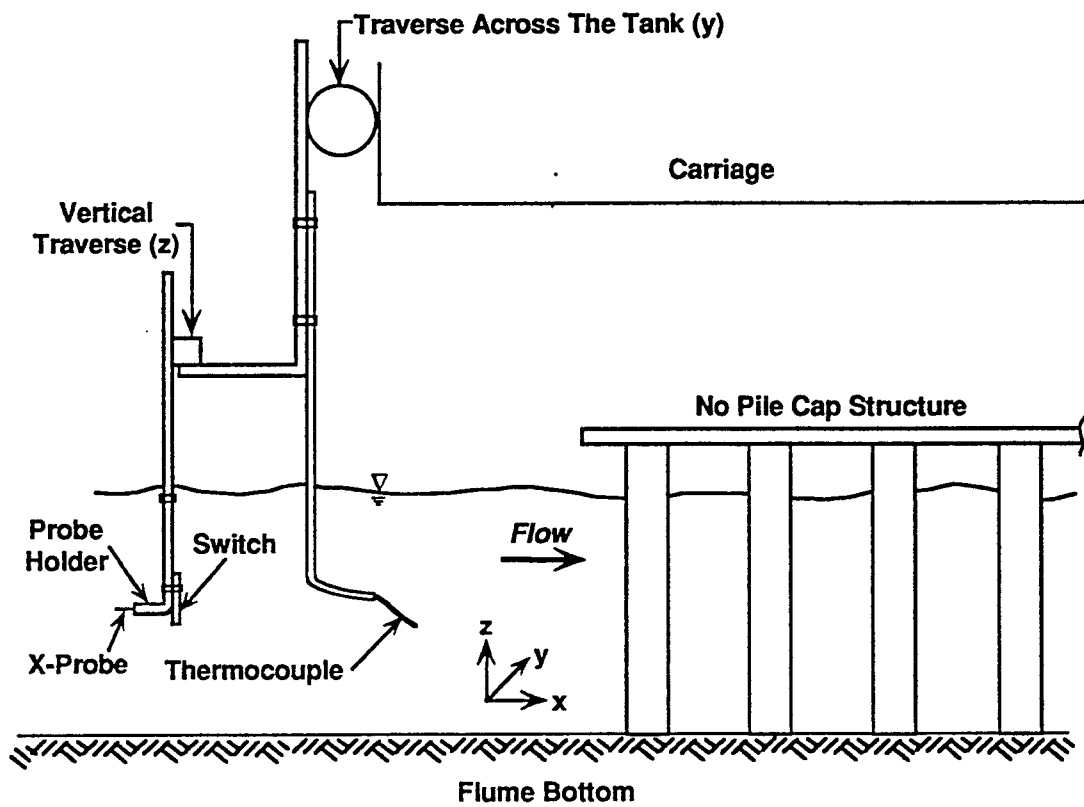


Figure A.5 Overall set-up of experimental apparatus and instrumentation for hydrodynamic study.

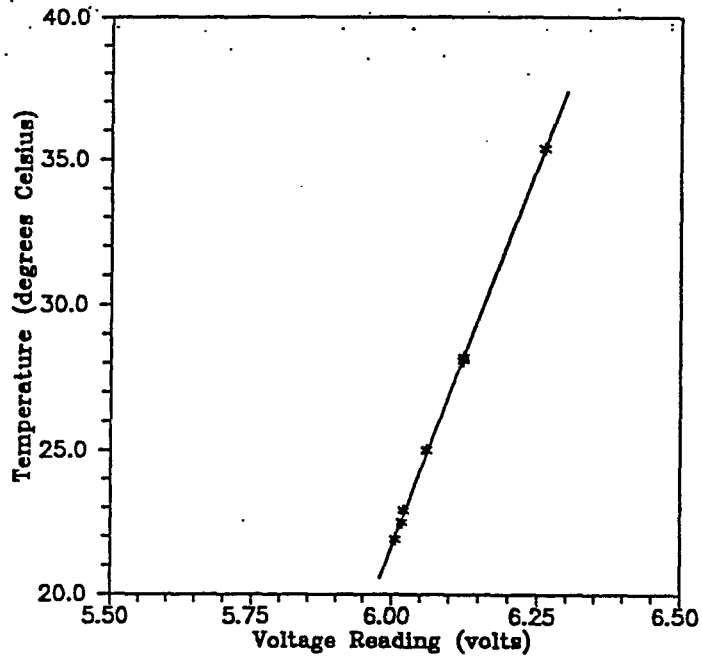


Figure A.6 Calibration curve for the temperature probe.

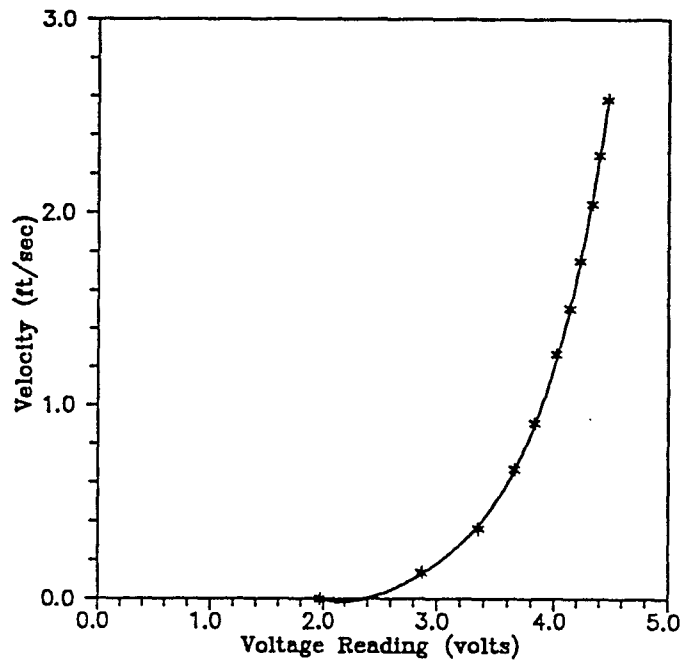


Figure A.7 Calibration curve for the x sensor probe.

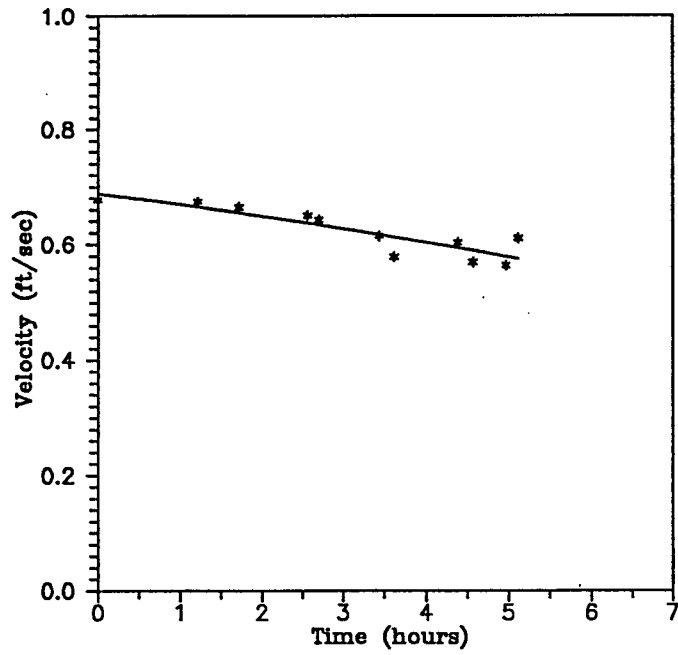


Figure A.8 Mean velocity in front of structure vs. time at $x = -4.92$ ft and $z = 0.12$ in (test H-1).

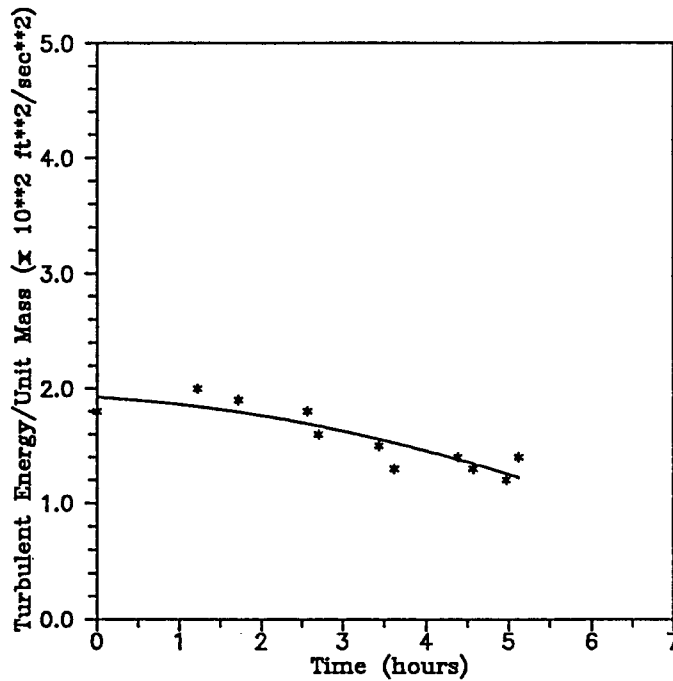


Figure A.9 Turbulent energy/unit mass in front of structure vs. time at $x = -4.92$ ft and $z = 0.12$ in (test H-1).

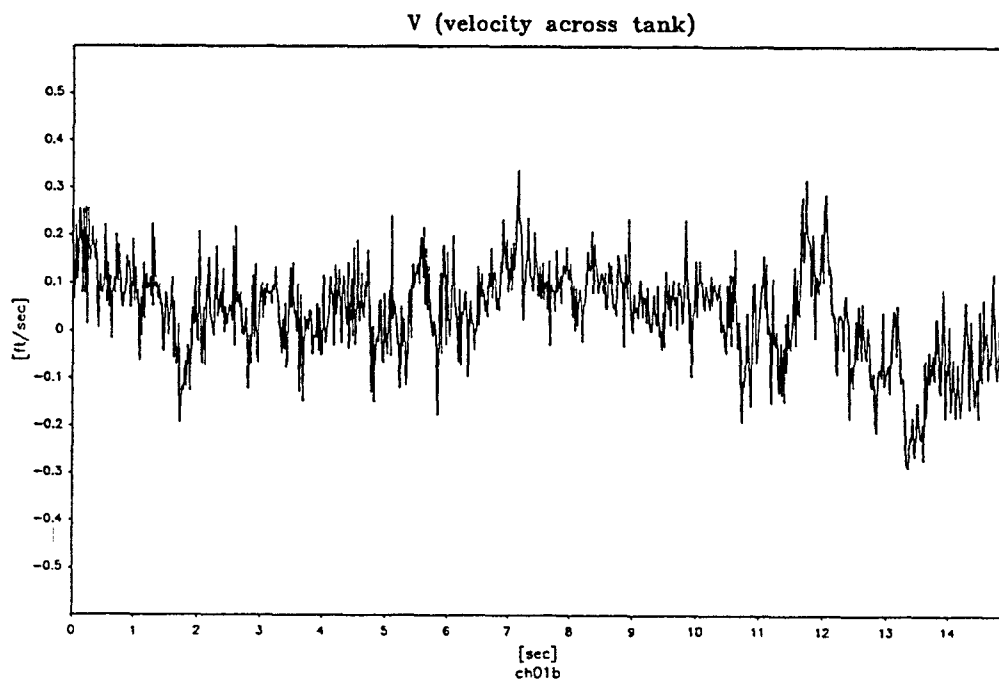
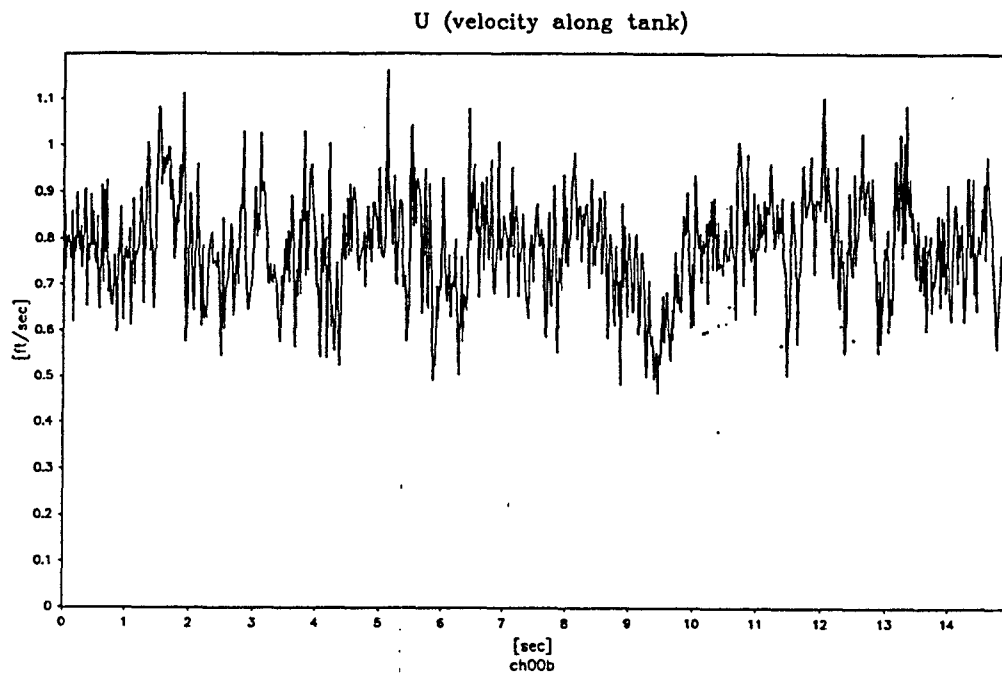


Figure A.10 Unfiltered U and V velocity components for test H-1 at grid point B2.

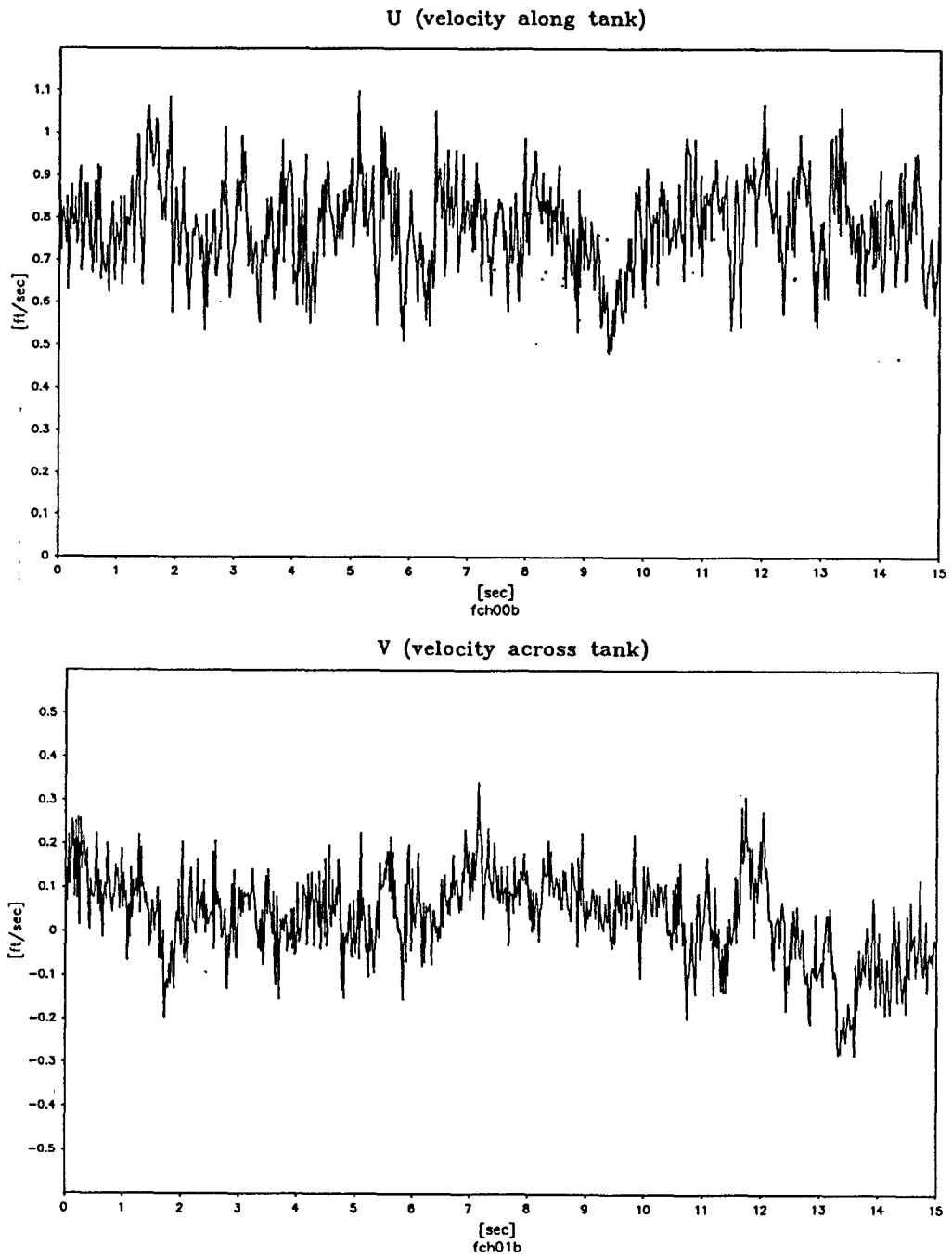
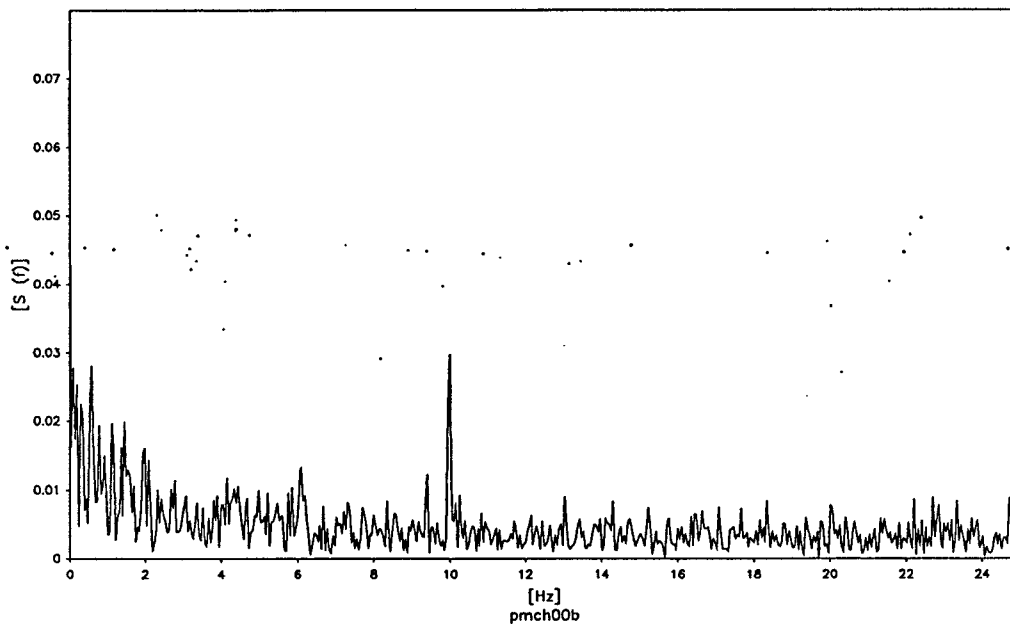


Figure A.11 Filtered U and V velocity components for test H-1 at grid point B2.

Power Density Spectrum of Unfiltered U (velocity along tank)



Power Density Spectrum of Filtered U (velocity along tank)

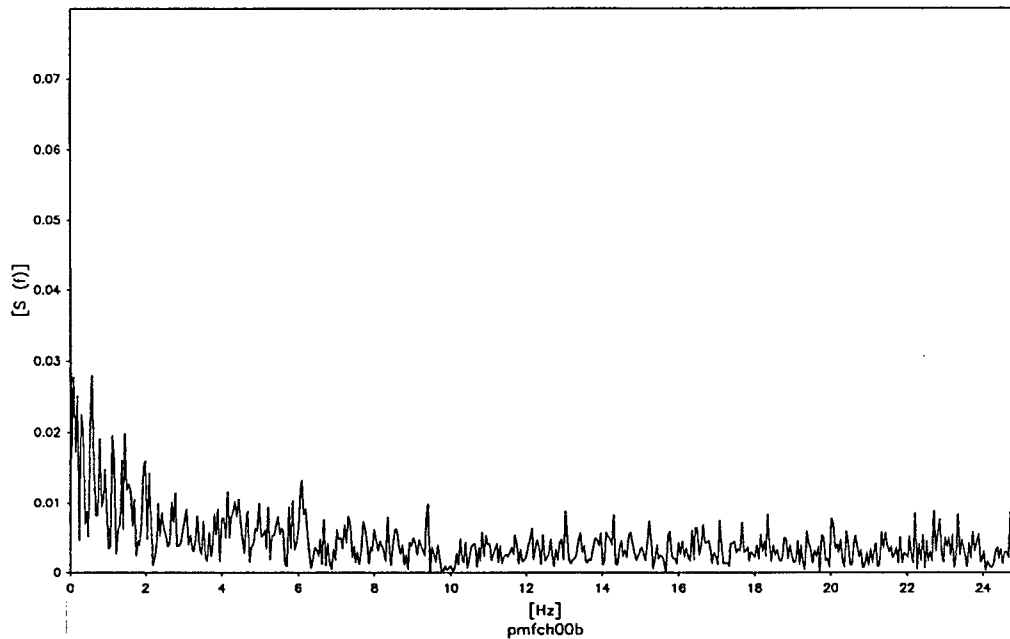
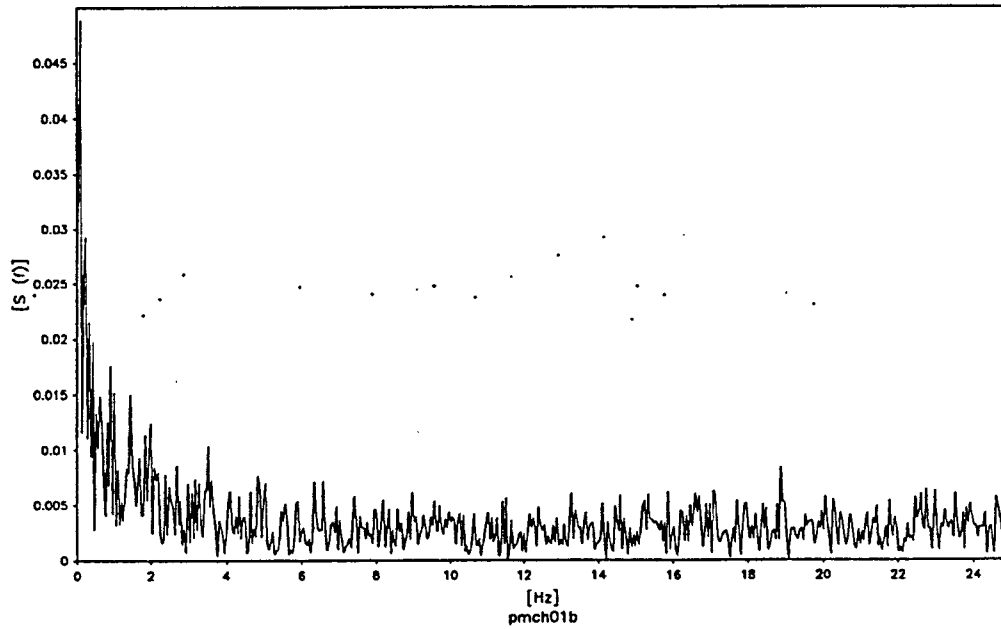


Figure A.12 Power density spectra of U velocity components in Figures A.10 and A.11.

Power Density Spectrum of Unfiltered V (velocity across tank)



Power Density Spectrum of Filtered V (velocity across tank)

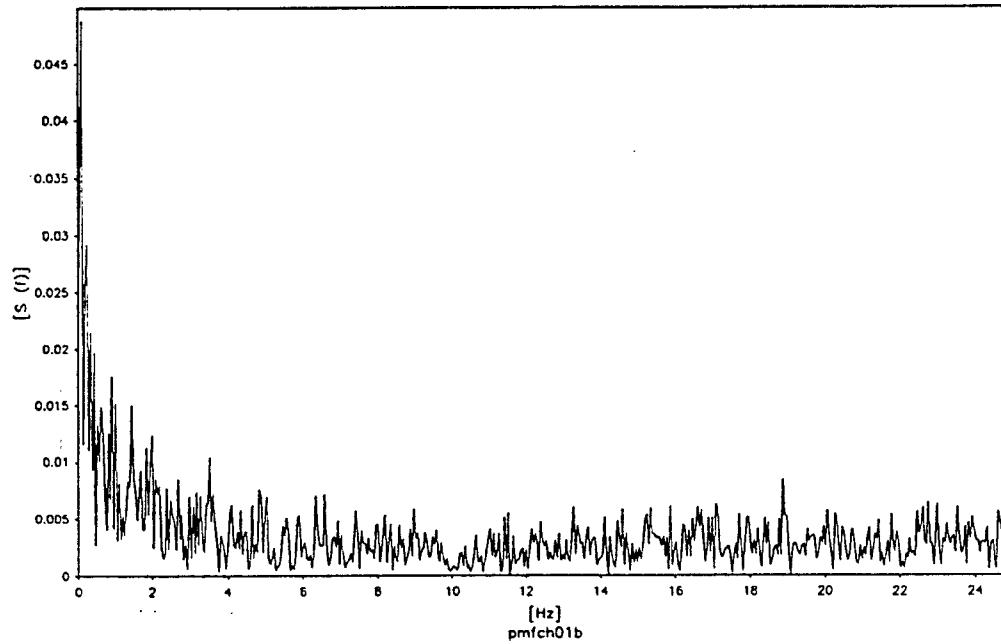


Figure A.13 Power density spectra of V velocity components in Figures A.10 and A.11.

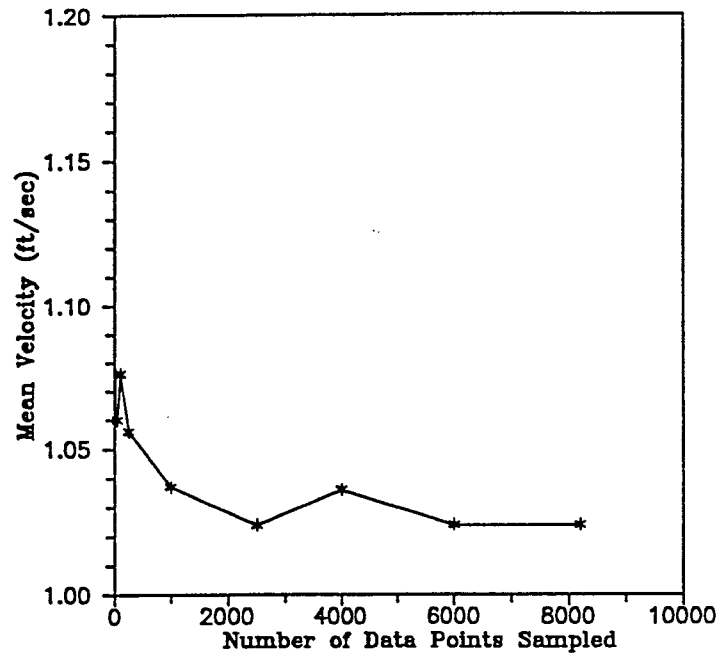


Figure A.14 Mean velocity vs number of data points sampled ($x = 0.335$ ft; $y = 0.364$ ft and $z = 0.12$ in).

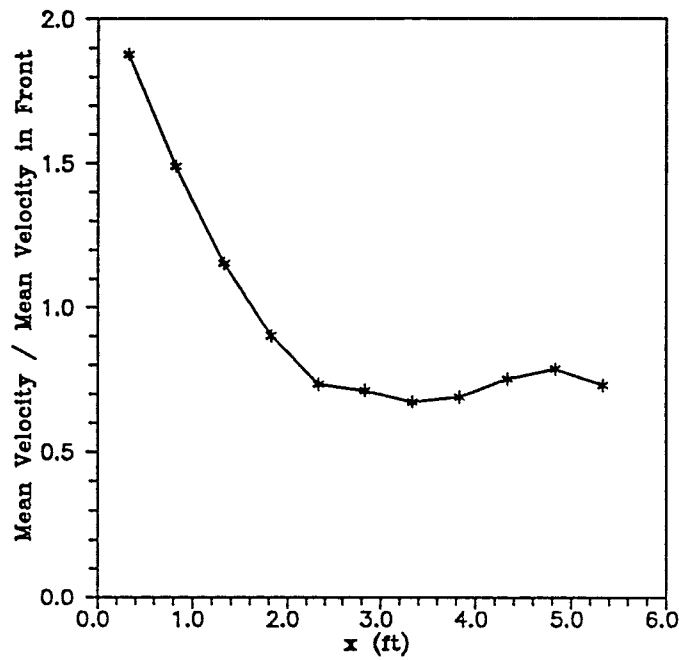


Figure A.15 Variation of mean velocity parallel to the 70° pile cap (top position) structure at $y = 0.364$ ft and $z = 0.12$ in.

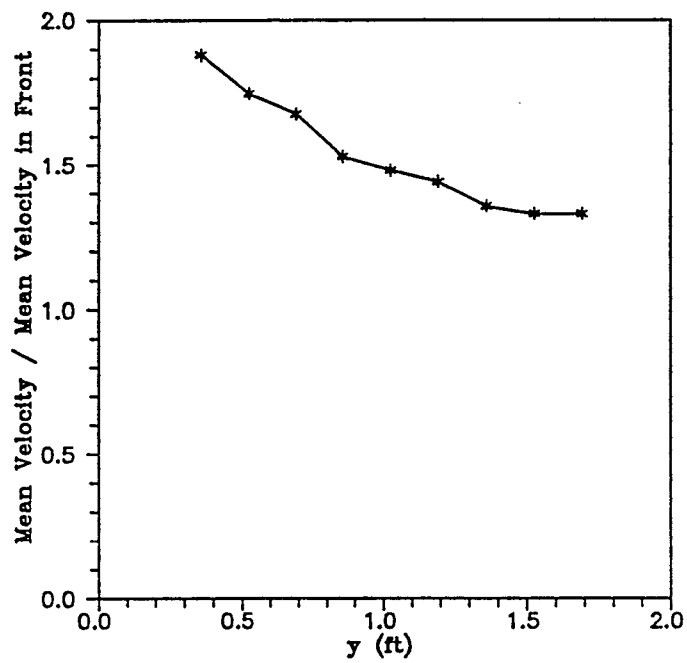


Figure A.16 Variation of mean velocity normal to the 70° pile cap (top position) structure at $x = 0.335$ ft and $z = 0.12$ in.

APPENDIX B

SCOUR STUDY

SCOUR STUDY

B.1 Background

Sediment scour experiments were performed in the same flume and with the same model piers as the hydrodynamic study. The objectives of the scour study were: 1) to provide scour data for calibrating and testing the scour prediction relationship developed as part of the hydrodynamic study and 2) to provide laboratory scour data for multiple pile structures with and without pile caps. Another important aspect of this study was the measurement of the rates of scour.

The metal plates covering the recess in the flume were removed and the multiple pile structure was centered in the test area. Sand was then placed around the structure (see Figure B.1). Three different sediment sizes were used in the flume. The largest quantity of sand (Category 1) was placed in the regions of the test area where no scour was anticipated. This category had sediment sizes ranging from 0.2 to 0.8 mm (see Figure B.2). Category 2 consisted of sand that was used to anchor the sand in the first category and had a range of sediment sizes from 0.84 to 2.00 mm (see Figure B.3). This minimized the amount of fine sand transported down the flume and through the pump. The third category of sand was placed in the region around the structure where scour was anticipated. This category had sediment sizes ranging from 0.42 to 0.84 mm and a median grain size, d_{50} , of 0.60 mm (see Figure B.4).

Instrumentation with the ability to make in situ scour measurements (i.e. measurements of the scour as it occurs) were developed. In the past, scour measurements have been very laborious and time consuming. Recent developments in underwater acoustics technology now allow techniques, formerly used only for bottom profiling at prototype depths to be used in the laboratory. The main component of the system used was the Simrad Mesotech 810 echo sounder (see Table B.1).

B.2 Instrumentation and Calibration

B.2.1 Depth Readings

The acoustic bed profiling system was developed, constructed and tested in the Coastal Engineering Laboratory at the University of Florida. An acoustic pulse sent by the echo sounder reflects off the bottom and the return pulse is sensed by the sounder. The time required for the signal to travel to and from the bottom is measured and the distance computed. Returns from particles in suspension also show up in the signal and must be dealt with as noise. A schematic drawing of the system is shown in Figure B.5. The bowl which sits just below the surface of the water when measurements are being made serves to minimize the disturbance to the flow (see Figure B.6).

To allow the echo sounder to send acoustic signals to the bottom, a small window was cut out of the bowl and a vinyl sheet glued over the slot. The acoustic reflection from the vinyl sheet was minimal. The level of water in the bowl was such that the end of the sounder head was always submerged. The echo sounder was mounted on a frame as shown in Figure B.5 and a motor was used to rotate the head and thus the acoustic beam toward and away from the structure. The entire depth measuring system was mounted on a carriage that traversed the width of the flume.

The echo sounder operates at 2.25 Mhz. The 2.25 Mhz operating frequency was chosen to give reasonable accuracies at short ranges, as well as to insure sufficient energy in the reflection from the bed. A 10 μ sec pulse is emitted at a 100 Hz rate. The returned pulse is an analog time/amplitude history of the water column. The travel time of the signal is proportional to the distance to a reflecting object. The amplitude of the pulse at any point in time is a measure of the number, size and density of reflecting particles in the water column.

The acoustic signal from the echo sounder was calibrated by positioning a flat metal plate at different elevations below the sounder and the output recorded. A calibration curve for the echo sounder is given in Figure B.7.

Noise in the acoustic data (Channel CH00) came from reflections from the pile cap and/or piles and suspended sediment. Since the main mechanism for sediment movement was bed load transport, the noise caused by suspended sediment was minimal. A plot of the raw echo sounder output is shown in Figure B.8. The output from the echo sounder was filtered using a lowpass, sixth-order Butterworth filter with a cutoff frequency of 3 hertz. A plot of the echo sounder output signal after filtering is shown in Figure B.9. Power spectra for the unfiltered and filtered signals are shown in Figure B.10.

B.2.2 Position Readings

The angle the echo sounder head makes with the vertical was measured using a ten turn precision potentiometer. A protractor mounted on the side of the unit was used in the calibration process. The head was rotated to various angles and the output voltage from the potentiometer recorded. Because of some play in the gears moving the sounder head, a lag between the actual angle and the angle measured was observed. To compensate for this, a lag was added or subtracted from the calibration curve depending on the direction the sounder head was swinging. A plot of the modified calibration curve used is shown in Figure B.11 along with the actual readings during the calibration process. The modified calibration curves are listed below:

for the swing from -7° to 0° ,

$$\Theta \text{ (degrees)} = 39.60 - 11.16 V, \quad (\text{B.2})$$

for the swing from 0° to 32°,

$$\Theta \text{ (degrees)} = 39.102 - 11.16 V, \quad (\text{B.3})$$

for the swing from 32° to 0°,

$$\Theta \text{ (degrees)} = 42.60 - 11.16 V, \quad (\text{B.4})$$

and for the swing from 0° to -7°,

$$\Theta \text{ (degrees)} = 43.10 - 11.16 V. \quad (\text{B.5})$$

A small wheel in a track attached to a potentiometer was used to measure the position across the flume and a similar arrangement was used to measure the position of the carriage along the flume. Scales placed along and across the flume were used to calibrate the position potentiometers. The start and ending points for each traverse was recorded in the log book. A data reduction program was then used to transform the output from the echo sounder signal and the position potentiometers to xyz coordinates.

B.3 Data Acquisition

A Data Translation DT2801 computer board and GLOBAL LAB data acquisition software were used to digitize and record the analog signals from the echo sounder output and the potentiometer readings at a sampling frequency of 40 hertz.

Channel CH01 recorded the output from the potentiometer measuring the position along the flume (x direction) while Channel CH03 was used for the position of the carriage across the flume (y direction). Both output signals were filtered using lowpass, sixth-order Butterworth filters with a cutoff frequency of 0.5 hertz. The noise in Channel CH03 was caused by sudden movements of the manually operated traverse across the flume. The carriage was moved along the flume with a variable speed motor at a slow speed (approximately 0.8 in/sec). The smooth motion along the flume minimized the noise in Channel CH01. Figure B.12 compares the power density spectra of Channel CH03 before and after filtering. As mentioned before, the start and end points of the x and y traverses were recorded in the log book.

The echo sounder angle signal was recorded on Channel CH02 and was filtered using a lowpass, second-order Butterworth filter with a cutoff frequency of 20 hertz. The sounder head was designed to swing from -9° to 35° but only data in the range from -7° to 32° was used because of reflection and attenuation of the signal at the ends of the swing.

B.4 Data Reduction

A data reduction program was written to convert sediment scour data obtained from the echo sounder and position potentiometers to bottom coordinates in rectangular coordinates (x,y and z). The raw data consisted of: 1) voltage proportional to the distance from the echo sounder head to the bottom, 2) voltage proportional to the position of the depth measuring system along the tank (x position), 3) voltage proportional to the angle of inclination of the sounder head (measured from a vertical line with the angle varying from -7° to 32°) and 4) voltage proportional to the position of the depth measuring system across the tank (y position).

Figure B.13 is a definition sketch of the measurements needed to convert the raw data to x-y coordinates. The equations used are:

$$\begin{aligned} z &= (R + R_o) \cos \Theta - z_o \text{ and} \\ d &= (R + R_o) \sin \Theta, \end{aligned}$$

where

$$\begin{aligned} R &= \text{distance from echo sounder face to bottom,} \\ d &= \text{radial distance from echo sounder to bottom measurement,} \\ z_o &= \text{vertical distance from echo sounder pivot to original bottom,} \\ R_o &= \text{distance from echo sounder pivot to its face and} \\ \Theta &= \text{angle of echo sounder with vertical axis,} \\ &\quad (-7^\circ \text{ to } +32^\circ). \end{aligned}$$

After the data reduction process, the data was gridded using the surface fit program, SURFER, which was used to interpolate and map the bottom. Figure B.14 shows the data points used to map out the bottom prior to the test while Figure B.15 is a plot of the data points after the test was completed. The number of data points used to map the bottom was approximately 9,000.

B.5 Test Procedures

Prior to each scour test, the sand was compacted with a tamper, smoothed and leveled. After the bottom was leveled, the flume was slowly filled with water to prevent scour during the fill process. Before starting the flow, the bottom was mapped with the echo sounder. This allowed the scour measurements to be compared with the original bottom. After the pump was started, minor flow adjustments had to be made during the first 30 minutes of the test to obtain the desired velocities. Mapping of the bottom began a few minutes after the pump was started and this continued throughout the duration of the test (~ 28 hours). The interval between the scans increased as the rate of scour decreased (from ~ 10 minutes at the start to ~ 90 minutes at the end). After the flow was stopped, the bottom was mapped once more. The water was then drained from the flume and test area and point gauge measurements of the bottom were made.

B.6 Time Rate of Scour

Since these experiments were conducted under clear water scour conditions, the scour hole development could be observed visually. As soon as the flow was started, sediment along the structure was put into motion. Due to the clear water scour conditions, there was very little sediment being transported into the region surrounding the front row of piles, thus the rate of erosion in this region is large. Further downstream in the structure, there was initially (and for some time) more sediment being transported into the region than was being scoured, thus accretion occurred. Accretion continued until the transport into the region fell below the scour rate. The sediment transport processes were more rapid at first but decreased with time making it very difficult to judge the "maturity" of the scour hole strictly by observation.

Plots of scour depths versus time at different locations along the structure are very informative (see Figures B.16 and B.17). From these figures, it is evident that the local scour depths at rows 1 and 2 were approaching equilibrium after 28 hours. On the other hand, a net scour at the piles in row 6 was just beginning 25 hours into the flow. Figures B.18 to B.20 compare the time rate of scour of piles 1, 2 and 6 for the no pile cap structure and the 70° pile cap (top position) structure.

Table B.1 Echo sounder technical data.

Simrad Mesotech 810 Serial No. 9866	
Transmitter	
Transmitter	4 selectable pulse lengths and 2 selectable power levels
Operating Frequency	2.25 MHz
Output Power	200 Watts max
Beamwidth	0.8 degrees
Receiver	
Maximum Range	8.53 ft
Repetition Rate	100 Hz
Assumed Sound Velocity	4838 ft/sec
Output Frequency	455 Hz
Miscellaneous	
Temperature	Operating: -10 to +40 °C
Dimensions	3.5 in square x 8 in long



Figure B.1 Test area of flume showing no pile cap structure and central region near structure.

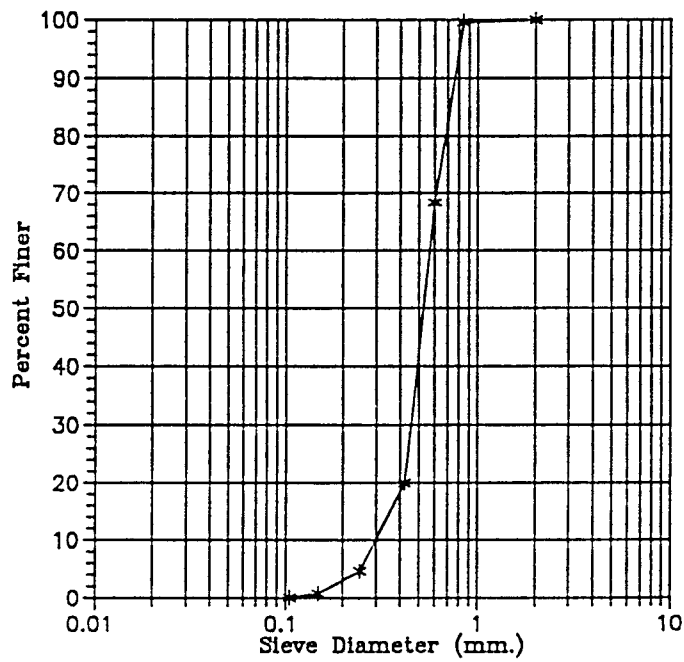


Figure B.2 Sediment size distribution for Category 1 sand (away from structure).

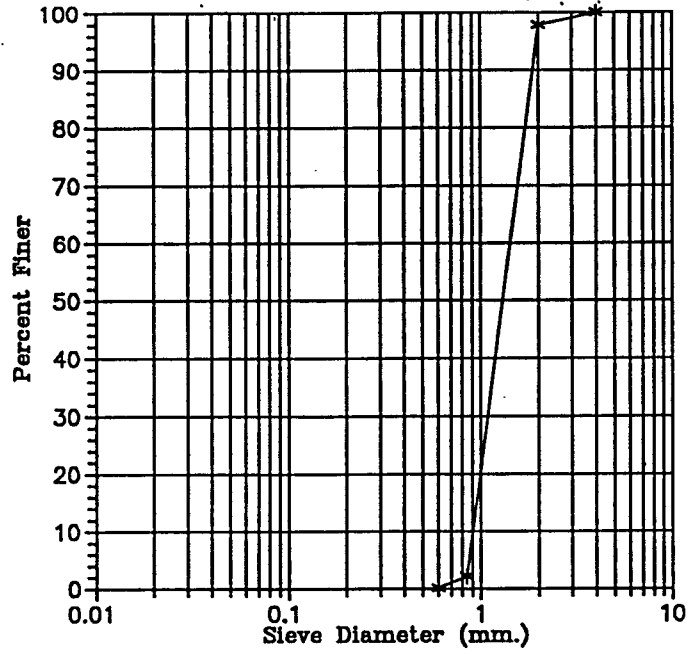


Figure B.3 Sediment size distribution for Category 2 sand (anchoring layer).

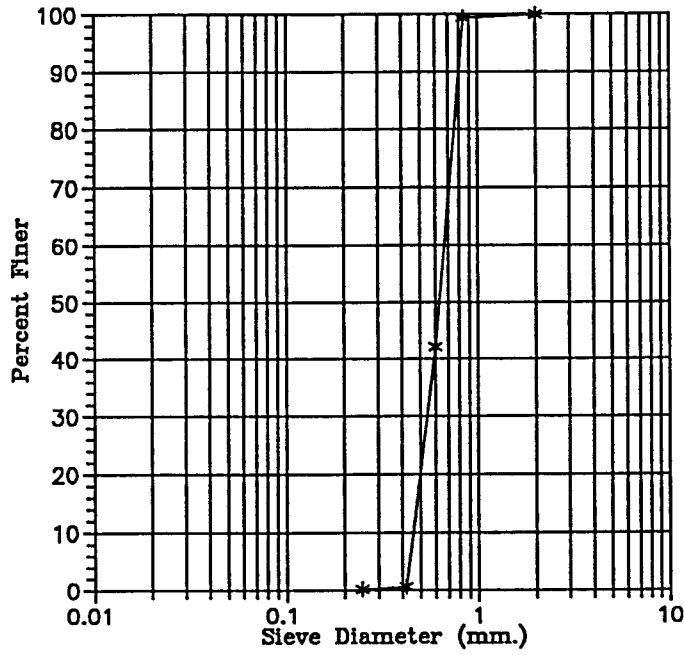


Figure B.4 Sediment size distribution for Category 3 sand (around structure).

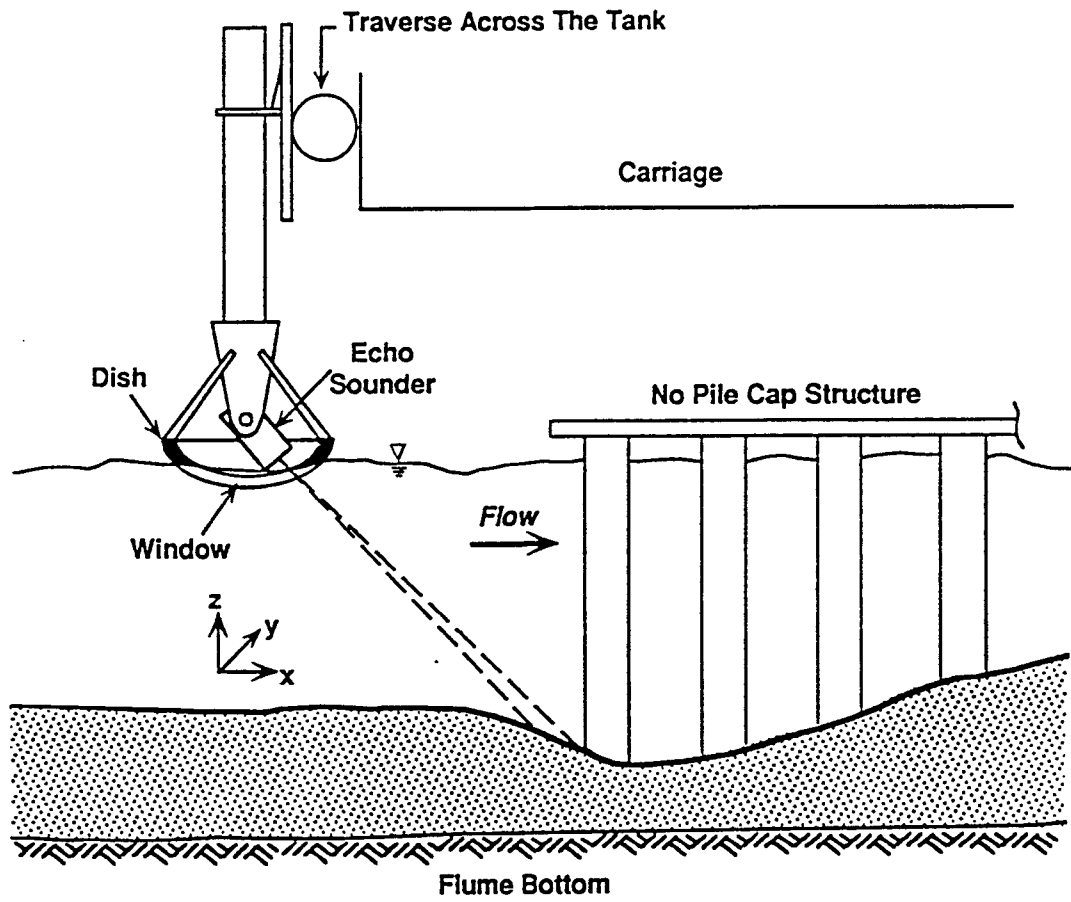


Figure B.5 Overall set-up of experimental apparatus and instrumentation for scour study.

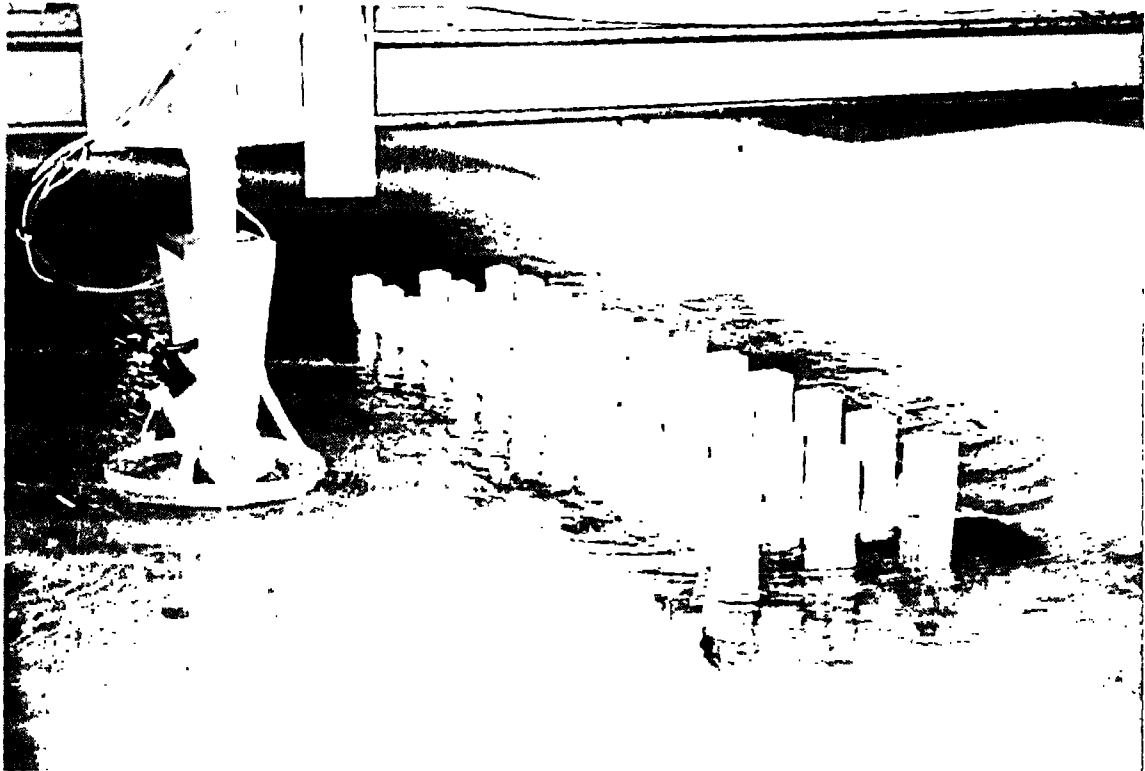


Figure B.6 Experimental set-up for scour study.

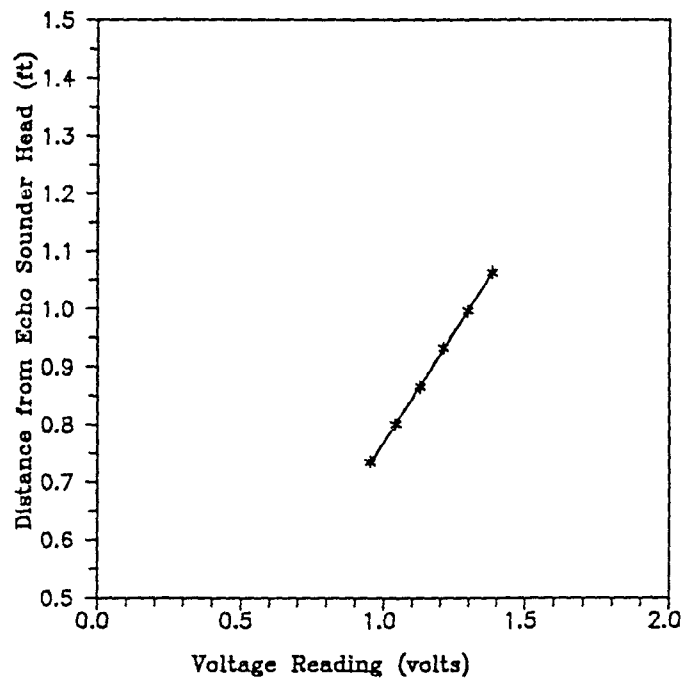


Figure B.7 Calibration curve for the echo sounder output signal.

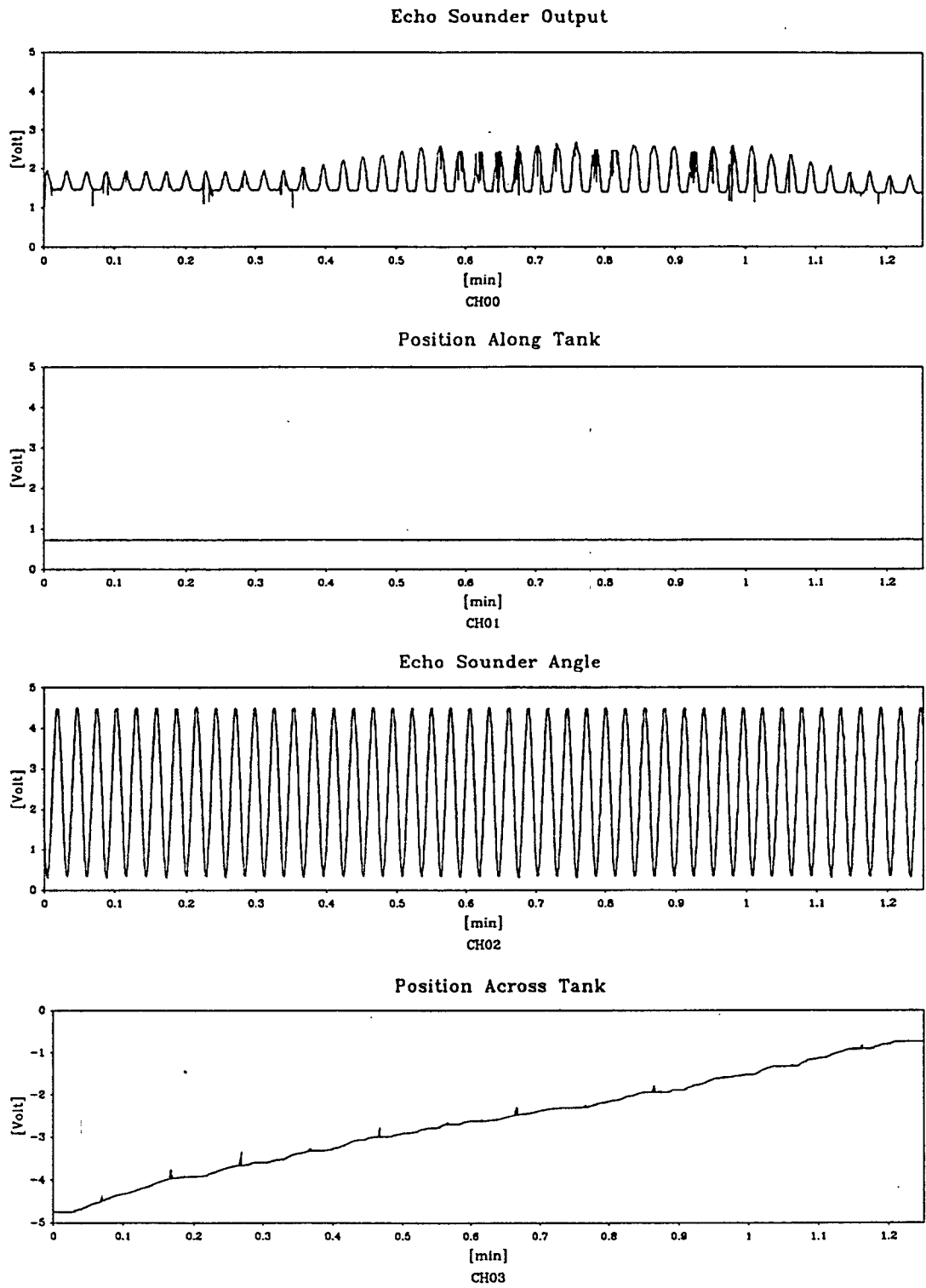


Figure B.8 Unfiltered output signals after completion of test S-1.

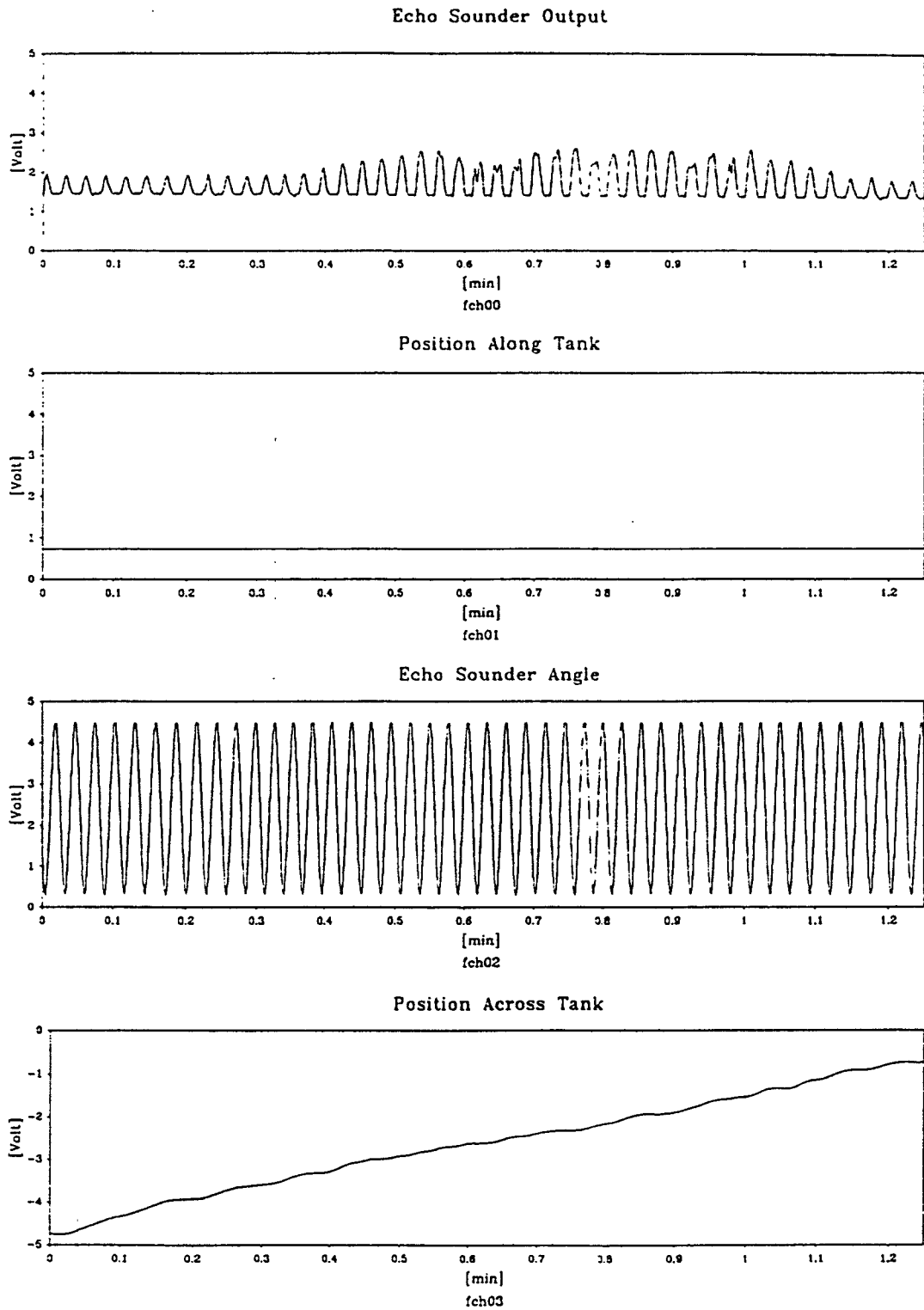
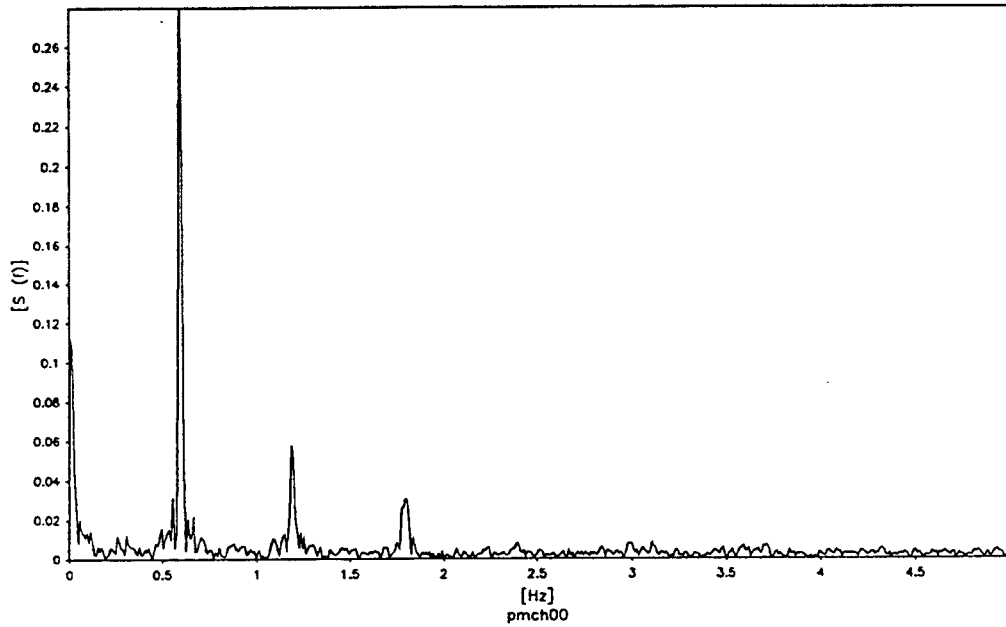


Figure B.9 Filtered output signals after completion of test S-1.

Power Density Spectrum of Unfiltered Sonar Output



Power Density Spectrum of Filtered Sonar Output

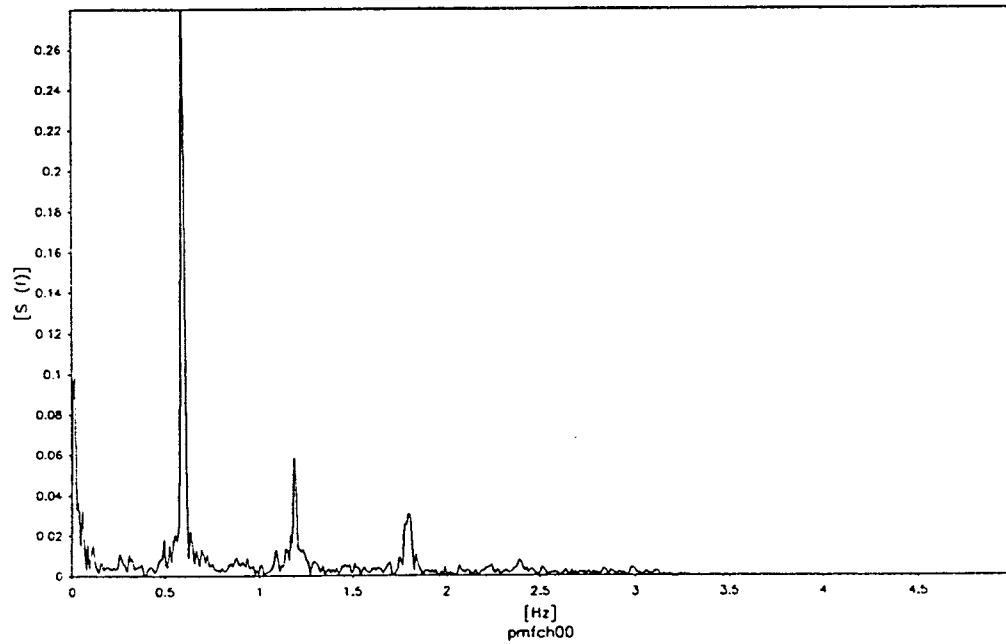


Figure B.10 Power density spectra of echo sounder output (Channel CH00) in Figures B.8 and B.9.

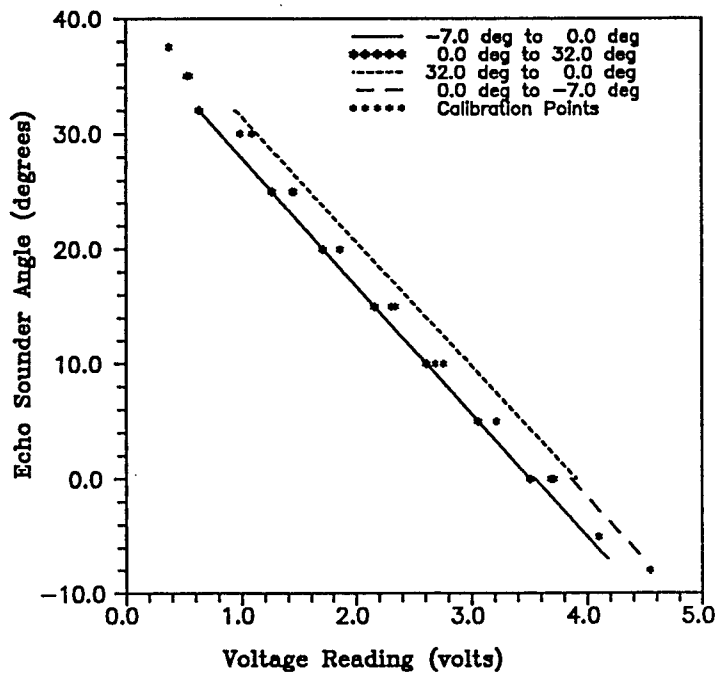
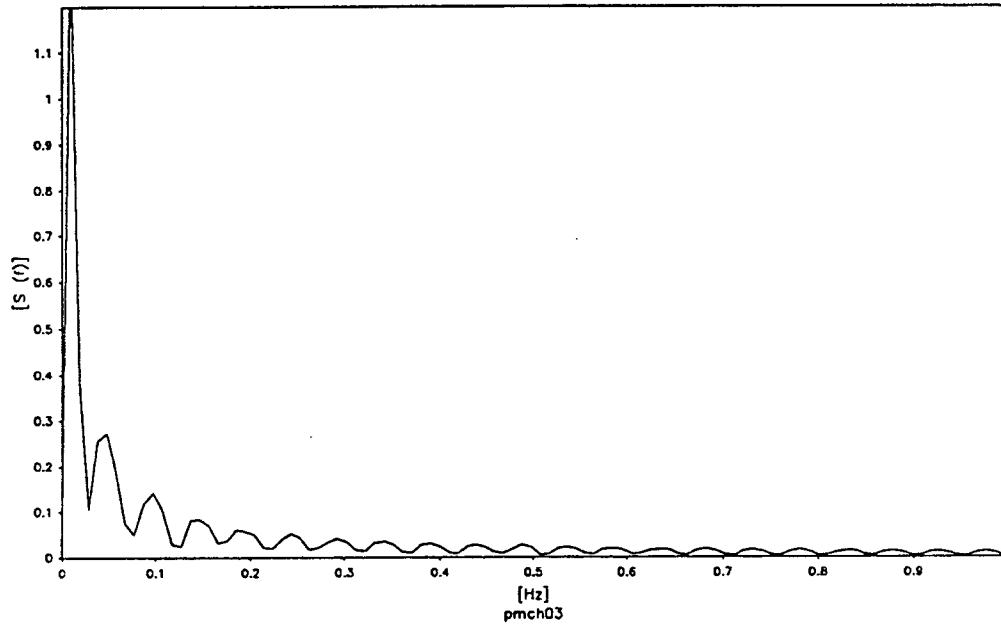


Figure B.11 Modified calibration curve for echo sounder angle.

Power Density Spectrum of Unfiltered Position Across Tank



Power Density Spectrum of Filtered Position Across Tank

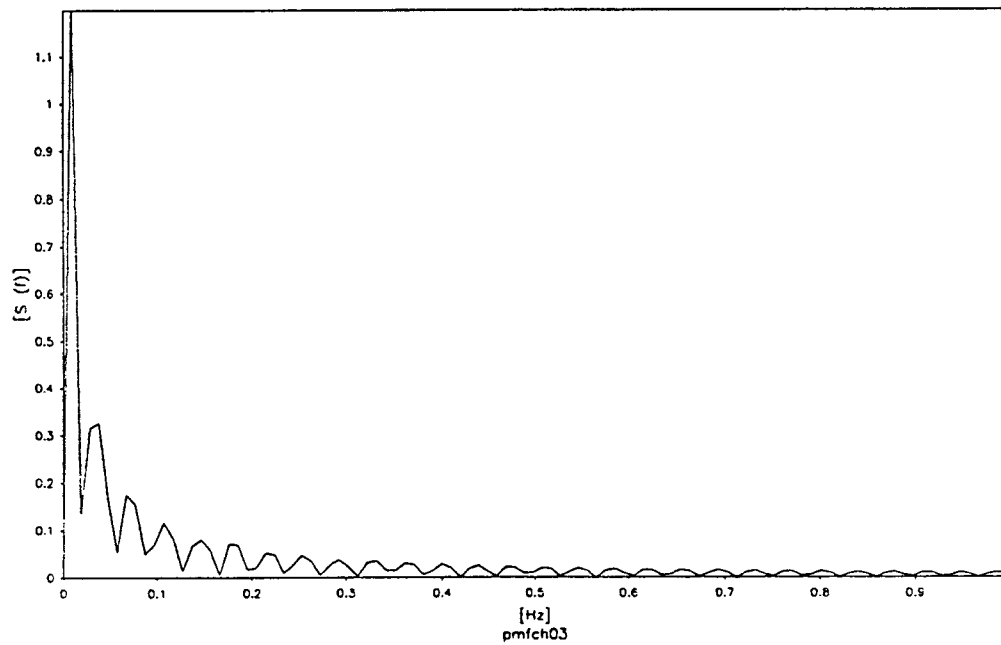
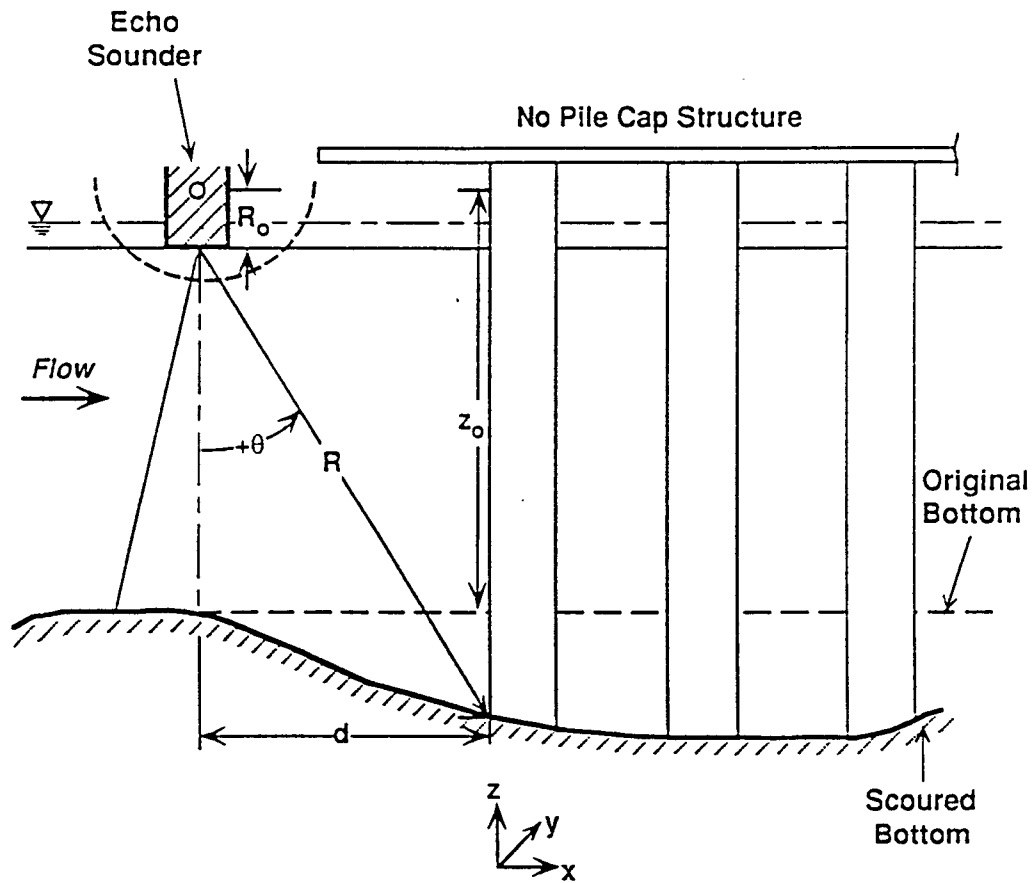


Figure B.12 Power density spectra of y position potentiometer (Channel CH03) in Figures B.8 and B.9.



The origin of the right hand coordinate system is located at the original bottom on the front outer corner of pile C1.
Positive x is in the direction of flow, *Positive z* is upward and *Positive y* is normal to the flow.

Figure B.13 Definition sketch showing measurements needed for conversion of raw data to x-y coordinates.

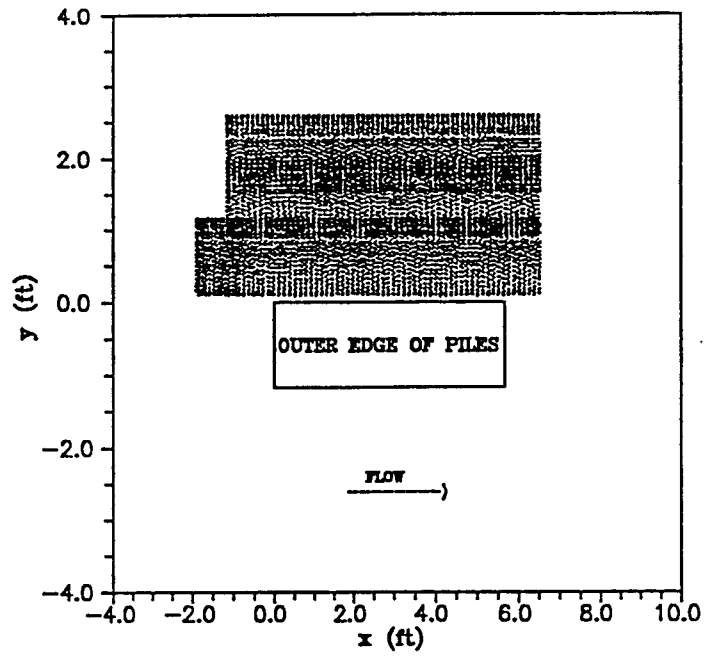


Figure B.14 Data points before start of scour test S-1 (No pile cap structure).

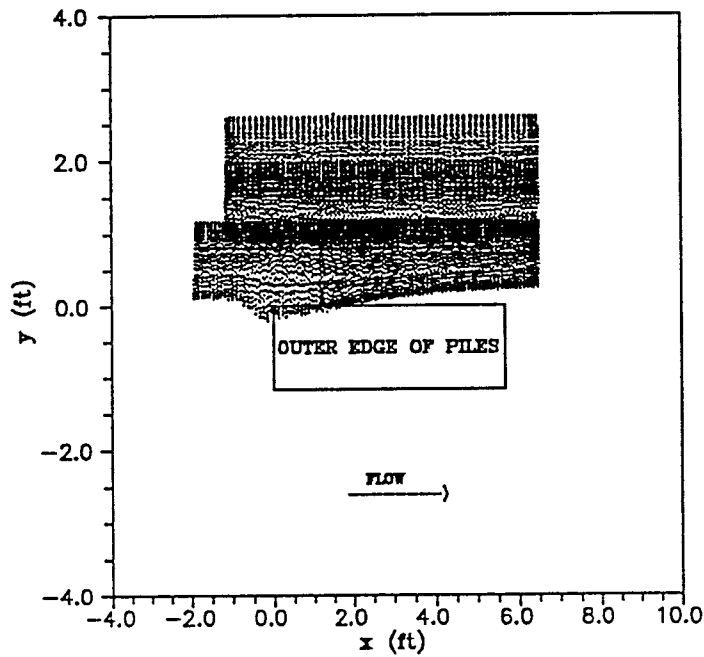


Figure B.15 Data points after completion of scour test S-1 (No pile cap structure).

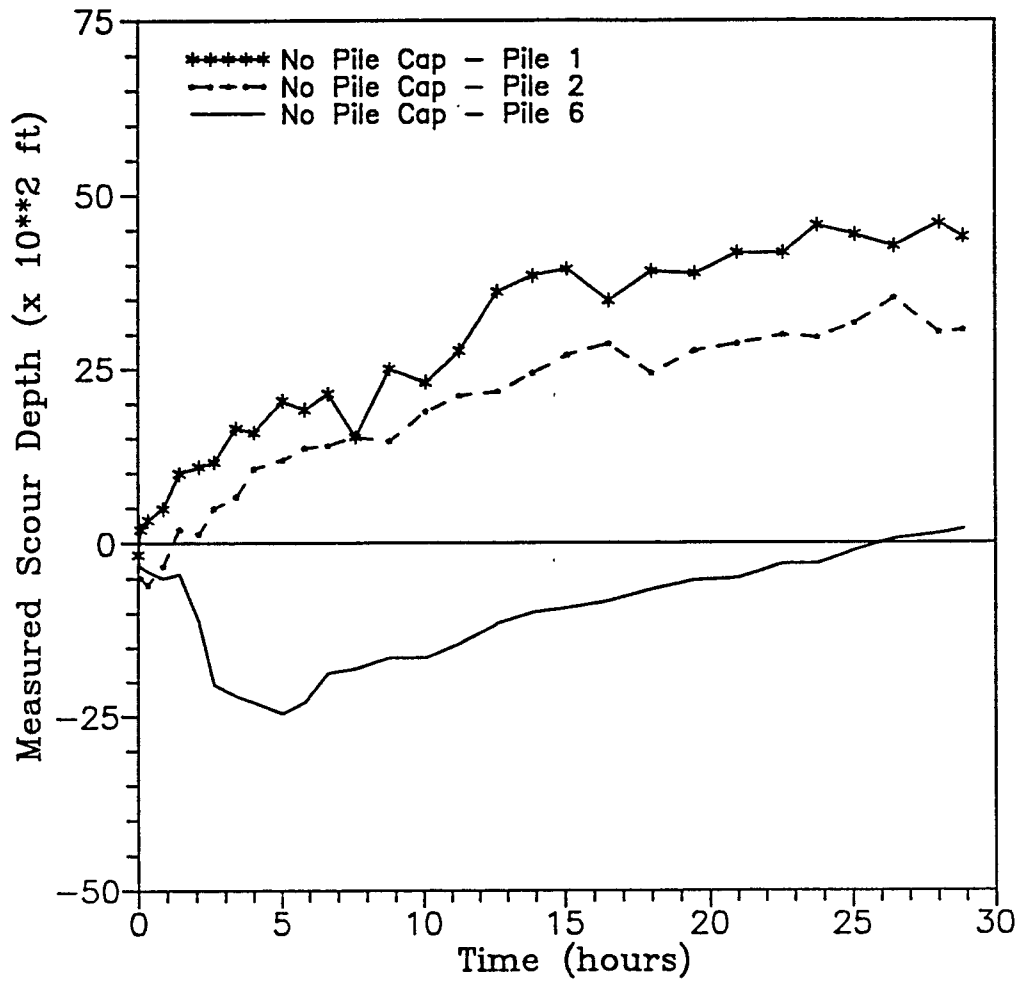


Figure B.16 Time rate of scour of piles 1, 2 and 6 of no pile cap structure.

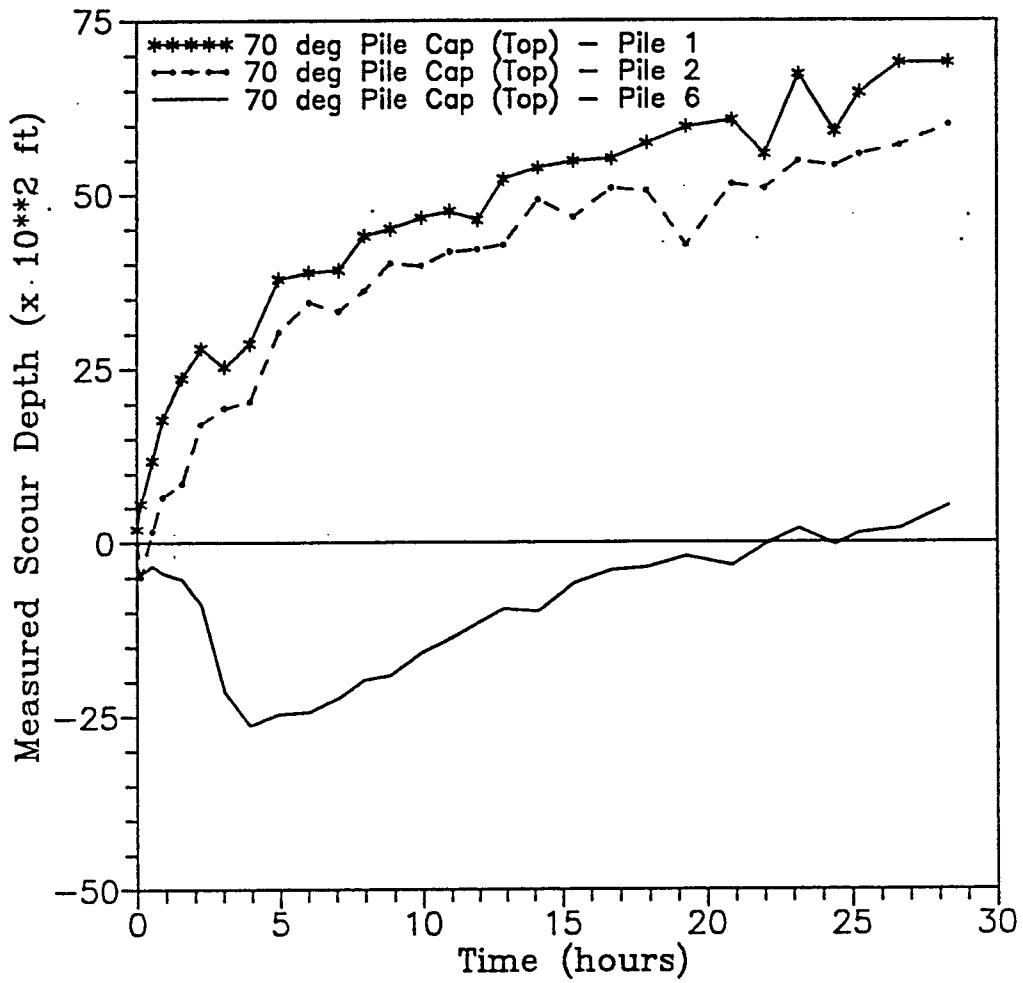


Figure B.17 Time rate of scour of piles 1, 2 and 6 of 70° pile cap (top position) structure.

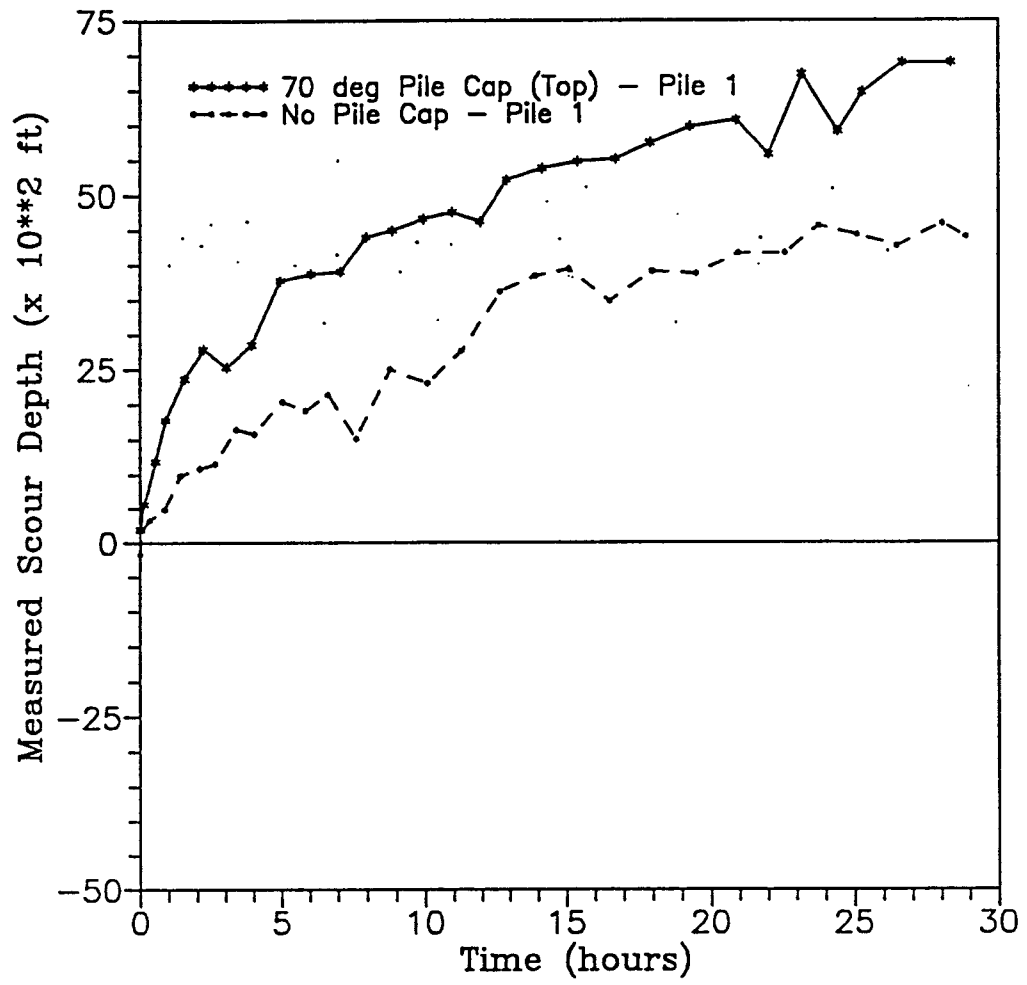


Figure B.18 Time rate of scour of pile 1.

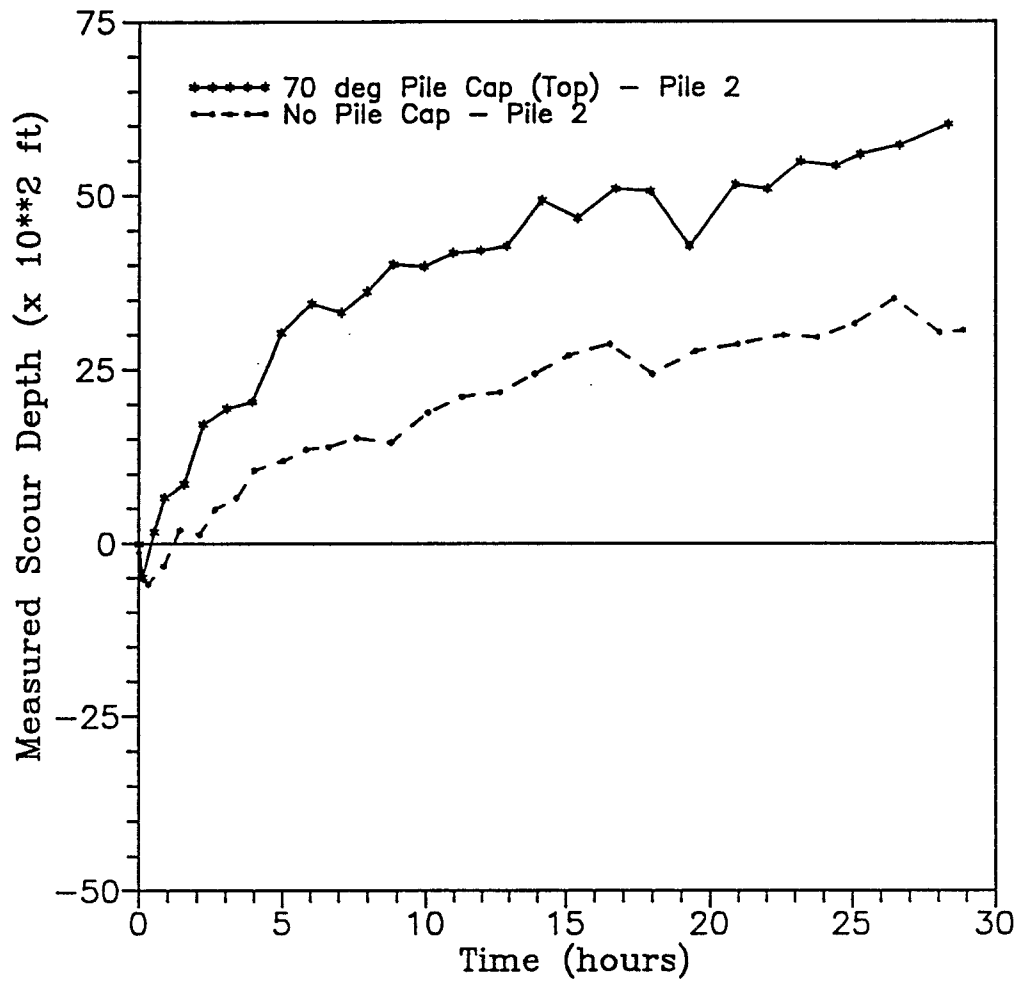


Figure B.19 Time rate of scour of pile 2.

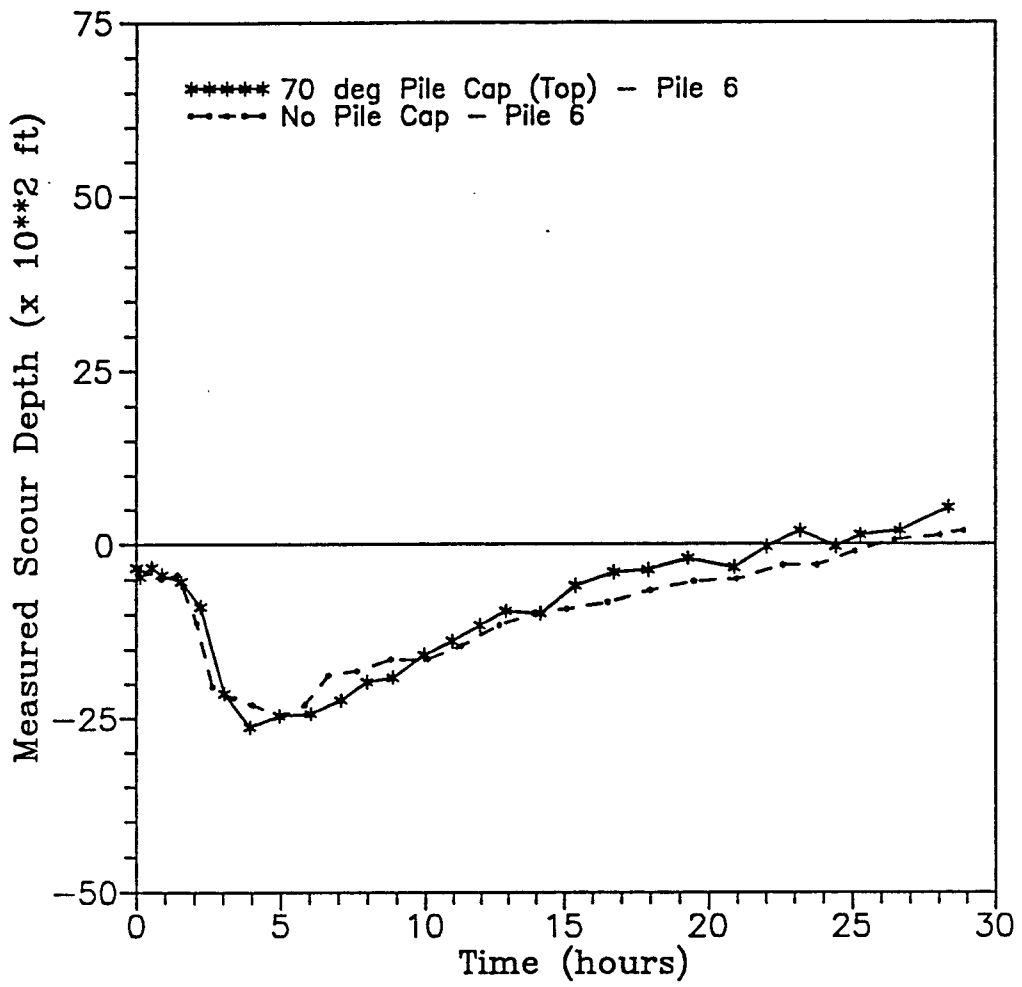


Figure B.20 Time rate of scour of pile 6.

APPENDIX C

ANALYSIS OF HYDRODYNAMIC AND SCOUR RESULTS

ANALYSIS OF HYDRODYNAMIC AND SCOUR RESULTS

C.1 Mathematical Model

Preliminary tests indicated that the X sensor probe had to be rotated 90° (such that the filaments were in parallel, horizontal planes) in order for the probe to resolve horizontal variations in the flow direction (see Appendix A). In this position, the probe measured the two horizontal components of velocity, U and V. It was assumed that the turbulent shear stress is proportional to $\rho(u'^2 + v'^2)$. The total shear stress would then be

$$\tau = \mu \frac{\partial \bar{U}}{\partial z} + a\rho(u'^2 + v'^2) \quad (C.1)$$

where "a" is a dimensionless constant to be determined from measurements in front of (and not influenced by) the structure. The analysis resulted in a value of 0.10 for "a".

The dimensionless shear stress, τ_d , was then computed at each grid point where flow measurements were made. The dimensionless shear stress is the ratio of the shear stress at any point, τ , and the shear stress of the undisturbed flow in front of the structure, τ_o , at $z = 0.12$ in. The surface fit program SURFER, was used to interpolate and map the dimensionless shear stress over the study area. SURFER was also used to fit the scour data. The grid laid out over a portion of the area expected to scour is shown in Figure A.4. With the existing probe support, hydrodynamic measurements closer than 0.364 ft to the piles could not be made due to the pile cap. This made it necessary to extrapolate the shear stress from the closest grid point to the piles.

In attempting to obtain a functional relationship between the equilibrium scour depth and the shear stress, the following guidelines were used. The relationship should be as simple as possible and be directed at the specific problem at hand. That is, it should be directed at equilibrium scour depths at the transition from clear water to live bed conditions thus eliminating the need to introduce sediment properties, etc. The thought being that this relationship could be extended to include a broader range of conditions at a later date. In light of the above, the following form was selected:

$$d_e = f(\tau), \quad (C.2)$$

where

d_e = equilibrium scour depth,

$$f(\tau) = b \left(\frac{\tau - \tau_o}{\tau_o} \right)^c = b (\tau_d - 1)^c, \quad (C.3)$$

$$\tau_d = \frac{\tau}{\tau_o}, \quad (\text{C.4})$$

and b and c are empirical coefficients.

Since the increase in bottom shear stress caused by the different multiple pile structures was the only parameter changing during the hydrodynamic experiments, the coefficients b and c were determined by a least squares fit between the predicted and estimated equilibrium scour depths at a section near the front of the pier. The coefficients are considered constant for the range of conditions considered here. For a more general formulation, the coefficients will undoubtedly be dependent on some of the quantities held constant during these experiments. Various sediment transport equations have been developed using the critical shear stress, τ_c and/or bed shear stress, τ_b . The shear stresses in these equations were raised to powers varying from 0.33 to 3 (see Table C.1).

The first step in evaluating the coefficients was to assign a value for c. Using the dimensionless shear stress, τ_d , and the measured scour depth at grid point A3, a value for b was computed. Grid point A3 (see Figure A.4) was selected because the time rate of scour curves in Figures B.16 and B.17 indicate that this area is close to its equilibrium scour depth. Grid point A2 was not chosen because τ_d is lower there than at A3. The reason being that point A2 is far enough forward that the flow at that point is less influenced by the structure. The values obtained for b and c are 0.152 and 0.5 ft respectively.

SURFER was then used to create a finer grid of the estimated shear stresses and the corresponding scour depths at these grid points were computed using Equation C.2. One constraint on the computed equilibrium scour depths was that the scour depth between two adjacent grid points could not change more than that allowed by the sediment angle of repose, 32° (Melville and Raudkivi, 1977). The predicted equilibrium scour depth is the larger between the scour depth based on the dimensionless shear stress and the scour depth which satisfies the sediment angle of repose.

To simplify the presentation of the results, bottom elevations instead of predicted and measured scour depths are presented. Bottom elevation, z, and scour depth, d_e , are related by $z = -d_e$. Figures C.1 to C.12 show τ_d , the measured bottom elevation after a 28 hour scour test, and the predicted equilibrium bottom elevations for the no pile cap and the 70° pile cap (top position) structures. The estimated equilibrium bottom elevation shown in Figure C.8 is the measured bottom elevation at 28 hours extrapolated to equilibrium and adjusted for the velocity being below the transition between live bed and clear water conditions. The extrapolation involved dividing the scour depths by 0.9 and multiplying by 1.14. The results indicate that the predicted equilibrium bottom elevations are closer to the measured bottom elevations towards the front of the structure. Figures C.13 and C.14 are contours of dimensionless shear stress around the no pile cap and 70° pile cap (top position) structures. Figures C.15 and C.17 are the measured bottom elevations over the same area.

Figures C.16 and C.18 are contours of the predicted equilibrium bottom elevations (for the area where hydrodynamic flow measurements were made) based on the dimensionless shear stresses in Figures C.13 and C.14. These figures show that the computed equilibrium bottom elevations are deeper than the measured values throughout the area but the difference is greater toward the back of the structure. This is one indication that the scour is much closer to equilibrium near the front of the structure. Figures C.19 and C.20 show the 70° pile cap (top position) before and after the scour test.

Figure C.21 shows the results at row 3 ($x = 1.31$ ft) for the 70° pile cap (bottom position) structure. The predicted equilibrium bottom elevations do not match the measured bottom elevations for the cases where the pile cap was initially resting on the bottom (see Figures C.22 and C.23). This however, is to be expected since for these cases the structure shape near the bottom changes abruptly with the development of the scour hole. The scour predictions are better suited for a structure with a pile cap that starts 0.42 ft above the bottom and penetrates deep below the bottom. The scour test results for the cases where the pile cap rests on the bottom should not be compared with the hydrodynamic test data for these structures for the above stated reasons.

Flow measurements closer to the structure are clearly needed. As stated earlier, time and cost constraints prevented the necessary modifications to the constant temperature probe support to allow these measurements. Such measurements will be included in future studies. One possible improvement would be to use flush mounted shear stress probes in the vicinity of the structure where flows are highly unsteady and the shear stresses are large.

Table C.1 Some formulas for bed load and total load (Sleath, 1984).

Investigator	Formula	Comments
Du Boys (1879)	$Q_s = A\tau_o(\tau_o - \tau_c)$	Bed Load
O'Brien and Rindlaub (1934)	$Q_s = A(\tau_o - \tau_c)^m$	Bed Load
Shields (1936)	$Q_s = AQS(\tau_o - \tau_c) / ((\rho_s - \rho)gd)$	Bed Load
Brown (1950)	$Q_s = AD^{3/2}(\tau_o / (\rho_s - \rho)gd)^3$	Bed Load
Garde and Albertson (1958)	$Q_s = Q(D/d)f(D) / (u_*d/\nu)^{2/3}$	Total Load
Chang (1967)	$Q_s = A\bar{U}(\tau_o - \tau)$	Total Load

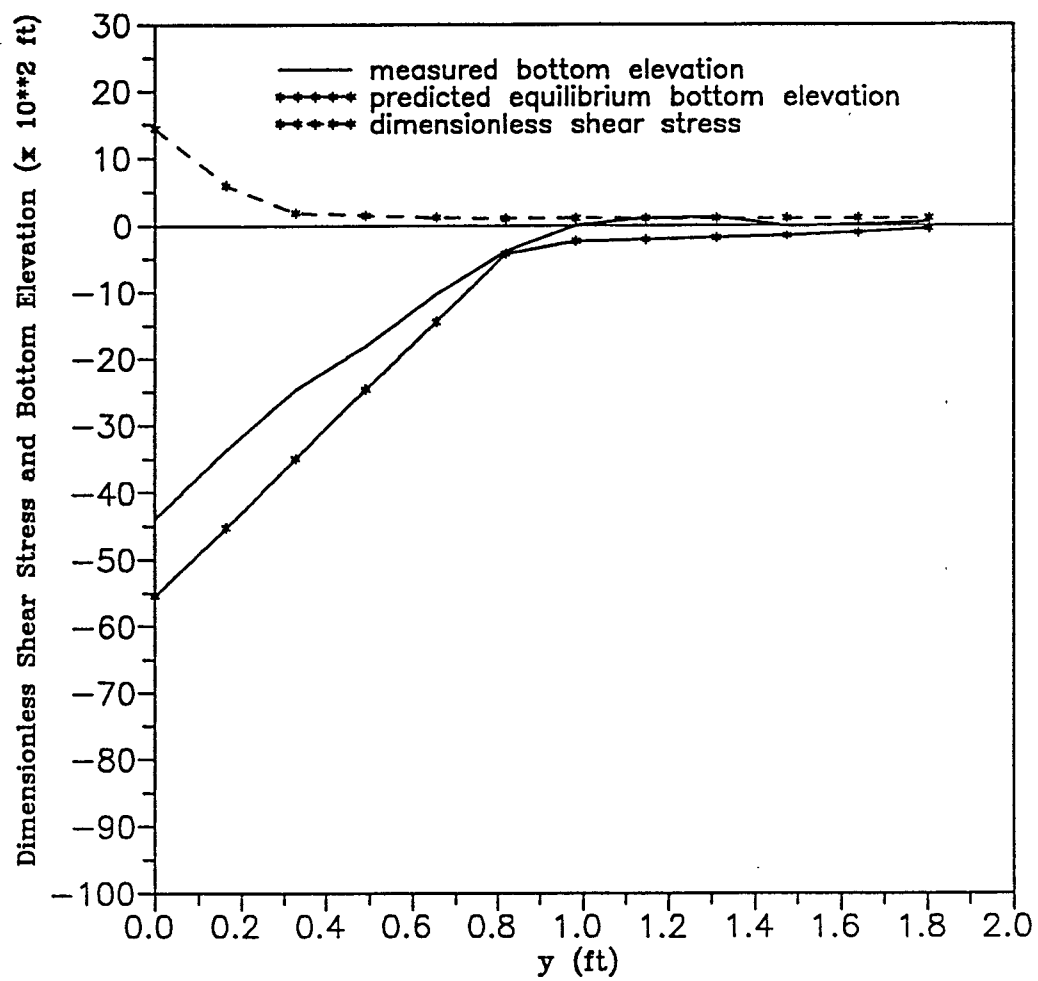


Figure C.1 Comparison of measured bottom elevation, predicted equilibrium bottom elevation and dimensionless shear stress for the no pile cap structure (row 2 : $x = 0.33$ ft).

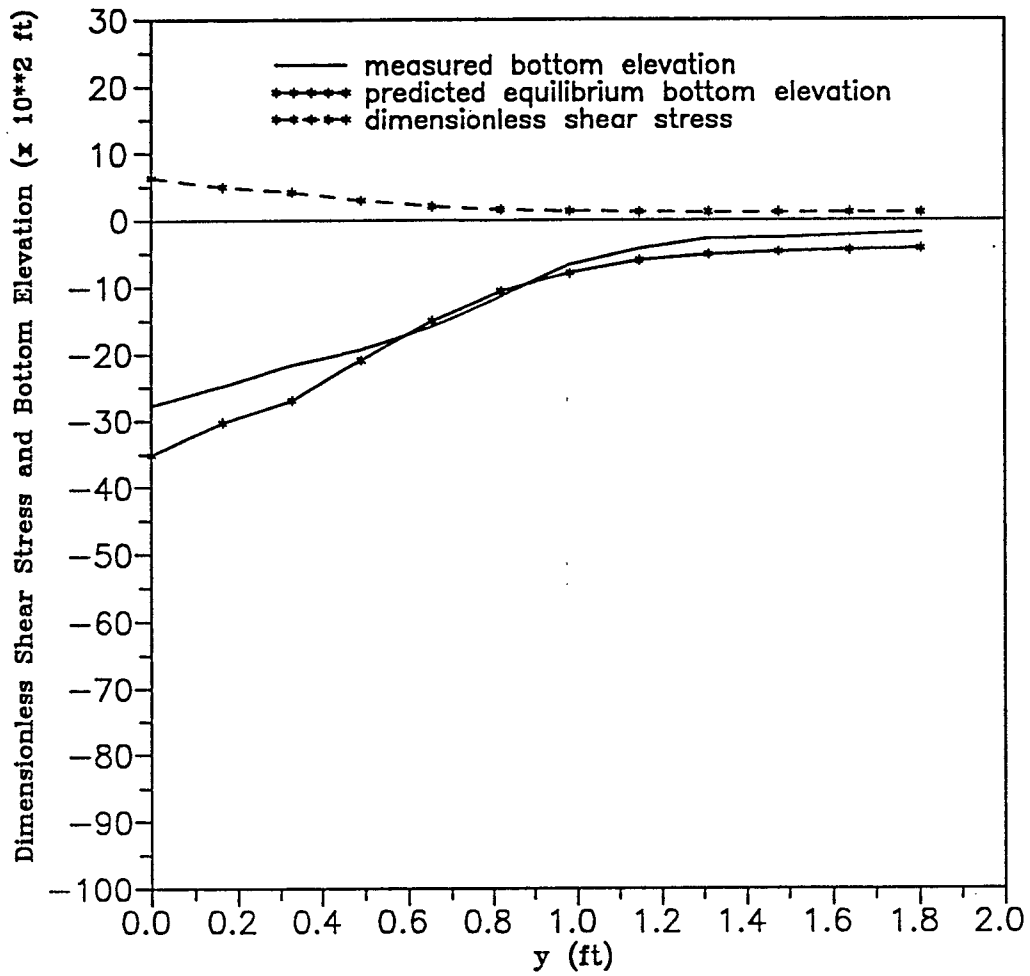


Figure C.2 Comparison of measured bottom elevation, predicted equilibrium bottom elevation and dimensionless shear stress for the no pile cap structure (row 3 : $x = 1.31$ ft).

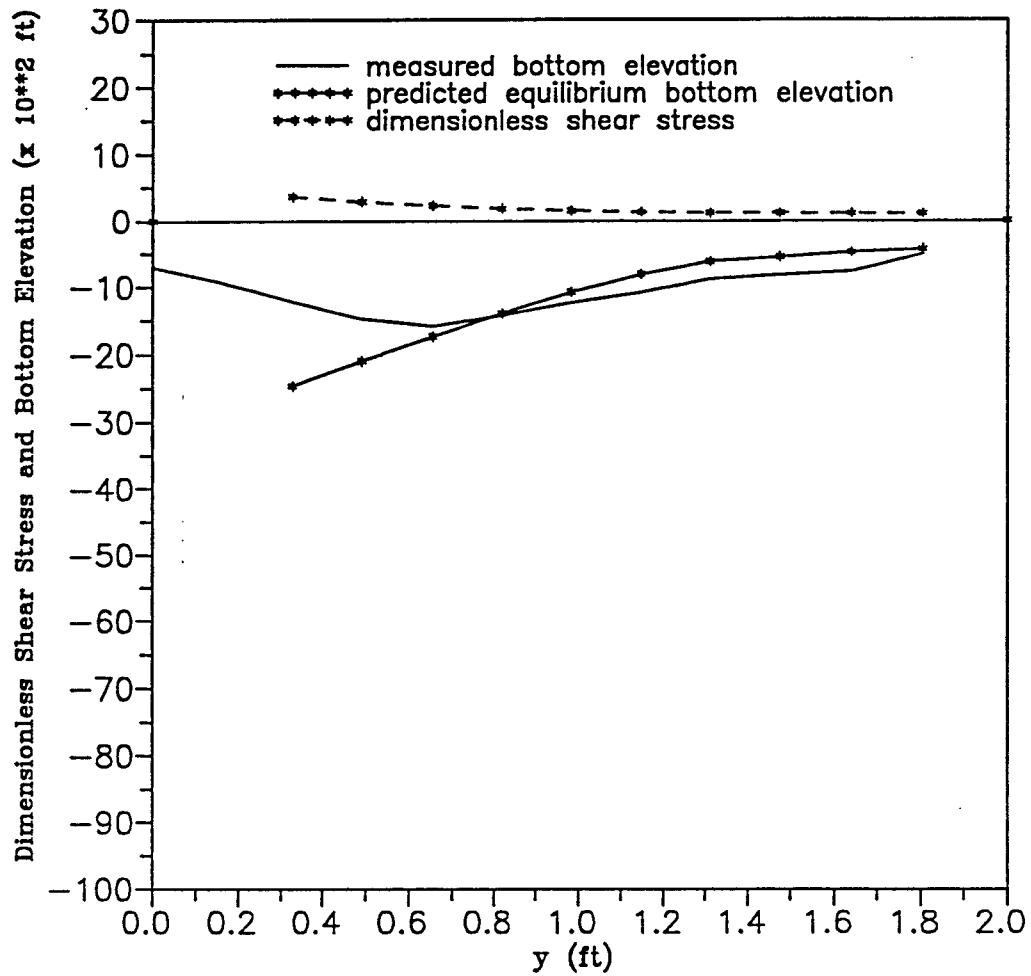


Figure C.3 Comparison of measured bottom elevation, predicted equilibrium bottom elevation and dimensionless shear stress for the no pile cap structure (row 4 : $x = 2.30$ ft).

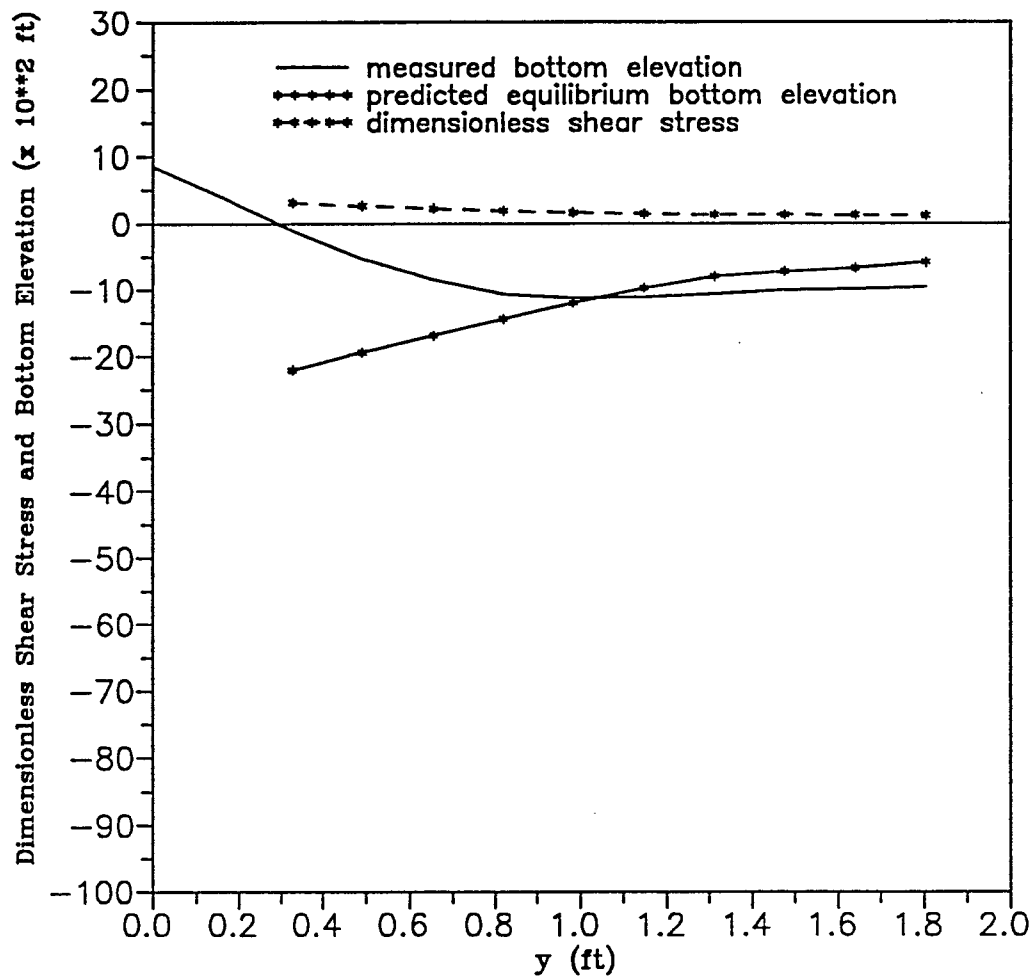


Figure C.4 Comparison of measured bottom elevation, predicted equilibrium bottom elevation and dimensionless shear stress for the no pile cap structure (row 5 : $x = 3.28$ ft).

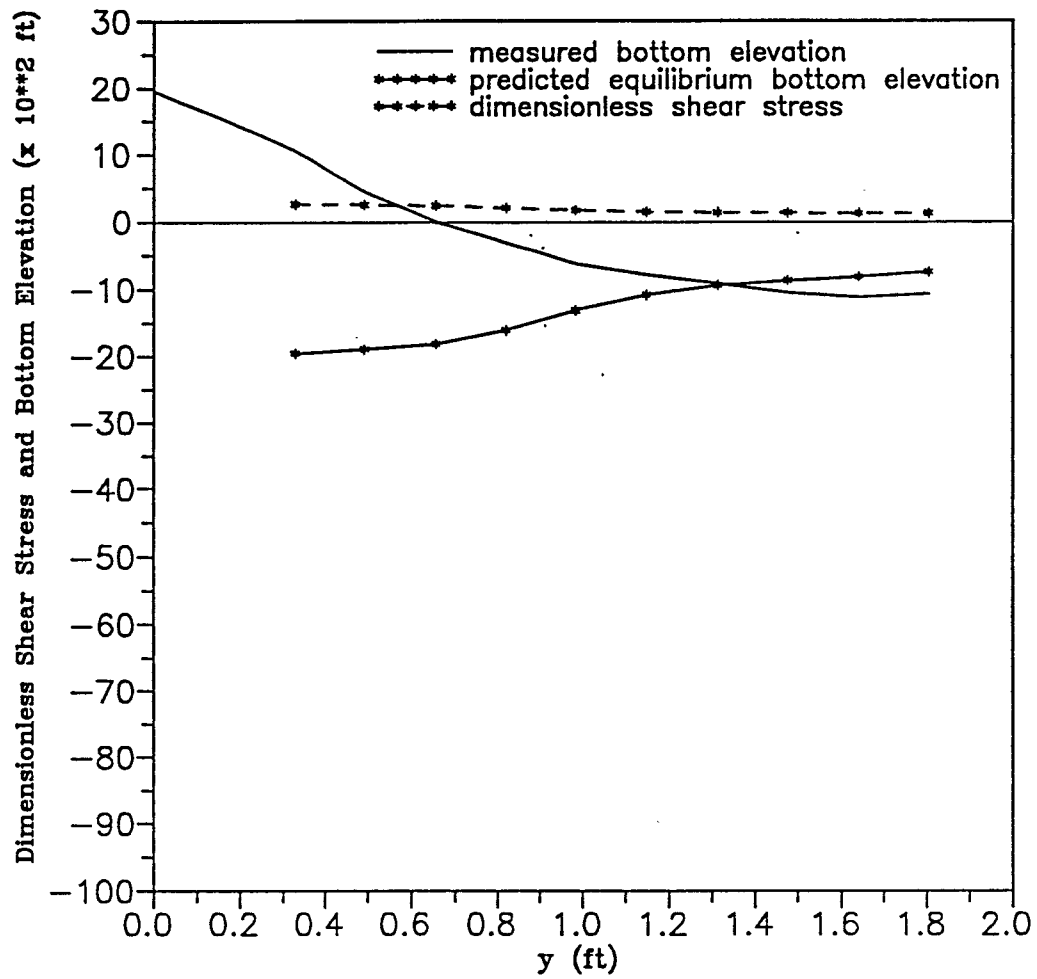


Figure C.5 Comparison of measured bottom elevation, predicted equilibrium bottom elevation and dimensionless shear stress for the no pile cap structure (row 6 : $x = 4.27$ ft).

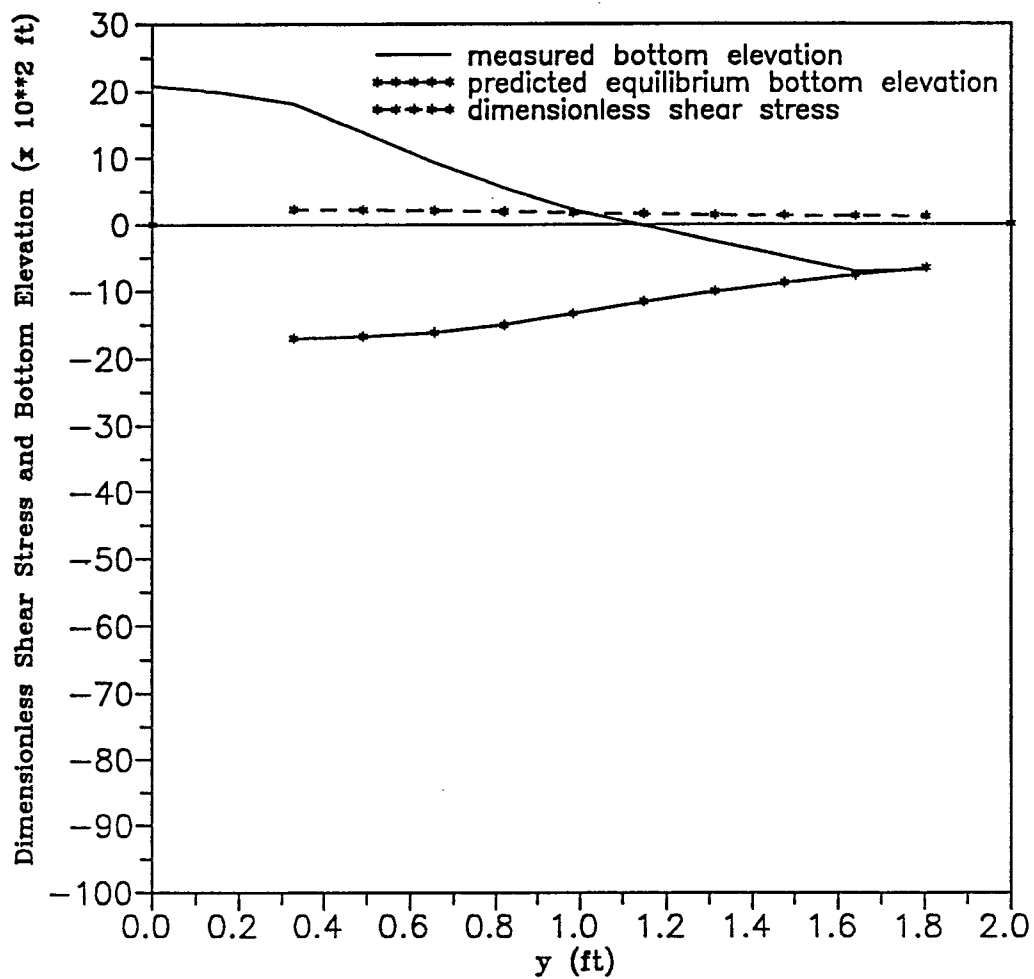


Figure C.6 Comparison of measured bottom elevation, predicted equilibrium bottom elevation and dimensionless shear stress for the no pile cap structure (row 7 : $x = 5.25$ ft).

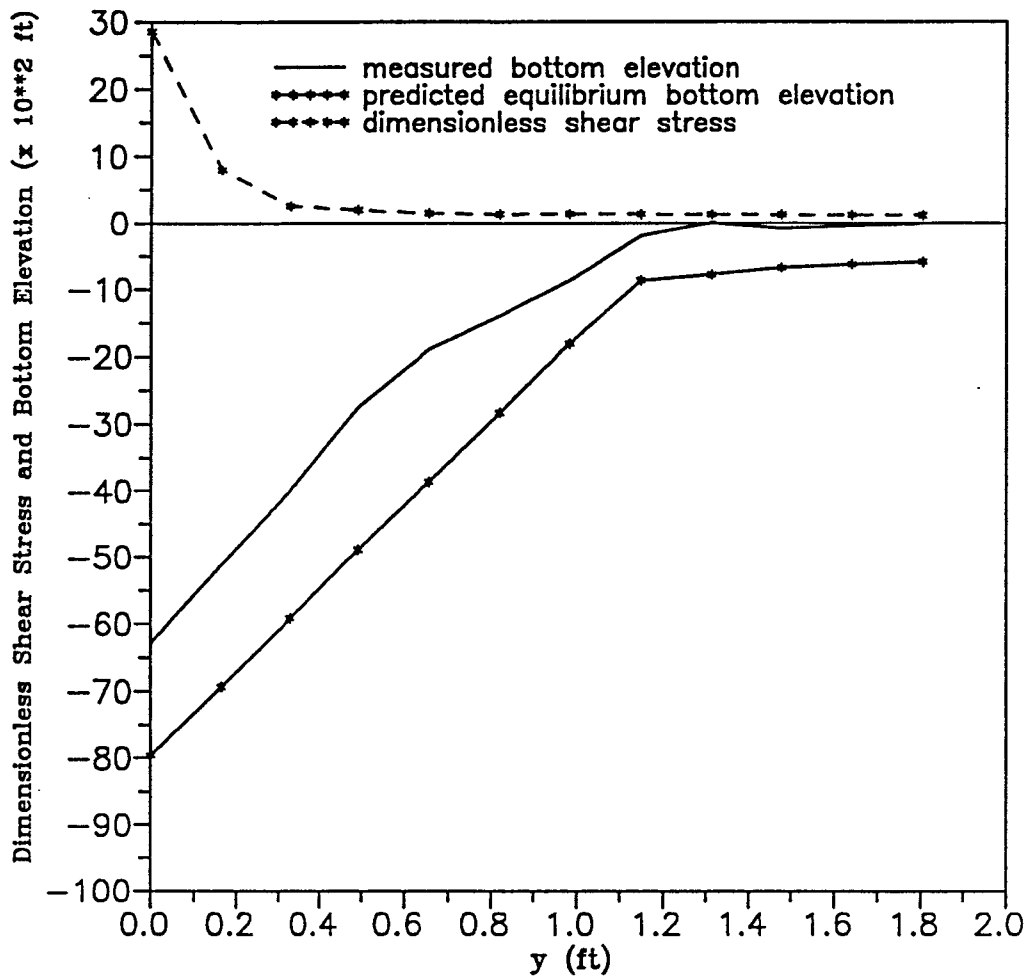


Figure C.7 Comparison of measured bottom elevation, predicted equilibrium bottom elevation and dimensionless shear stress for 70° pile cap (top) structure (row 2 : $x = 0.33$ ft).

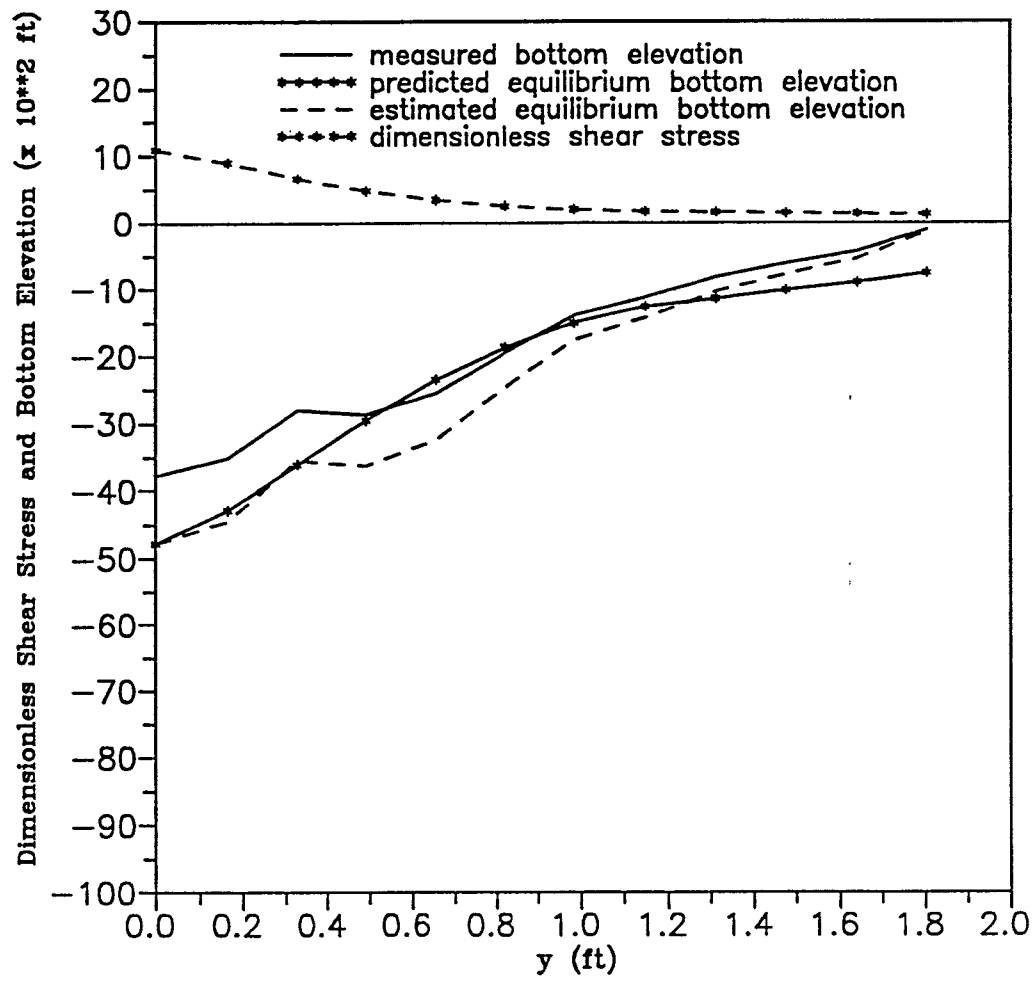


Figure C.8 Comparison of measured bottom elevation, estimated and predicted equilibrium bottom elevations and dimensionless shear stress for the 70° pile cap (top) structure (row 3 : $x = 1.31$ ft).

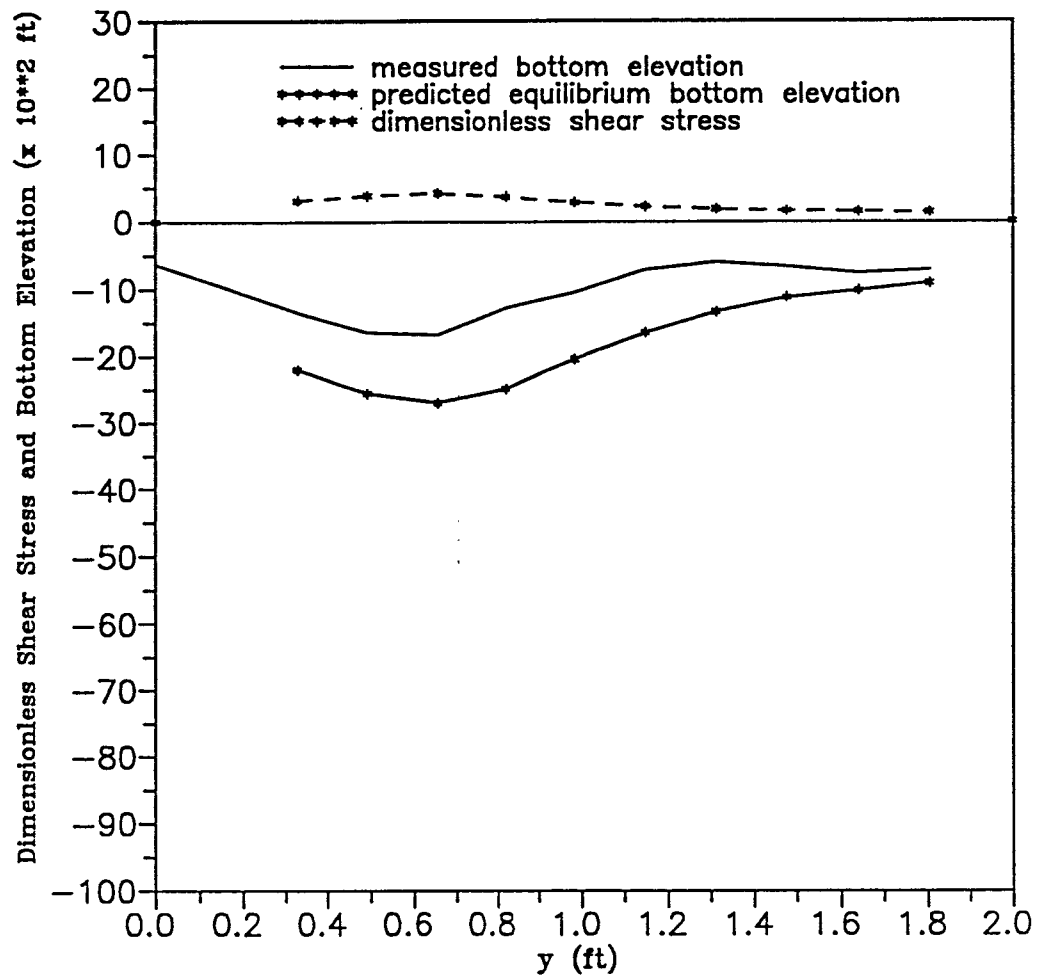


Figure C.9 Comparison of measured bottom elevation, predicted equilibrium bottom elevation and dimensionless shear stress for the 70° pile cap (top) structure (row 4 : $x = 2.30$ ft).

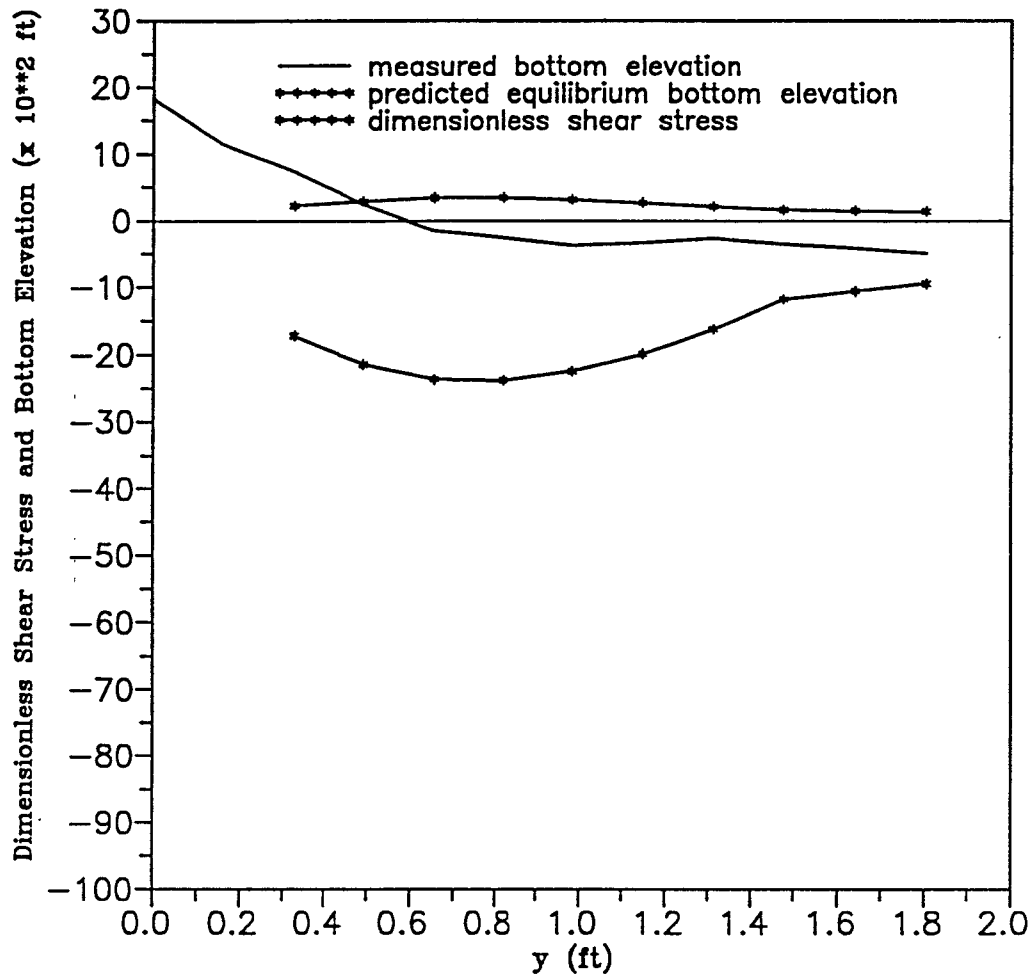


Figure C.10 Comparison of measured bottom elevation, predicted equilibrium bottom elevation and dimensionless shear stress for the 70° pile cap (top) structure (row 5 : $x = 3.28$ ft).

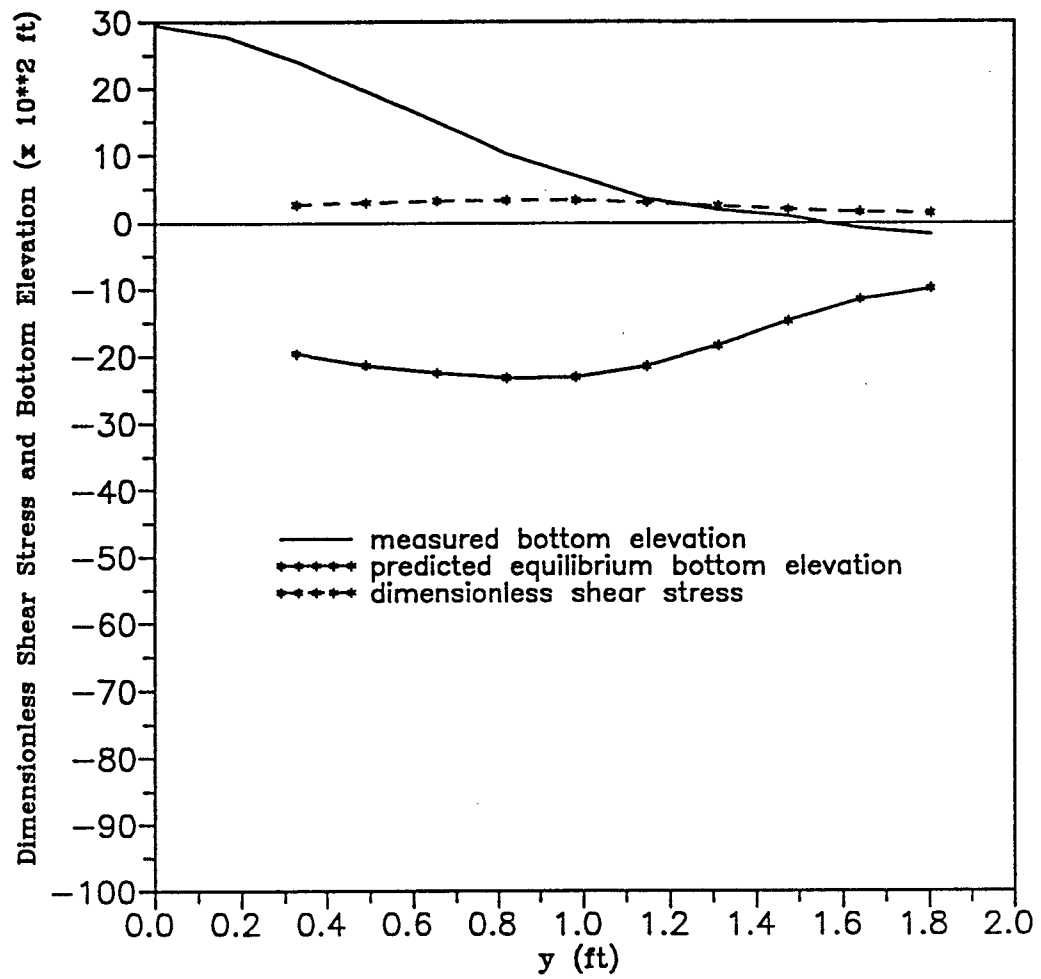


Figure C.11 Comparison of measured bottom elevation, predicted equilibrium bottom elevation and dimensionless shear stress for the 70° pile cap (top) structure (row 6 : $x = 4.27$ ft).

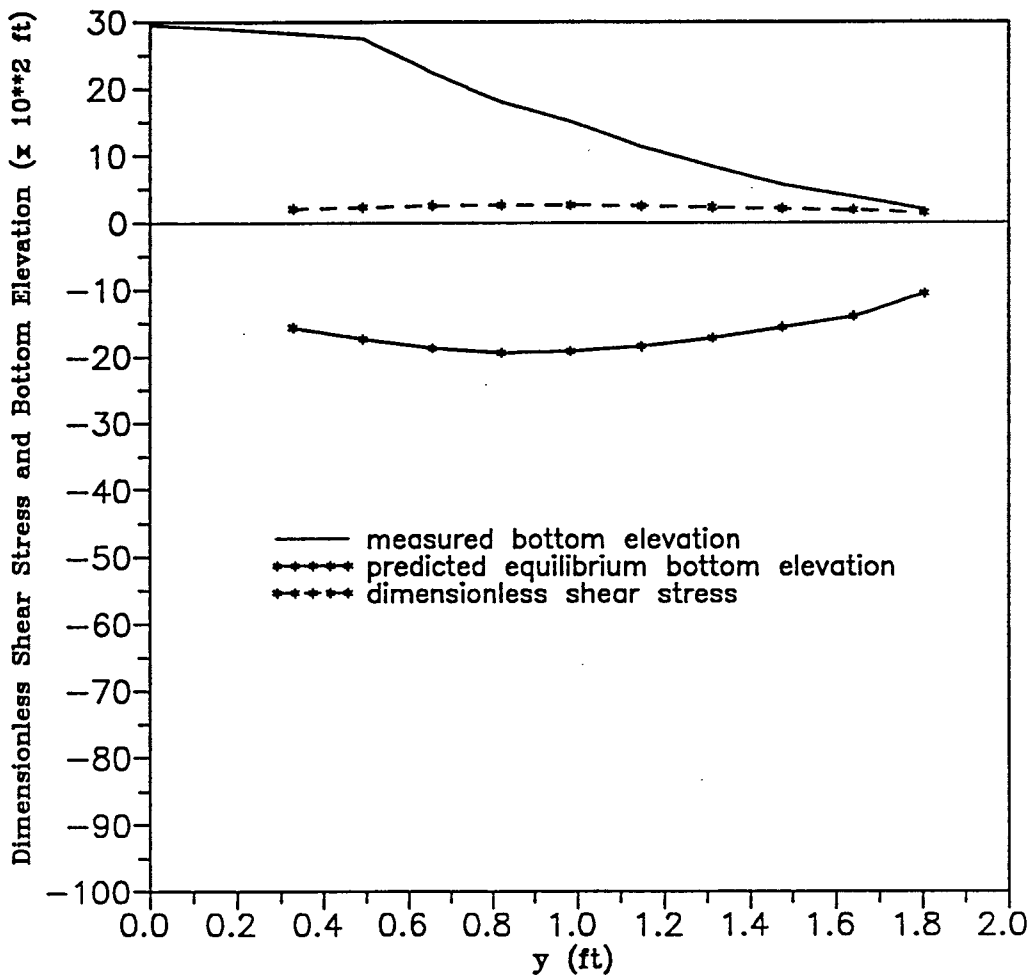


Figure C.12 Comparison of measured bottom elevation, predicted equilibrium bottom elevation and dimensionless shear stress for the 70° pile cap (top) structure (row 7 : $x = 5.25$ ft).

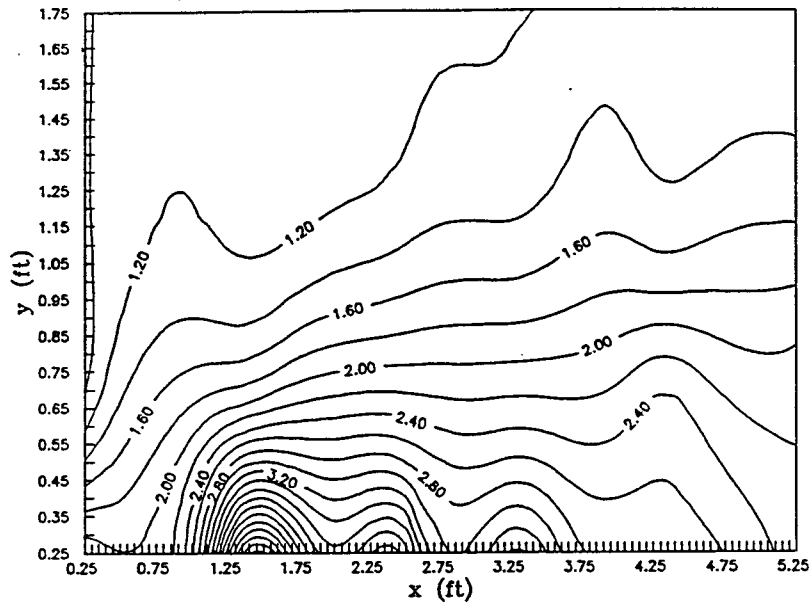


Figure C.13 Contours of dimensionless shear stress, τ_d , around no pile cap structure.

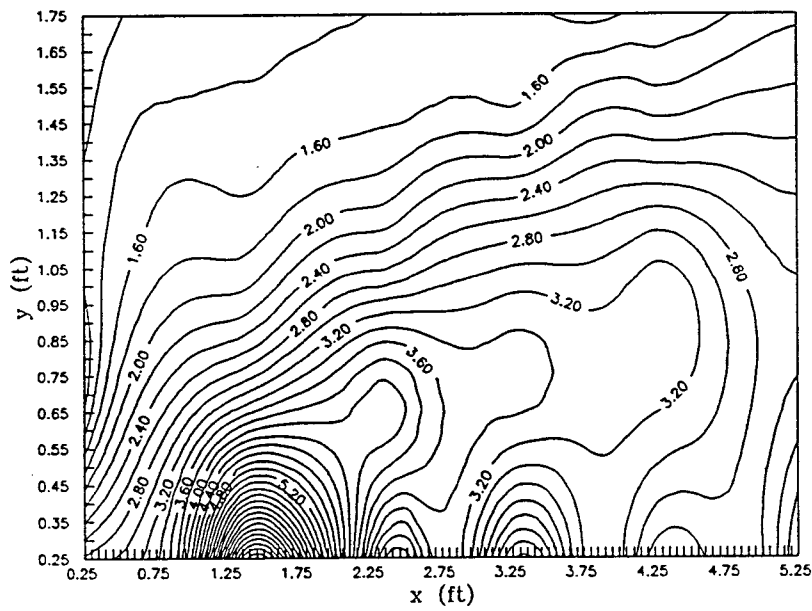


Figure C.14 Contours of dimensionless shear stress, τ_d , around 70° pile cap (top position) structure.

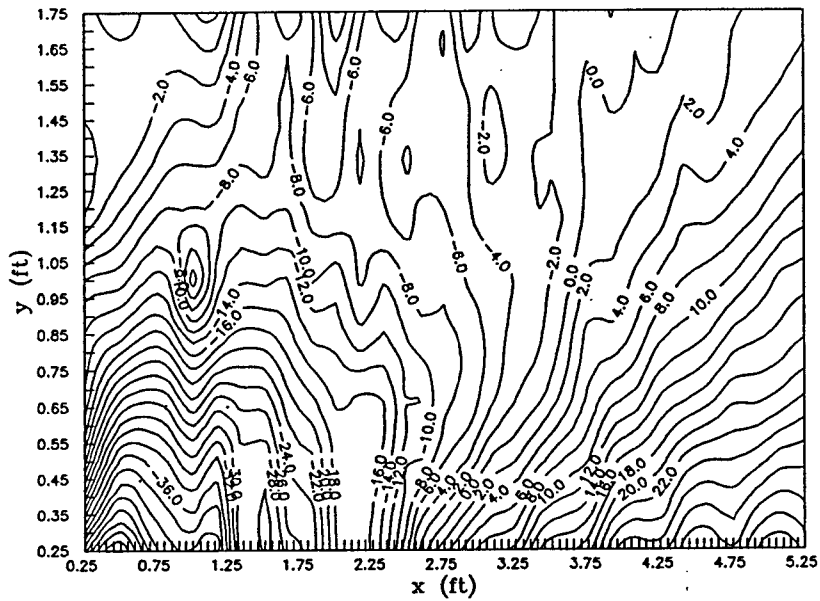


Figure C.17 Contours of measured bottom elevation $\times 10^2$ (ft) around 70° pile cap (top position) structure after completion of scour test.

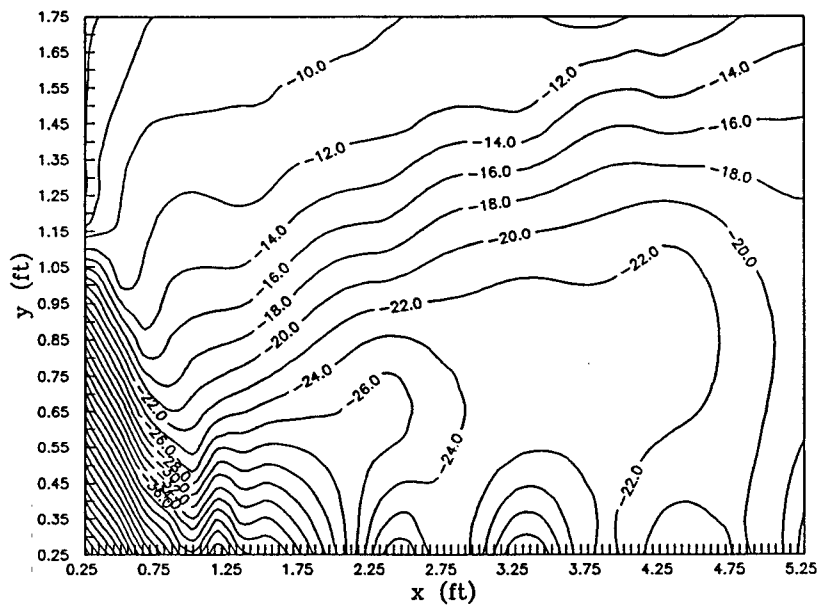


Figure C.18 Contours of predicted equilibrium bottom elevation $\times 10^2$ (ft) around 70° pile cap (top position) structure.

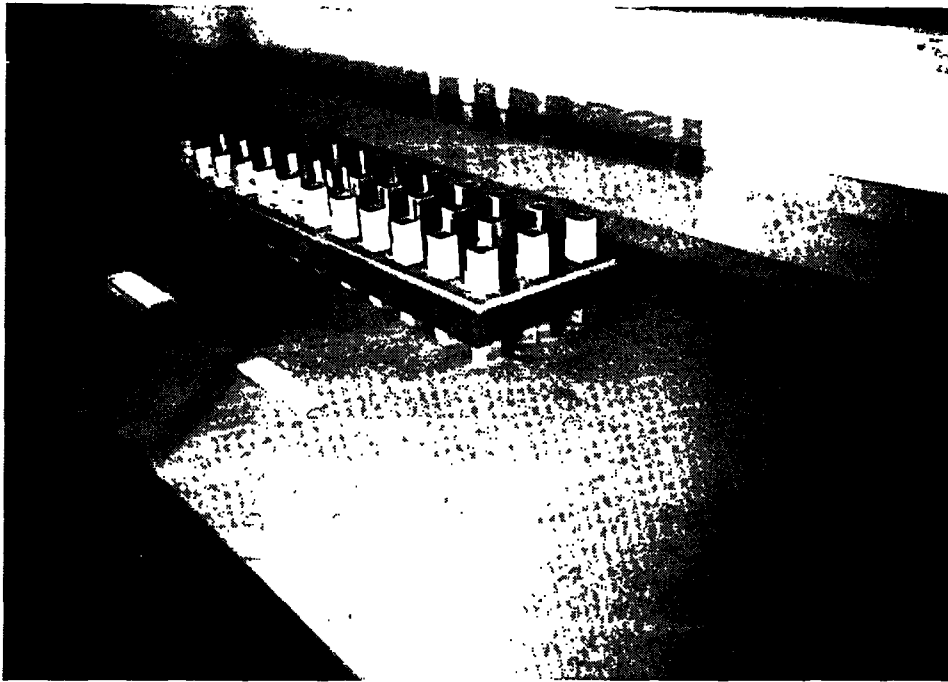


Figure C.19 70° pile cap (top position) structure before the scour test.

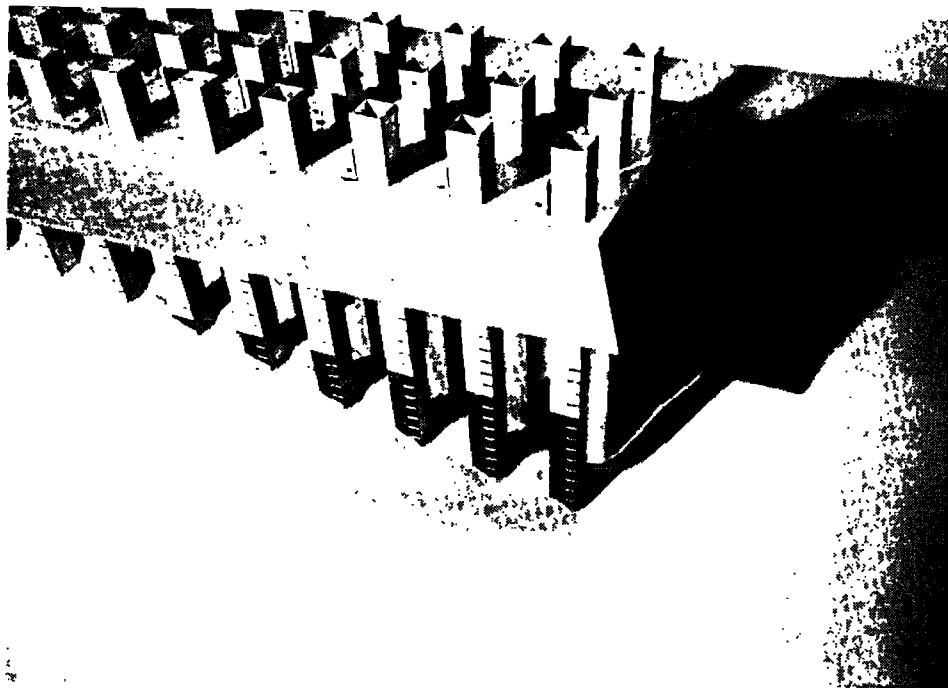


Figure C.20 70° pile cap (top position) structure after completion of the scour test.

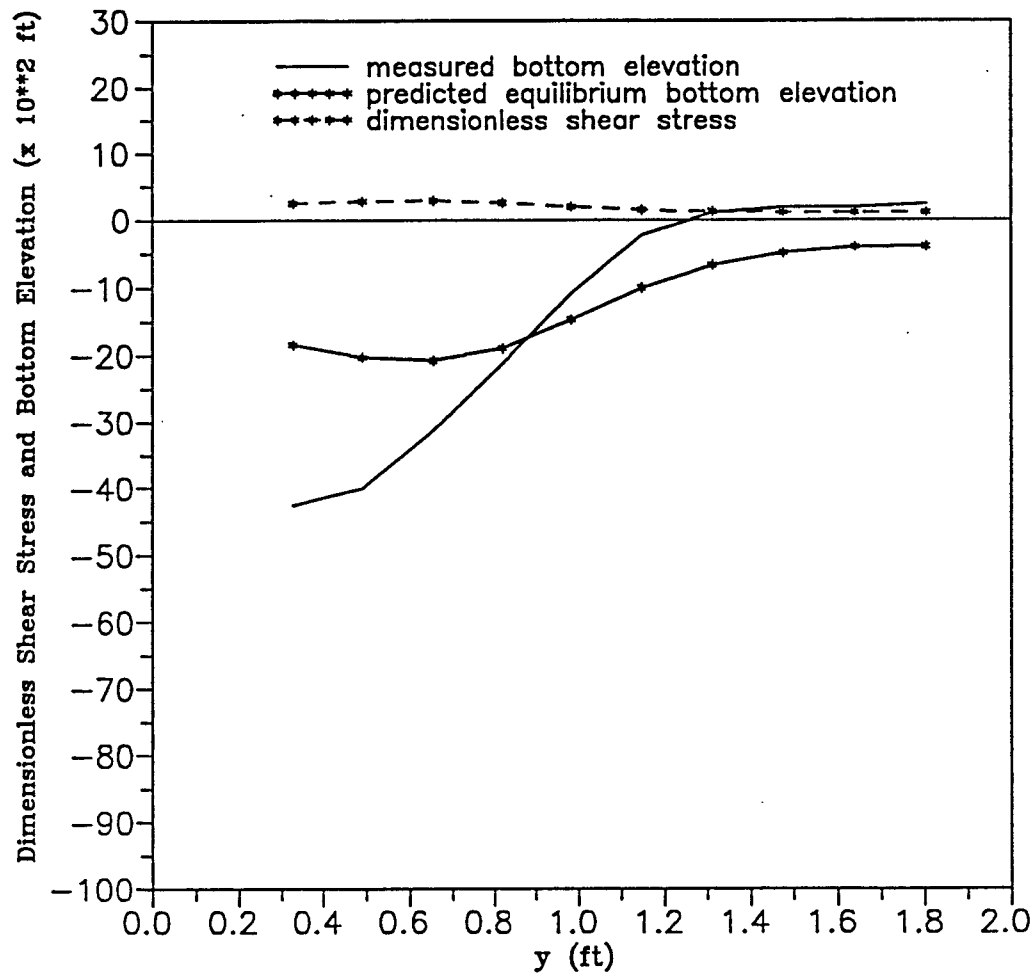


Figure C.21 Comparison of measured bottom elevation, predicted equilibrium bottom elevation and dimensionless shear stress for 70° pile cap (bottom) structure (row 3 : $x = 1.31$ ft).

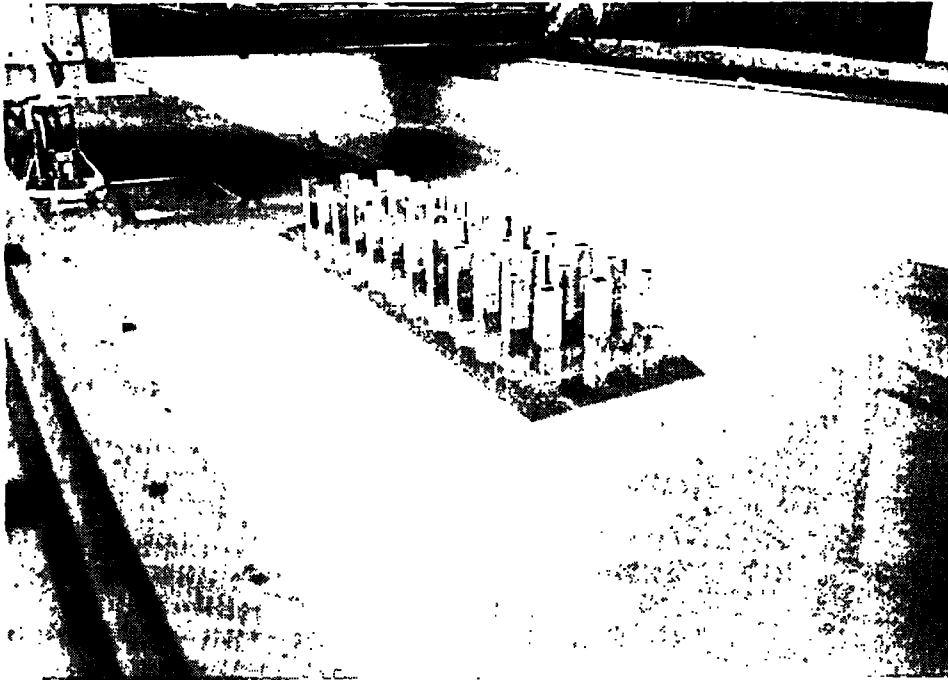


Figure C.22 70° pile cap (bottom position) structure before the scour test.

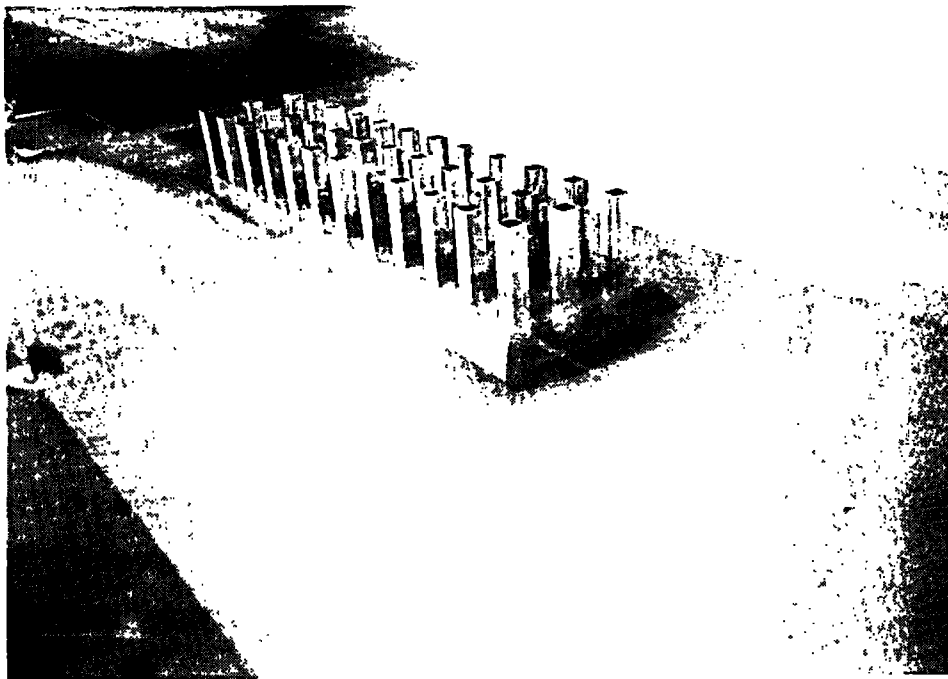


Figure C.23 70° pile cap (bottom position) structure after completion of the scour test.

APPENDIX D

DATA

DATA

Table D.1 Values of x and y at grid points of hydrodynamic study.

Grid Point*	x (ft)	y (ft)
A1	-4.92	0.36
A2	0.33	0.36
A3	1.40	0.36
A4	2.34	0.36
A5	3.33	0.36
A6	4.33	0.36
A7	5.40	0.36
B1	-4.92	0.69
B2	0.33	0.69
B3	1.40	0.69
B4	2.34	0.69
B5	3.33	0.69
B6	4.33	0.69
B7	5.40	0.69
C1	-4.92	1.02
C2	0.33	1.02
C3	1.40	1.02
C4	2.34	1.02
C5	3.33	1.02
C6	4.33	1.02
C7	5.40	1.02

* See Figure A.4.

Table D.1--continued

D1	-4.92	1.46
D2	0.33	1.46
D3	1.40	1.46
D4	2.34	1.46
D5	3.33	1.46
D6	4.33	1.46
D7	5.40	1.46
E1	-4.92	1.99
E2	0.33	1.99
E4	2.34	1.99
E6	4.33	1.99

Table D.2 Results of hydrodynamic test H-1.

Structure = No Pile Cap (0° to flow)
 μ = $1.67 \times 10^{-5} \text{ lb}_f \cdot \text{sec}/\text{ft}^2$
 ρ = $62.17 \text{ lb}_m/\text{ft}^3$

Grid Point	Time Mean Velocity ft/sec	Turbulent Energy/ Unit Mass ft ² /sec ² x 10 ²	τ_v lb _f /ft ² x 10 ³	τ_t lb _f /ft ² x 10 ³	τ lb _f /ft ² x 10 ³	$\frac{\tau}{\tau_o}$
A1	0.68	1.83	1.15	3.53	4.68	0.957
A2	0.99	3.52	1.67	6.81	8.48	1.733
A3	0.96	8.69	1.63	16.8	18.4	3.763
A4	0.76	7.73	1.29	14.9	16.2	3.319
A5	0.71	6.78	1.21	13.1	14.3	2.922
A6	0.72	6.00	1.23	11.6	12.8	2.619
A7	0.52	5.07	0.88	9.80	10.7	2.182
A1	0.70	2.04	1.19	3.95	5.12	1.048
B1	0.70	2.03	1.19	3.91	5.10	1.043
B2	0.91	2.09	1.55	4.03	5.58	1.142
B3	0.94	3.82	1.59	7.37	8.98	1.834
B4	0.86	4.81	1.46	9.29	10.7	2.195
B5	0.84	4.76	1.42	9.21	10.6	2.172
B6	0.88	5.39	1.48	10.4	11.9	2.433
B7	0.72	4.87	1.21	9.42	10.6	2.172
B1	0.70	2.01	1.19	3.88	5.08	1.039
C1	0.70	1.87	1.19	3.61	4.80	0.982
C2	0.82	1.87	1.38	3.61	4.99	1.021
C3	0.83	2.39	1.40	4.62	6.04	1.233
C4	0.82	2.95	1.40	5.70	7.08	1.448

Table D.2--continued

C5	0.81	3.26	1.38	6.29	7.69	1.570
C6	0.85	3.43	1.44	6.62	8.06	1.650
C7	0.74	3.62	1.25	6.70	8.25	1.687
C1	0.69	1.90	1.17	3.68	4.82	0.987
D1	0.65	1.74	1.11	3.36	4.47	0.913
D2	0.77	1.73	1.29	3.34	4.66	0.950
D3	0.75	2.16	1.27	4.18	5.45	1.116
D4	0.77	2.20	1.32	4.24	5.56	1.134
D5	0.78	2.41	1.32	4.66	5.99	1.223
D6	0.82	2.62	1.38	5.05	6.45	1.319
D7	0.76	2.68	1.29	5.18	6.47	1.322
D1	0.70	1.97	1.19	3.80	4.97	1.018
E1	0.67	1.84	1.13	3.55	4.68	0.957
E2	0.76	1.83	1.29	3.53	4.82	0.987
E4	0.79	2.06	1.36	3.97	5.33	1.087
E6	0.78	2.23	1.32	4.30	5.62	1.149
E1	0.67	1.91	1.15	3.68	4.82	0.986
A1	0.72	2.08	1.23	4.01	5.24	1.071

Estimated Shear Stress Away from Influence of Structure

Grid Point = A1 (x = -4.92 ft; y = 0.364 ft; z = 0.12 in)

$$\tau_o = \tau_{vo} + \tau_{to}$$

$$\tau_{vo} = \mu \, du/dy$$

$$\tau_{to} = a\rho(u'^2 + v'^2)$$

$$a = 0.10$$

$$\tau_{vo} = \text{viscous shear stress} = 1.17 \times 10^{-3} \text{ lb}_f/\text{ft}^2$$

$$\tau_{to} = \text{turbulent shear stress} = 3.72 \times 10^{-3} \text{ lb}_f/\text{ft}^2$$

$$\tau_o = 4.89 \times 10^{-3} \text{ lb}_f/\text{ft}^2$$

Table D.3 Results of hydrodynamic test H-2.

Structure = 70° Pile Cap - Top Position (0° to flow)
 $\mu = 1.67 \times 10^{-5} \text{ lb}_f \cdot \text{sec}/\text{ft}^2$
 $\rho = 62.17 \text{ lb}_m/\text{ft}^3$

Grid Point	Time Mean Velocity ft/sec	Turbulent Energy/ Unit Mass $\text{ft}^2/\text{sec}^2 \times 10^2$	τ_v $\text{lb}_f/\text{ft}^2 \times 10^3$	τ_t $\text{lb}_f/\text{ft}^2 \times 10^3$	τ $\text{lb}_f/\text{ft}^2 \times 10^3$	$\frac{\tau}{\tau_o}$
A1	0.60	1.46	1.02	2.82	3.84	0.811
A2	1.16	4.69	1.96	9.06	11.0	2.329
A3	0.71	14.2	1.19	27.4	28.6	6.038
A4	0.45	7.75	0.77	15.0	15.7	3.324
A5	0.42	5.89	0.71	11.4	12.1	2.556
A6	0.44	6.40	0.75	12.4	13.1	2.768
A7	0.34	4.29	0.58	8.29	8.85	1.872
A1	0.65	1.91	1.09	3.70	4.78	1.011
B1	0.64	1.88	1.09	3.63	4.72	0.996
B2	0.94	2.69	1.59	5.20	6.79	1.432
B3	0.93	7.11	1.59	13.7	15.3	3.236
B4	0.79	9.82	1.36	19.0	20.3	4.292
B5	0.66	8.05	1.13	15.5	16.7	3.520
B6	0.66	7.34	1.13	14.2	15.3	3.234
B7	0.53	5.82	0.90	11.3	12.2	2.567
B1	0.63	1.90	1.09	3.67	4.76	1.005
C1	0.60	1.90	1.02	3.65	4.68	0.988
C2	0.90	2.53	1.52	4.89	6.43	1.357
C3	0.85	3.93	1.44	7.58	9.04	1.909
C4	0.79	5.67	1.34	11.0	12.3	2.600

Table D.3--continued

D1	0.61	1.81	1.04	3.49	4.53	0.958
D2	0.86	2.31	1.46	4.45	5.91	1.250
D3	0.83	3.00	1.42	5.81	7.20	1.524
D4	0.77	3.09	1.29	5.97	7.29	1.538
D5	0.76	3.49	1.29	6.75	8.02	1.695
D6	0.79	4.23	1.36	8.17	9.52	2.012
D7	0.74	4.42	1.25	8.54	9.79	2.069
D1	0.64	2.02	1.09	3.88	4.99	1.054
E1	0.61	1.68	1.02	3.24	4.26	0.902
E2	0.80	2.12	1.36	4.09	5.45	1.153
E4	0.81	2.59	1.38	4.99	6.37	1.346
E6	0.75	2.84	1.27	5.49	6.77	1.430
E1	0.59	1.86	1.00	3.59	4.59	0.971
A1	0.61	1.81	1.04	3.49	4.53	0.958
B1	0.64	2.01	1.09	3.88	4.97	1.049
C1	0.64	2.01	1.09	3.86	4.97	1.049

Estimated Shear Stress Away from Influence of Structure

Grid Point = A1 (x = -4.92 ft; y = 0.364 ft; z = 0.12 in)

$$\begin{aligned} \tau_o &= \tau_{vo} + \tau_{to} & \tau_{vo} &= 1.06 \times 10^{-3} \text{ lb}_f/\text{ft}^2 \\ \tau_{vo} &= \mu \, du/dy & \tau_{to} &= 3.67 \times 10^{-3} \text{ lb}_f/\text{ft}^2 \\ \tau_{to} &= a\rho(u'^2 + v'^2) & \tau_o &= 4.74 \times 10^{-3} \text{ lb}_f/\text{ft}^2 \\ a &= 0.10 \end{aligned}$$

Table D.4 Results of hydrodynamic test H-3.

Structure = 70° Pile Cap - Bottom Position (0° to flow)

μ = 1.72×10^{-5} lb_f·sec/ft²

ρ = 62.18 lb_m/ft³

Grid Point	Velocity (ft/sec)	Turbulent Energy ft ² /sec ² x 10 ²	τ_v lb _f /ft ² x 10 ³	τ_t lb _f /ft ² x 10 ³	τ lb _f /ft ² x 10 ³	$\frac{\tau}{\tau_o}$
A1	0.66	2.22	1.15	4.28	5.45	0.924
A2	0.57	7.45	1.00	14.4	15.4	2.612
A3	0.82	6.70	1.44	13.0	14.4	2.440
A4	0.71	6.02	1.23	11.6	12.9	2.183
A5	0.67	5.94	1.17	11.5	12.7	2.149
A6	0.72	5.18	1.25	10.0	11.3	1.913
A7	0.56	4.35	0.98	8.39	9.40	1.593
A1	0.76	2.57	1.34	4.99	6.33	1.074
B1	0.73	2.61	1.27	5.03	6.33	1.073
B2	1.12	7.76	1.94	15.0	16.9	2.876
B3	1.02	6.87	1.77	13.3	15.1	2.556
B4	0.91	5.41	1.59	10.5	12.1	2.044
B5	0.86	5.15	1.50	9.96	11.4	1.944
B6	0.88	4.87	1.52	9.42	10.9	1.856
B7	0.75	5.05	1.31	9.75	11.1	1.878
B1	0.72	2.40	1.25	4.64	5.89	0.999
C1	0.71	2.43	1.23	4.70	5.93	1.007
C2	1.00	4.46	1.75	8.60	10.4	1.757
C3	1.05	5.43	1.84	10.5	12.3	2.091
C4	0.94	4.71	1.63	9.11	10.7	1.823

Table D.4--continued

C5	0.91	4.79	1.59	9.27	10.9	1.842
C6	0.93	4.71	1.63	9.11	10.7	1.820
C7	0.82	4.47	1.42	8.65	10.1	1.708
C1	0.71	2.61	1.23	5.03	6.26	1.065
D1	0.65	2.13	1.15	4.11	5.24	0.891
D2	0.91	2.57	1.59	4.97	6.56	1.113
D3	0.89	3.65	1.54	7.06	8.60	1.461
D4	0.89	3.89	1.54	7.52	9.06	1.538
D5	0.86	3.98	1.50	7.68	9.19	1.560
D6	0.90	3.84	1.57	7.41	8.98	1.525
D7	0.85	3.73	1.48	7.20	8.69	1.474
D1	0.66	2.00	1.15	3.86	5.01	0.850
E1	0.56	1.52	0.98	2.92	3.90	0.663
E2	0.79	1.78	1.38	3.45	4.80	0.817
E4	0.83	2.12	1.44	4.09	5.53	0.940
E6	0.78	2.16	1.36	4.18	5.53	0.940
E1	0.53	1.36	0.92	2.63	3.55	0.603
A1	0.75	2.70	1.29	5.22	6.52	1.107
B1	0.72	2.44	1.25	4.70	5.95	1.011

Estimated Shear Stress Away from Influence of Structure

Grid Point = A1 (x = -4.92 ft; y = 0.364 ft; z = 0.12 in)

$$\begin{aligned} \tau_o &= \tau_{vo} + \tau_{to} & \tau_{vo} &= 1.23 \times 10^{-3} \text{ lb}_f/\text{ft}^2 \\ \tau_{vo} &= \mu \, du/dy & \tau_{to} &= 4.66 \times 10^{-3} \text{ lb}_f/\text{ft}^2 \\ \tau_{to} &= a\rho(u'^2 + v'^2) & \tau_o &= 5.89 \times 10^{-3} \text{ lb}_f/\text{ft}^2 \\ a &= 0.10 \end{aligned}$$

Table D.5 Predicted and measured bottom elevations for scour test S-1 (no pile cap structure).

x (ft)	y (ft)	Measured Bottom Elevation after 28 hours (ft)	τ_d	Computed Equil. Bottom Elevation based on τ_d (ft)	Computed Equil. Bottom Elevation based on angle of repose (ft)	Predicted Equil. Bottom Elevation (ft)
0.33	0.00	-0.44	14.40	-0.55	-0.55	-0.55
0.33	0.16	-0.34	6.00	-0.34	-0.45	-0.45
0.33	0.33	-0.25	1.89	-0.14	-0.35	-0.35
0.33	0.49	-0.18	1.51	-0.11	-0.25	-0.25
0.33	0.66	-0.10	1.18	-0.06	-0.15	-0.15
0.33	0.82	-0.04	1.04	-0.03	-0.04	-0.04
0.33	0.98	0.00	1.02	-0.02	0.06	-0.02
0.33	1.15	0.01	1.02	-0.02	0.08	-0.02
0.33	1.31	0.01	1.02	-0.02	0.08	-0.02
0.33	1.48	0.00	1.01	-0.01	0.08	-0.01
0.33	1.64	0.00	1.01	-0.01	0.09	-0.01
0.33	1.80	0.00	1.00	0.00	0.09	0.00

Table D.5--continued

x (ft)	y (ft)	Measured Bottom Elevation after 28 hours (ft)	τ_d	Computed Equil. Bottom Elevation based on τ_d (ft)	Computed Equil. Bottom Elevation based on angle of repose (ft)	Predicted Equil. Bottom Elevation (ft)
1.31	0.00	-0.28	6.37	-0.35	-0.35	-0.35
1.31	0.16	-0.25	5.00	-0.30	-0.25	-0.30
1.31	0.33	-0.22	4.16	-0.27	-0.20	-0.27
1.31	0.49	-0.19	2.90	-0.21	-0.17	-0.21
1.31	0.66	-0.16	1.98	-0.15	-0.11	-0.15
1.31	0.82	-0.11	1.49	-0.11	-0.05	-0.11
1.31	0.98	-0.07	1.27	-0.08	0.00	-0.08
1.31	1.15	-0.04	1.16	-0.06	0.02	-0.06
1.31	1.31	-0.03	1.12	-0.05	0.04	-0.05
1.31	1.48	-0.03	1.10	-0.05	0.05	-0.05
1.31	1.64	-0.02	1.09	-0.04	0.05	-0.04
1.31	1.80	-0.02	1.08	-0.04	0.06	-0.04

Table D.5--continued

x (ft)	y (ft)	Measured Bottom Elevation after 28 hours (ft)	τ_d	Computed Equil. Bottom Elevation based on τ_d (ft)	Computed Equil. Bottom Elevation based on angle of repose (ft)	Predicted Equil. Bottom Elevation (ft)
2.30	0.00	-0.07				
2.30	0.16	-0.09				
2.30	0.33	-0.12	3.65	-0.25	-0.25	-0.25
2.30	0.49	-0.15	2.92	-0.21	-0.14	-0.21
2.30	0.66	-0.16	2.32	-0.17	-0.11	-0.17
2.30	0.82	-0.14	1.85	-0.14	-0.07	-0.14
2.30	0.98	-0.12	1.51	-0.11	-0.04	-0.11
2.30	1.15	-0.11	1.29	-0.08	0.00	-0.08
2.30	1.31	-0.09	1.17	-0.06	0.02	-0.06
2.30	1.48	-0.08	1.33	-0.06	0.04	-0.06
2.30	1.64	-0.08	1.10	-0.05	0.05	-0.05
2.30	1.80	-0.05	1.08	-0.04	0.05	-0.04

Table D.5--continued

x (ft)	y (ft)	Measured Bottom Elevation after 28 hours (ft)	τ_d	Computed Equil. Bottom Elevation based on τ_d (ft)	Computed Equil. Bottom Elevation based on angle of repose (ft)	Predicted Equil. Bottom Elevation (ft)
3.28	0.00	0.09				
3.28	0.16	0.04				
3.28	0.33	-0.01	3.13	-0.22	-0.22	-0.22
3.28	0.49	-0.05	2.65	-0.19	-0.12	-0.19
3.28	0.66	-0.08	2.25	-0.17	-0.09	-0.17
3.28	0.82	-0.11	1.91	-0.14	-0.07	-0.14
3.28	0.98	-0.11	1.63	-0.12	-0.04	-0.12
3.28	1.15	-0.11	1.42	-0.10	-0.02	-0.10
3.28	1.31	-0.11	1.28	-0.08	0.00	-0.08
3.28	1.48	-0.10	1.23	-0.07	0.02	-0.07
3.28	1.64	-0.10	1.20	-0.07	0.03	-0.07
3.28	1.80	-0.10	1.15	-0.06	0.03	-0.06

Table D.5--continued

x (ft)	y (ft)	Measured Bottom Elevation after 28 hours (ft)	τ_d	Computed Equil. Bottom Elevation based on τ_d (ft)	Computed Equil. Bottom Elevation based on angle of repose (ft)	Predicted Equil. Bottom Elevation (ft)
4.27	0.00	0.19				
4.27	0.16	0.15				
4.27	0.33	0.11	2.67	-0.20	-0.20	-0.20
4.27	0.49	0.04	2.57	-0.19	-0.09	-0.19
4.27	0.66	0.00	2.44	-0.18	-0.09	-0.18
4.27	0.82	-0.03	2.13	-0.16	-0.08	-0.16
4.27	0.98	-0.06	1.75	-0.13	-0.06	-0.13
4.27	1.15	-0.08	1.51	-0.11	-0.03	-0.11
4.27	1.31	-0.09	1.38	-0.09	0.00	-0.09
4.27	1.48	-0.10	1.33	-0.09	0.01	-0.09
4.27	1.64	-0.11	1.29	-0.08	0.01	-0.08
4.27	1.80	-0.11	1.24	-0.07	0.02	-0.07

Table D.5--continued

x (ft)	y (ft)	Measured Bottom Elevation after 28 hours (ft)	τ_d	Computed Equil. Bottom Elevation based on τ_d (ft)	Computed Equil. Bottom Elevation based on angle of repose (ft)	Predicted Equil. Bottom Elevation (ft)
5.25	0.00	0.21				
5.25	0.16	0.20				
5.25	0.33	0.18	2.26	-0.17	-0.17	-0.17
5.25	0.49	0.14	2.22	-0.17	-0.07	-0.17
5.25	0.66	0.09	2.14	-0.16	-0.06	-0.16
5.25	0.82	0.06	1.98	-0.15	-0.06	-0.15
5.25	0.98	0.02	1.78	-0.13	-0.05	-0.13
5.25	1.15	0.00	1.59	-0.12	-0.03	-0.12
5.25	1.31	-0.03	1.44	-0.10	-0.01	-0.10
5.25	1.48	-0.05	1.34	-0.09	0.00	-0.09
5.25	1.64	-0.07	1.26	-0.08	0.01	-0.08
5.25	1.80	-0.07	1.19	-0.06	0.03	-0.06

Table D.6 Predicted and measured bottom elevations for scour test S-2 (70° pile cap structure - top position).

x (ft)	y (ft)	Measured Bottom Elevation after 28 hours (ft)	τ_d	Computed Equil. Bottom Elevation based on τ_d (ft)	Computed Equil. Bottom Elevation based on angle of repose (ft)	Predicted Equil. Bottom Elevation (ft)
0.33	0.00	-0.63	28.60	-0.80	-0.80	-0.80
0.33	0.16	-0.51	8.00	-0.40	-0.69	-0.69
0.33	0.33	-0.40	2.59	-0.19	-0.59	-0.59
0.33	0.49	-0.28	1.98	-0.15	-0.49	-0.49
0.33	0.66	-0.19	1.49	-0.11	-0.39	-0.39
0.33	0.82	-0.14	1.31	-0.08	-0.28	-0.28
0.33	0.98	-0.09	1.35	-0.09	-0.18	-0.18
0.33	1.15	-0.02	1.33	-0.09	-0.08	-0.09
0.33	1.31	0.00	1.27	-0.08	0.01	-0.08
0.33	1.48	-0.01	1.20	-0.07	0.02	-0.07
0.33	1.64	-0.00	1.17	-0.06	0.03	-0.06
0.33	1.80	-0.00	1.15	-0.06	0.04	-0.06

Table D.6--continued

x (ft)	y (ft)	Measured Bottom Elevation after 28 hours (ft)	τ_d	Computed Equil. Bottom Elevation based on τ_d (ft)	Computed Equil: Bottom Elevation based on angle of repose (ft)	Predicted Equil. Bottom Elevation (ft)
1.31	0.00	-0.38	10.92	-0.48	-0.48	-0.48
1.31	0.16	-0.35	9.00	-0.43	-0.37	-0.43
1.31	0.33	-0.28	6.67	-0.36	-0.33	-0.36
1.31	0.49	-0.29	4.81	-0.29	-0.26	-0.29
1.31	0.66	-0.26	3.41	-0.23	-0.19	-0.23
1.31	0.82	-0.19	2.53	-0.19	-0.13	-0.19
1.31	0.98	-0.14	1.99	-0.15	-0.08	-0.15
1.31	1.15	-0.11	1.69	-0.12	-0.05	-0.12
1.31	1.31	-0.08	1.57	-0.11	-0.02	-0.11
1.31	1.48	-0.06	1.45	-0.10	-0.01	-0.10
1.31	1.64	-0.04	1.35	-0.09	0.00	-0.09
1.31	1.80	-0.01	1.35	-0.07	0.01	-0.07

Table D.6--continued

x (ft)	y (ft)	Measured Bottom Elevation after 28 hours (ft)	τ_d	Computed Equil. Bottom Elevation based on τ_d (ft)	Computed Equil. Bottom Elevation based on angle of repose (ft)	Predicted Equil. Bottom Elevation (ft)
2.30	0.00	-0.06				
2.30	0.16	-0.10				
2.30	0.33	-0.13	3.12	-0.22	-0.22	-0.22
2.30	0.49	-0.16	3.86	-0.26	-0.12	-0.26
2.30	0.66	-0.17	4.19	-0.27	-0.15	-0.27
2.30	0.82	-0.13	3.71	-0.25	-0.17	-0.25
2.30	0.98	-0.10	2.84	-0.20	-0.15	-0.20
2.30	1.15	-0.07	2.19	-0.16	-0.10	-0.16
2.30	1.31	-0.06	1.78	-0.13	-0.06	-0.13
2.30	1.48	-0.07	1.55	-0.11	-0.03	-0.11
2.30	1.64	-0.07	1.45	-0.10	-0.01	-0.10
2.30	1.80	-0.07	1.36	-0.09	0.00	-0.09

Table D.6--continued

x (ft)	y (ft)	Measured Bottom Elevation after 28 hours (ft)	τ_d	Computed Equil. Bottom Elevation based on τ_d (ft)	Computed Equil. Bottom Elevation based on angle of repose (ft)	Predicted Equil. Bottom Elevation (ft)
3.28	0.00	0.18				
3.28	0.16	0.11				
3.28	0.33	0.07	2.29	-0.17	-0.17	-0.17
3.28	0.49	0.02	3.00	-0.21	-0.07	-0.21
3.28	0.66	-0.01	3.44	-0.24	-0.11	-0.24
3.28	0.82	-0.03	3.48	-0.24	-0.13	-0.24
3.28	0.98	-0.04	3.20	-0.22	-0.14	-0.22
3.28	1.15	-0.03	2.73	-0.20	-0.12	-0.20
3.28	1.31	-0.03	2.15	-0.16	-0.09	-0.16
3.28	1.48	-0.04	1.61	-0.12	-0.06	-0.12
3.28	1.64	-0.04	1.49	-0.10	-0.02	-0.10
3.28	1.80	-0.05	1.39	-0.09	0.00	-0.09

Table D.6--continued

x (ft)	y (ft)	Measured Bottom Elevation after 28 hours (ft)	τ_d	Computed Equil. Bottom Elevation based on τ_d (ft)	Computed Equil. Bottom Elevation based on angle of repose (ft)	Predicted Equil. Bottom Elevation (ft)
4.27	0.00	0.31				
4.27	0.16	0.28				
4.27	0.33	0.24	2.68	-0.19	-0.19	-0.19
4.27	0.49	0.19	2.98	-0.21	-0.09	-0.21
4.27	0.66	0.15	3.21	-0.22	-0.11	-0.22
4.27	0.82	0.10	3.36	-0.23	-0.12	-0.23
4.27	0.98	0.07	3.34	-0.23	-0.13	-0.23
4.27	1.15	0.03	3.01	-0.21	-0.13	-0.21
4.27	1.31	0.02	2.48	-0.18	-0.11	-0.18
4.27	1.48	0.01	1.95	-0.15	-0.08	-0.15
4.27	1.64	-0.01	1.58	-0.11	-0.04	-0.11
4.27	1.80	-0.02	1.43	-0.10	-0.01	-0.10

Table D.6--continued

x (ft)	y (ft)	Measured Bottom Elevation after 28 hours (ft)	τ_d	Computed Equil. Bottom Elevation based on τ_d (ft)	Computed Equil. Bottom Elevation based on angle of repose (ft)	Predicted Equil. Bottom Elevation (ft)
5.25	0.00	0.33				
5.25	0.16	0.32				
5.25	0.33	0.31	2.07	-0.15	-0.15	-0.15
5.25	0.49	0.27	2.31	-0.17	-0.05	-0.17
5.25	0.66	0.22	2.53	-0.19	-0.07	-0.19
5.25	0.82	0.18	2.65	-0.19	-0.08	-0.19
5.25	0.98	0.15	2.62	-0.19	-0.09	-0.19
5.25	1.15	0.11	2.49	-0.18	-0.09	-0.18
5.25	1.31	0.08	2.29	-0.17	-0.08	-0.17
5.25	1.48	0.06	2.07	-0.15	-0.07	-0.15
5.25	1.64	0.04	1.86	-0.14	-0.05	-0.14
5.25	1.80	0.02	1.49	-0.10	-0.04	-0.10

Table D.7 Predicted and measured bottom elevations for scour test S-3 (70° pile cap structure - bottom position).

x (ft)	y (ft)	Measured Bottom Elevation after 28 hours (ft)	τ_d	Computed Equil. Bottom Elevation based on τ_d (ft)	Computed Equil. Bottom Elevation based on angle of repose (ft)	Predicted Equil. Bottom Elevation (ft)
0.33	0.00					
0.33	0.16					
0.33	0.33	-0.42	2.47	-0.18	-0.18	-0.18
0.33	0.49	-0.40	2.80	-0.20	-0.08	-0.20
0.33	0.66	-0.31	2.89	-0.21	-0.10	-0.21
0.33	0.82	-0.21	2.57	-0.19	-0.10	-0.19
0.33	0.98	-0.11	1.94	-0.15	-0.09	-0.15
0.33	1.15	-0.02	1.44	-0.10	-0.04	-0.10
0.33	1.31	0.01	1.20	-0.07	0.00	-0.07
0.33	1.48	0.02	1.11	-0.05	0.03	-0.05
0.33	1.64	0.02	1.07	-0.04	0.05	-0.04
0.33	1.80	0.02	1.07	-0.04	0.06	-0.04